# Numerical Shockwave Anomalies

by

Daniel Wei-Ming Zaide

A dissertation submitted in partial fulfillment
of the requirements for the degree of
Doctor of Philosophy
(Aerospace Engineering and Scientific Computing)
in The University of Michigan
2012

Doctoral Committee:

Professor Kenneth G. Powell, Co-Chair
Professor Philip L. Roe, Co-Chair
Professor James P. Holloway
Professor Bram van Leer
Assistant Professor Krzysztof J. Fidkowski
Robert B. Lowrie, Los Alamos National Laboratory

*"The most astounding fact, is the knowledge that the atoms that comprise life on Earth, the atoms that make up the human body, are traceable to the crucibles that cooked light elements into heavy elements in their core under extreme temperatures and pressures. These stars, the high mass ones among them, went unstable in their later years, they collapsed and then exploded, scattering their enriched guts across the galaxy. Guts made of carbon, nitrogen, oxygen, and all the fundamental ingredients of life itself. These ingredients became part of gas clouds that condense, collapse, form the next generation of solar systems, stars with orbiting planets, and these planets now have the ingredients for life itself. So that when I look up at the night sky, and I know that yes, we are part of this universe, we are in this universe, but perhaps more important that both of those facts, is that the universe is in us. When I reflect on that fact, I look up - many people feel small because the universe is big, but I feel big, because my atoms came from those stars. There's a level of connectivity. That's really what you want in life, you want to feel connected, you want to feel relevant. You want to feel like you're a participant in the goings on of activities and events around you. That's precisely what we are, just by being alive."*

*Neil deGrasse Tyson*

To my grandparents

# ACKNOWLEDGEMENTS

First and foremost, I'd like to thank my parents for being there while I pursued my academic dream. Their understanding and experience have been of tremendous assistance. Thank you to my sister, for inspiring me to follow my dreams and to do it while maintaining my sense of self and individuality; I am grateful to have you by my side. I am also grateful to my extended family, on both sides.

To Professor Carl Ollivier-Gooch at the University of British Columbia, thank you for giving me my first opportunity in this field and although I didn't know it at the time, for planting the challenges with shock-capturing into my head that would eventually consume me and lead to this very thesis. To Professor David Zingg at the University of Toronto for also giving me my break into CFD - your kind words no doubt contributed to my place at the University of Michigan.

To Phil, I remember walking into your office after my first viscous flow course and telling you I'd come to Michigan to work with you. Who knew that this is where we'd end up. Thank you for your continued support and patience with me. Thank you for challenging me while giving me the freedom to pursue my own ideas, however unsuccessfully, and cultivating my growth as a researcher.

To Ken, thank you for all the support and assistance and for always having an open door when I needed advice. I remember when we first started working together, you made it clear it was more about learning and education than the work itself. I also remember asking you if you wanted weekly meetings, and you telling me you didn't want students who needed weekly meetings. It has been a true pleasure, and

I couldn't have done it without you.

To Professor van Leer, thank you for believing in me and your assistance and experience on this challenging topic. You have been the voice of reason on many occasions and have been influential in my future endeavors. To Professor Fidkowski, for being a good role model and for providing helpful suggestions in a timely manner. To Professor Holloway, for having a sense of humour and graciously serving on my committee, as well as providing career advice and serving to my many other needs. To Rob, for advising me during my summer at Los Alamos and for being a great person to be around and work with.

A special thanks also goes out to Dr. Jim Kamm and Dr. Hung T. Huynh for their candor and enthusiasm about my work. Professor Z.J. Wang has taken me under his wing from afar, and mentored me over the last few years, and his advice and friendship are much appreciated. I would also like to thank my fellow current and former colleagues within the academic community, they have been of tremendous assistance during my time here, especially Huafei Sun. I'd also like to acknowledge a few friends, Katherine, Carol, Pete, Alina, Kian, and Vianne in Vancouver, Cece, Jenmy, Anita, and Paul in Toronto, Mike in Ottawa, and Cam and Denise in Montreal, among others for constantly reminding me there is more to life than research.

Finally, I'd like thank my sources of funding, for without them, I would not have been able to enjoy this experience. First, the Center for Radiative Shock Hydrodynamics at the University of Michigan has been of tremendous support over the past four years. Thank you Professor Paul Drake and the rest of the team for allowing me to pursue my interests within the CRASH program. I am also grateful for the contributions of the Natural Sciences and Engineering Research Council of Canada, which has allowed me to travel to places I never thought I'd go. Lastly, to Dr. Nikos Nikoforakis and the University of Cambridge and to Dr. Don Burton and Los Alamos National Laboratory, thank you for two wonderful summers.

# TABLE OF CONTENTS

**DEDICATION** . . . . . ii

**ACKNOWLEDGEMENTS** . . . . . iii

**LIST OF FIGURES** . . . . . vii

**CHAPTER**

**I. Introduction** . . . . . 1

1.1 Motivation . . . . . 1
1.2 Numerical Shockwave Anomalies . . . . . 4
1.2.1 Slowly Moving Shockwaves . . . . . 4
1.2.2 The Carbuncle . . . . . 5
1.2.3 The Wall Heating Phenomenon . . . . . 6
1.2.4 The Stationary Shock . . . . . 7
1.3 Thesis Overview . . . . . 7

**II. Physical Discretization** . . . . . 9

2.1 General Conservation Laws . . . . . 9
2.1.1 Weak Solutions . . . . . 10
2.1.2 The Riemann Problem . . . . . 11
2.2 Euler Equations . . . . . 12
2.3 The Finite Volume Method . . . . . 14
2.4 Roe's Riemann Solver . . . . . 17
2.5 Capturing Shocks . . . . . 18

**III. Shock-Capturing Anomalies** . . . . . 20

3.1 The Stationary Shock . . . . . 20
3.1.1 Ambiguity in Shock Position . . . . . 23
3.2 The Wall Heating Phenomenon . . . . . 25
3.2.1 The Reflecting Noh Problem . . . . . 29

3.2.2 The Start-up Error . . . 31
3.3 The Slowly Moving Shockwave Phenomenon . . . 32
3.4 The Carbuncle Phenomenon . . . 34
3.5 A Linear Hugoniot? . . . 36
3.6 Summary . . . 39

**IV. New Flux Functions** . . . 40

4.1 Interpolated Fluxes . . . 41
4.2 New Flux Function - A . . . 43
4.2.1 Observations . . . 44
4.3 New Flux Function - B . . . 45
4.4 Burgers' Equation . . . 46
4.4.1 Total Variation Diminishing . . . 48
4.4.2 Numerical Results . . . 50
4.5 Euler Equations . . . 51
4.5.1 Canonical Test Problems . . . 52
4.5.2 Numerical Shockwave Anomalies . . . 55
4.6 Summary . . . 63

**V. Extensions** . . . 65

5.1 Second-Order Accuracy . . . 65
5.2 Two Dimensions . . . 67
5.2.1 Euler Equations . . . 69
5.3 Second-Order Accuracy Results . . . 70
5.3.1 Simple Waves . . . 70
5.3.2 Isentropic Vortex . . . 72
5.3.3 Summary . . . 74
5.4 Results for Two-dimensional Shocks. . . . 74
5.4.1 Rotated Slowly Moving Shock Problem . . . 74
5.4.2 1.5D Carbuncle . . . 76
5.4.3 Double Mach Reflection . . . 77
5.4.4 Summary . . . 78

**VI. Conclusions and Future Work** . . . 90

**BIBLIOGRAPHY** . . . 96

# LIST OF FIGURES

**Figure**


1.1 Comparison between a stone wall and a captured shockwave. . . . . 3

2.1 Representative solution to the Riemann Problem. . . . . 12

2.2 Representative Hugoniot curves for the Euler equations. . . . . 15

2.3 Representative single shock problem. . . . . 19

3.1 Comparison of results using various flux functions for a Mach 10 stationary shockwave. . . . . 22

3.2 Wave diagram for the one-point stationary shockwave. . . . . 22

3.3 Equal area rule. . . . . 23

3.4 Shock position in energy vs shock position in density. . . . . 24

3.5 Diagram of the Noh problem. . . . . 26

3.6 Conserved quantities for a Mach 1.1 Noh problem. . . . . 28

3.7 Conserved quantities for a Mach $10^6$ Noh problem. . . . . 28

3.8 Shock position vs time for the Noh problem. . . . . 28

3.9 The reflecting Noh problem. . . . . 29

3.10 Results for the reflected Noh problem. . . . . 30

3.11 Results for a single shock problem. . . . . 31

3.12 Perturbations of the stationary shock. . . . . 32

3.13 Intermediate states of the slowly moving shock. . . . . 33

3.14 Intermediate states of the one-dimensional carbuncle for a Mach 20 shock. . . . . 35

3.15 Results for the Noh-like problem for the straight-line system. . . . . 38

3.16 Results for the slowly moving shock problem for the straight-line system. . . . . 38

4.1 Physically realizable region of interpolated flux for Burgers' Equation 47

4.2 Simple wave results for Burgers' equation. . . . . 51

4.3 Numerical results for Sod's Shocktube Problem. . . . . 53

4.4 Numerical results for the Double Blast Wave problem. . . . . 54

4.5 Numerical results for the Shu-Osher test problem at $t = 1.8$. . . . . 55

4.6 Results for the slowly moving shock problem with $S = 0.0001$. . . . 58

4.7 Results for the slowly moving shock problem with $S = 0.001$. . . . . 59

4.8 Results for the slowly moving shock problem with $S = 0.1$. . . . . 60

4.9 Relative Maximum Momentum Error vs Shock Speed. . . . . 60

4.10 Density, velocity and pressure results for the Noh problem with initial Mach number of 2 (top) and Mach number of 10 (bottom). . . . . 61

4.11 Relative Wall Density Error vs Mach number for Roe's Riemann Solver ($\times$), flux function A ($\square$), and flux function B ($\circ$). . . . . 62

4.12 Stability results for the one-dimensional carbuncle. . . . . 64

5.1 Oblique shock in two dimensions. . . . . 67

5.2 Error Convergence for the 1D (left) and 2D (right) moving density wave. . . . . 71

5.3 Error convergence for the simple compression wave. . . . . 72

5.4 Error convergence for the simple expansion. First order results (left) and second order results (right). . . . . 73

5.5 Error convergence for the isentropic vortex. . . . . 74

5.6 Initial set-up for the rotated slowly moving shock problem. . . . . 75

5.7 Results for the rotated slowly moving shock problem for Roe's Riemann solver with $M_0 = 2, S = 0.01$, and $\alpha = 5.71°$. . . . . 79

5.8 Results for the rotated slowly moving shock problem for flux function A. . . . . 80

5.9 Results for the rotated slowly moving shock problem for flux function B. . . . . 81

5.10 Errors in momentum for both new flux functions and Roe's Riemann solver for the Mach 2.0 shock with speed 0.01. . . . . 82

5.11 Errors in momentum for both new flux functions and Roe's Riemann solver for the Mach 2.0 shock with speed 0.1. . . . . 82

5.12 Results for the rotated slowly moving shock problem for Roe's Riemann solver with $M_0 = 10, S = 0.01$, and $\alpha = 11.4°$. . . . . 83

5.13 Results for the rotated slowly moving shock problem for flux function A. . . . . 84

5.14 Results for the rotated slowly moving shock problem for Roe's Riemann solver with $M_0 = 10, S = 0.01$, and $\alpha = 41°$. . . . . 85

5.15 Results for the rotated slowly moving shock problem for flux function A. . . . . 86

5.16 Results for the rotated slowly moving shock problem for flux function B. . . . . 87

5.17 Errors in momentum for both new fluxes and Roe's Riemann solver for the Mach 10.0 shock with speed 0.01. . . . . 88

5.18 Errors in momentum for both new fluxes and Roe's Riemann solver for the Mach 10.0 shock with speed 0.1. . . . . 88

5.19 Density contours for the double mach reflection for a 480 x 120 grid at t = 0.2. . . . . 89

# CHAPTER I

# Introduction

## 1.1 Motivation

Understanding shockwaves is critical to the prediction and study of many phenomena, where abrupt changes in material properties due to shockwaves can greatly affect regions of interest and activate physical mechanisms, including combustion or ionization [103]. With the increased focus on proper utilization of computational resources for problems with complex physics and fine-scale features, it is important to develop numerical methods that perform reliably and accurately and can be trusted with problems where little or no experimental data exists.

For flows governed by continuum mechanics, such as those modeled by the Euler equations, the majority of numerical methods have been developed off of the simple linear advection equation where it is possible to prove various mathematical properties such as stability and accuracy [76]. It is impressive that the methods developed from this scalar linear equation extend so well to nonlinear systems of equations, since the analysis of numerical schemes is difficult. This is especially true when shockwaves or other discontinuities are present. The nonlinear effects of the discontinuity are hard to predict and thus solution quality is far from guaranteed.

Although generally modeled as discontinuities, true shockwaves have finite width over which the energy is transformed from kinetic energy into heat, a process described

by viscous dissipation. However, for numerical shockwaves there is a numerical width, often much greater than the physical width. While the numerical width could be reduced to the order of the physical width, in practice this is much too computationally expensive and the governing equations do not apply at those small scales. Methods do exist that resolve the physical width of the shockwave by modeling particles collisions, as in gas kinetic schemes [100]. In practice, these methods are not as efficient and can be impractical for problems where the flow is of a mostly continuous nature.

While many schemes exist for these flows, this thesis focuses on a particular class of schemes for resolving shockwaves — Godunov-type shock capturing schemes [23] — due to their predominance in many commercial and research codes. Despite their common usage and generally good performance, there are still pervasive errors that can occur that do not disappear with common techniques such as increased grid resolution or accuracy. Previous work has classified some of these errors as errors in shock position, spurious waves, or unstable shock behavior [102]. These will be referred to as **Numerical Shockwave Anomalies**.

Godunov-type schemes, in their simplest form, consist of several steps. First, the domain is divided into a series of 'control volumes', or cells, separated by edges and the data is integrated and averaged to obtain a 'cell-average' in each cell. The cell-averages in neighboring control volumes are then used to determine how much of each quantity has moved between cells using a flux function and a flux at each cell edge is calculated. Finally, the data is updated using the difference in edge fluxes for each cell, determining how much of each quantity has moved in and out of a cell through its edges in a given time. Conservation is maintained since data is only changed through fluxes. Along with cell-averages, this is the heart of shock-capturing. By not dealing with derivatives and ensuring total quantities are conserved, the correct discontinuities are captured.

The first successful shock capturing solutions occurred in Los Alamos as part of

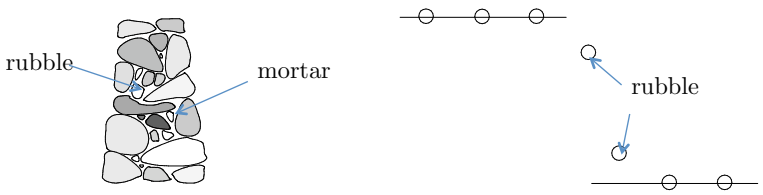


A wall built of natural stone. A captured shockwave.

Figure 1.1: Comparison between a stone wall and a captured shockwave.

the Manhattan Project were conducted by Von Neumann and Richtmyer [95]. These were done in the moving frame, adding an artificial viscosity to spread the shock over multiple cells and to mimic the physical viscosity not present in the governing equations. This leads to the formation of intermediate states having no direct physical interpretation. These 'filler' states serve the same purpose as the filler within a rough stone wall - only how it looks from either side is of interest, and anything can be put within it, as long as the final product is acceptable (Figure 1.1). Of course, as the mesh is refined, these intermediate states do not go away; they simply occupy less space. The existence of intermediate states does raise some doubt, however, as to how closely a captured shockwave may emulate an ideal discontinuous shockwave, or a real physical one.

With the potential issues arising from these intermediate states, some people would not ask how shocks should be captured but whether they should be captured at all [61, 82, 83]. This led to the development of shock fitting schemes, treating a shock as an explicit discontinuity satisfying internal boundary conditions where it can be represented with zero width. This works well when it is possible to determine the exact location of a shock, but is much more challenging when shocks interact and there is a complex shock structure. Hybrid approaches have been tried, using a shock-capturing method but aligning the grid with the shock [93] to avoid having any intermediate shock states, but this too is only effective for simple shocks. More recent work [66, 67] has combined shock fitting with shock capturing, only fitting the

dominant shockwaves.

## 1.2 Numerical Shockwave Anomalies

One of the first accounts of anomalous behavior was by in 1966 by Cameron [6], using a similar method to that of von Neumann and Richtmyer, who observed oscillations produced when shockwaves crossed both grid and material interfaces. He suggested that either the artificial viscosity or the mesh should be modified to properly smear out the shock. Two years later Emery [17] identified errors produced by shockwaves and again, suggested adding additional viscosity. As new shock capturing schemes were being developed, anomalous behavior was more frequently observed and could be classified into several main categories.

### 1.2.1 Slowly Moving Shockwaves

The slowly moving shockwave phenomenon, is the shedding of spurious waves by slowly moving shocks. One of the first observations was by Woodward and Colella who noticed oscillatory behavior in their analysis of strong shock problems [97]. Their solution was to remove the errors by jiggling the mesh, keeping the shock speed relative to the grid from being too small. This technique was effective for their work, but is far from scientific.

The first detailed study of slowly moving shocks was by Roberts, [73] who examined the intermediate shock states and noted their role in the creation of spurious waves. Similar work by Arora and Roe [1] would follow up on this idea, studying a range of problems and the role of intermediate states, relating the problem to an error in the stationary shock structure. The consensus in the literature [34, 35, 14, 38, 99, 89, 36, 37] is that the root cause of these post shock oscillations is the unsteadiness of the viscous profile and the inability of any existing scheme to add what is deemed to be the 'correct' artificial viscosity. Xu [98] even went as

far as to suggest that getting the viscosity correct was impossible, and no scheme of the type would ever work. Other researchers have not been as negative, developing various forms of artificial viscosity and showing fairly positive results, albeit with no complete elimination of the errors without smearing the shock entirely.

### 1.2.2 The Carbuncle

Another anomaly, first described by Peery and Imlay [69] as an irregular shock behavior around a blunt body, the carbuncle has since been replicated in other situations [43]. Specifically, Quirk introduced the most commonly analysed version, consisting of a one-dimensional stationary shock in a two-dimensional domain. By perturbing the shock, in his case through the grid, an instability is provoked and a shock behavior similar to that of the original carbuncle is observed. An even simpler version of the problem has also been analysed [8, 42], in the form of a one-dimensional stationary shock that does not remain stationary. Looking back to classical theory, Dyakov [13] and Landau and Livschitz [44] showed that the exact stationary shock-wave was always stable, at least for convex equations of state. This has led many to believe the carbuncle is purely a numerical artifact.

For numerical shockwaves, the analysis has most often taken the form of a linearized stability analysis, examining the stability of perturbations to the flow field [2, 5, 74, 68, 12, 3]. This has led to a wide range of theories about possible causes, from too much numerical vorticity [31, 70] to the commonly accepted conjecture of Liou [51], that flux functions where the mass flux is not a function of the pressure jump will not suffer from the carbuncle or other instabilities. Flux functions of this type are not physical, and were later shown to suffer from carbuncles [31, 42]. More rigorous analysis has also made the connection between the carbuncle and schemes that exactly capture contact discontinuities and shear waves [74, 68]. This is unfortunate, as ideally a scheme would be able to properly capture all types of discontinuities

without suffering from instabilities.

With these insights in mind, most cures still go back to the idea of artificial viscosity, developing some form of variable dissipation or adaptive flux function in an attempt to damp out unstable modes and prevent the growth of instabilities [40, 71, 39, 25, 64, 41, 85]. There is also the entropy based approach of Ismail and Roe [32]. They initially claimed this was carbuncle-free although this was later shown to not be the case [21]. In recent years, there has also been work focusing specifically on the role of the grid in these problems [28, 57], although neither offers any real cure.

One of the major challenges with the whole class of carbuncles is that they are physical solutions, 'mimicking' experimentally observable behavior [60, 77]. More recently, Elling [16] went as far as to suggest that since carbuncles are entropy-satisfying solutions, to eliminate them would be making false physical assumptions and they are thus incurable. At this point though, there does not seem to be enough evidence to make such strong claims.

### 1.2.3 The Wall Heating Phenomenon

A third anomaly is the creation of persistent "entropy traces" caused by an inappropriate production of entropy which then propagates in a physical manner [75, 80]. One such example, the wall heating phenomenon exemplified by Noh's [65, 99] well known test problem has caused much grief, both in the Eulerian and Lagrangian communities and occurs for a wide range of methods and physics [20]. This problem is exacerbated by methods that capture contact discontinuities [62], which also capture errors along contacts and are generally less diffusive.

Similar to Noh's original remedy, artificial heat conduction has been used in several other methods to alleviate the temperature excess[62, 11, 18], although much like Noh's original work, these tend to smear out other flow features. There have also been shock fitting attempts [19, 30] which have shown good results on the Noh problem.

These, however, still suffer from the standard challenges of shock fitting approaches. A more recent examination of it is that of Liou [52], who refers to it as the 'volcano' phenomenon.

A special case of wall heating is the so-called "start-up error", common in almost all shock capturing solvers. In 2000, a more detailed study by Rider [72] suggested that the cause is actually due to a phase error between density and pressure. This is in agreement with the analysis of Quirk and the conjecture of Liou for the carbuncle, suggesting a connection between the two anomalies.

### 1.2.4 The Stationary Shock

With all the attention on instabilities in the stationary shock, there is an anomaly within the shock structure itself [1] - the ambiguity of the sub-cell location of a stationary captured shock. This has been related to errors produced in interacting shocks by Menikoff [59], who noted the shift in relative energies resulted in entropy errors. While not initially appearing to be a problem, it is discomforting to note even within a captured shock, there is no agreement on its location within a cell.

## 1.3 Thesis Overview

It has been previously postulated by Barth [2] and Robinet et al. [74] among others [72, 92, 89] that many of these numerical problems are related. In this thesis, a different approach is applied to study these problems, choosing to link them through the nonlinearity of the jump conditions and the resulting ambiguity in sub-cell shock position. Several cures are then developed and discussed.

The major contributions of this thesis are:

[1] There is a large amount of mathematical literature on the existence of discrete stationary shock profiles [33, 58, 53, 84, 54, 55]. Only those that provide relevant numerical insights are discussed here.

- A deeper understanding of shock-capturing, the role of numerical shockwave structure and numerical shockwave anomalies.
- The determination of a major cause of numerical shockwave anomalies and the relationship between the nonlinearity of the physics and the anomalies.
- The development of two new flux functions that eliminate the cause and alleviate the errors caused by the anomalies.
- The extension of both new flux functions to higher-order schemes and multi-dimensional problems to verify future practicality and performance when shockwaves are multi-dimensional.

This thesis is organized as follows. In Chapter II, the basic mathematical properties of conservation laws are described followed by the shock-capturing methodology, with application to the Euler equations. The methods and analysis utilized can be generalized to other systems, although for the most part, analysis and numerical experiments are only performed for the Euler equations. In Chapter III, each numerical shockwave anomaly is analysed and linked to a single cause, the nonlinearity of the jump conditions and corresponding ambiguity in sub-cell shock position. With the cause identified, Chapter IV describes several methods that do not suffer from it and their superior properties and performance are shown in comparison with the baseline method in one dimension. To ensure these methods are potentially practical, Chapter V outlines two basic extensions of the method - second-order accuracy and two-dimensional problems and verifies the behavior on both new methods on a range of representative problems. Finally, in Chapter VI, conclusions are made and directions for future work are presented.

# CHAPTER II

# Physical Discretization

## 2.1 General Conservation Laws

Conservation laws are physical principles found throughout physics and nature. The general differential form for a system of conservation laws in one dimension can be written

$$\frac{\partial \mathbf{u}}{\partial t} + \frac{\partial \mathbf{f}}{\partial x} = \mathbf{0} \tag{2.1}$$

for the vector of conserved quantities $\mathbf{u}(x,t)$ and corresponding fluxes $\mathbf{f}(\mathbf{u}(x,t))$. In integral form, these state that the total amount of the conserved quanties in a domain $\Omega$ change proportional to the fluxes through the boundary,

$$\frac{\mathrm{d}}{\mathrm{d}t}\int_{\Omega} \mathbf{u} = \oint_{\partial\Omega} \mathbf{f}\cdot\mathbf{n}\,\mathrm{d}\Omega. \tag{2.2}$$

For simplicity, only one dimensional equations will be analysed, as many of their properties extend to additional spatial dimensions and since the numerical methods examined are based one dimensional derivations. Higher-order derivatives and source terms have also been ignored, a fair assumption for compressible, inviscid fluid flows as well as a wide range of other physics. For smooth solutions, this system can be

written in quasi-linear form as

$$\frac{\partial \mathbf{u}}{\partial t} + \mathbf{A}(\mathbf{u})\frac{\partial \mathbf{u}}{\partial x} = \mathbf{0} \tag{2.3}$$

where $\mathbf{A}(\mathbf{u}) = \frac{\partial \mathbf{f}}{\partial \mathbf{u}}$ is the flux Jacobian. Of particular interest here are hyperbolic conservation laws, distinguished by their wave-like solutions and the mathematical structure of their governing partial differential equations. The system is hyperbolic if the flux Jacobian has an eigenvalue decomposition $\mathbf{A} = \mathbf{R}\mathbf{\Lambda}\mathbf{L}$ with real eigenvalues in $\mathbf{\Lambda}$ and distinct eigenvectors in $\mathbf{R}$. This eigendecomposition leads to the set of left eigenvectors $\mathbf{L}$, and characteristic speeds $\mathbf{\Lambda}$ which arise from the diagonalized equations, obtained from conservation form by

$$\begin{aligned}
\frac{\partial \mathbf{u}}{\partial t} + \frac{\partial \mathbf{f}}{\partial x} &= \mathbf{0} && (2.4)\\
\frac{\partial \mathbf{u}}{\partial t} + \mathbf{A}\frac{\partial \mathbf{u}}{\partial x} &= \mathbf{0} && (2.5)\\
\frac{\partial \mathbf{u}}{\partial t} + \mathbf{R}\Lambda\mathbf{L}\frac{\partial \mathbf{u}}{\partial x} &= \mathbf{0} && (2.6)\\
\mathbf{L}\frac{\partial \mathbf{u}}{\partial t} + \Lambda\mathbf{L}\frac{\partial \mathbf{u}}{\partial x} &= \mathbf{0} && (2.7)
\end{aligned}$$

which show that the derivative of the $k^{th}$ Riemann invariant, $(\mathbf{L}\mathrm{d}\mathbf{u})_k$ is zero along characteristic curves with $\frac{\mathrm{d}x}{\mathrm{d}t} = \lambda_k$. This allows for construction and analysis of smooth solutions. For discontinuous solutions, the notion of a weak solution needs to be introduced.

### 2.1.1 Weak Solutions

Fundamental to this work and one of the major challenges with hyperbolic conservation laws is their admission of weak solutions. Weak solutions are solutions that satisfy

$$\int_0^\infty \int_{-\infty}^{\infty} \left[\frac{\partial \phi}{\partial t}\mathbf{u} + \frac{\partial \phi}{\partial x}\mathbf{f}\right] \mathrm{d}x\mathrm{d}t = -\int_{-\infty}^{\infty} \phi(x,0)\mathbf{u}(x,0)\mathrm{d}x \tag{2.8}$$

for all continuously differentiable test functions $\phi(x,t)$ that vanish on the boundaries[1]. In effect, the need for the conserved quantities to be differentiable has been transferred to the test functions and discontinuous solutions can exist. If a discontinuity is present in the solution, the conservation laws are satisfied through a set of equations known as jump conditions. The jump conditions represent many fluid phenomena, such as shockwaves and material interfaces and provide a foundation for analysis and development of meaningful test problems. Analytically, they are the set of equations connecting the solution from left state $\mathbf{u}_L$ to the right state $\mathbf{u}_R$ across a discontinuity with speed $S$,

$$\mathbf{f}(\mathbf{u}_R) - \mathbf{f}(\mathbf{u}_L) = S(\mathbf{u}_R - \mathbf{u}_L). \tag{2.9}$$

It is clear that the jump conditions themselves do not lead to a unique solution and additional information, an entropy condition, is required. For the systems examined in this work, the flux function is convex and an entropy condition [46] for a shock discontinuity across the $i^{th}$ nonlinear characteristic is

$$\lambda_i(\mathbf{u}_L) > S_i > \lambda_i(\mathbf{u}_R), \tag{2.10}$$

which allows a discontinuity only if the characteristics intersect. Without the entropy condition, there is no measure to distinguish the physical solution from a nonphysical solution and an entropy-violating shock can occur.

### 2.1.2 The Riemann Problem

The Riemann problem is a special initial value problem, with

$$\mathbf{u}(x,0) = \begin{cases} \mathbf{u}_L & x < 0 \\ \mathbf{u}_R & x > 0 \end{cases} \tag{2.11}$$

[1]As this work is not interested in proving the existence or other properties of weak solutions, more information can be found in [46].

The similarity solution $\mathbf{u}(x/t)$ is composed of simple waves associated with the characteristics and can be formed from characteristic information and the jump conditions, depending on the waves present. In Figure 2.1, a representative three-wave solution is shown in both physical space and state space, describing the solution at each $(x/t)$.

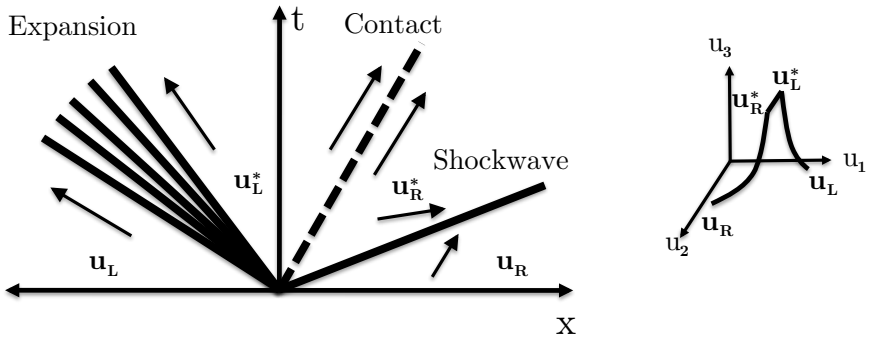


Figure 2.1: Representative solution to the Riemann Problem. (left) Physical Space. (right) State Space.

## 2.2 Euler Equations

The main equations studied in this thesis are the Euler Equations. The Euler equations, shown in one dimension, are the set of conservation laws governing compressible fluid flow in the absence of viscosity and heat conduction. They will serve as the basis for the majority of the numerical experiments performed in this work and represent the conservation of mass, momentum, and energy

$$\frac{\partial}{\partial t}\begin{bmatrix} \rho \\ \rho u \\ E \end{bmatrix} + \frac{\partial}{\partial x}\begin{bmatrix} \rho u \\ \rho u^2 + p \\ \rho u H \end{bmatrix} = \mathbf{0} \tag{2.12}$$

with the equation of state $p = p(\rho, e)$, enthalpy $H = \frac{E+p}{\rho}$ and an entropy $s = p\rho^{-\gamma}$. For an ideal gas ,the equation of state is

$$p = (\gamma - 1)\rho e = (\gamma - 1)\left(E - \frac{1}{2}\rho u^2\right). \tag{2.13}$$

where $\gamma$ is the polytropic constant, the ratio of specific heats. The main propagation speed is the sound speed, $a = \sqrt{\frac{\gamma p}{\rho}}$. The flux Jacobian is

$$\mathbf{A} = \begin{bmatrix} 0 & 1 & 0 \\ (\gamma-3)\frac{u^2}{2} & (3-\gamma)u & \gamma - 1 \\ \left(\frac{\gamma-1}{2}u^2 - H\right)u & H + (1-\gamma)u^2 & \gamma u \end{bmatrix}. \tag{2.14}$$

The eigenvalues and eigenvectors are

$$\mathbf{\Lambda} = \begin{bmatrix} u-a & 0 & 0 \\ 0 & u & 0 \\ 0 & 0 & u+a \end{bmatrix}, \qquad \mathbf{R} = \begin{bmatrix} 1 & 1 & 1 \\ u-a & u & u+a \\ H-ua & \frac{1}{2}u^2 & H+ua \end{bmatrix}. \tag{2.15}$$

The Riemann invariants are

$$\mathbf{L}\mathrm{d}\mathbf{u} = \frac{1}{a^2}\begin{bmatrix} \frac{1}{2}(\mathrm{d}p - \rho a \mathrm{d}u) \\ -(\mathrm{d}p - a^2\mathrm{d}\rho) \\ \frac{1}{2}(\mathrm{d}p + \rho a \mathrm{d}u) \end{bmatrix} \tag{2.16}$$

with the first and third invariants corresponding to acoustic waves and the second invariant corresponding to an entropy wave.

To describe shockwaves, the jump conditions are used. For waves corresponding to $\lambda = u+a$, suppose that the left (preshock) state is completely known, as $\rho_L, u_L, p_L$. If the density on the right is prescribed to be $\rho_R$, then the remaining postshock variables

are given in [9] by

$$p_R = p_L \frac{(\gamma+1)\rho_R - (\gamma-1)\rho_L}{(\gamma+1)\rho_L - (\gamma-1)\rho_R} \tag{2.17}$$

$$u_R = u_L + (p_L - p_R)\sqrt{\frac{2}{\rho_L\left((\gamma-1)p_L + (\gamma+1)p_R\right)}} \tag{2.18}$$

with the shock speed as

$$S = u_L + a_L\sqrt{1 + \frac{\gamma+1}{2\gamma}\left(\frac{p_R}{p_L} - 1\right)}. \tag{2.19}$$

The curve traced out in phase space by solving these equations is the Hugoniot curve. It has two branches. If $\rho_R > \rho_L$ then each point on the curve represents a valid state behind a (generally moving) shockwave, and this will be referred to as the *physical branch* of the Hugoniot curve. If $\rho_R < \rho_L$ this generates the *nonphysical branch* of the Hugoniot. A jump from $\mathbf{u}_L$ to $\mathbf{u}_R$ would violate thermodynamics. Note however, that each point on the nonphysical branch represents a state from which $\mathbf{u}_L$ could be reached by a valid shockwave. Typical Hugoniot curves are shown in Figure 2.2, demonstrating the differences between the two branches of the Hugoniot.

Along with shockwaves, these equations also allow for discontinuities in the form of contact discontinuities, which satisfy Equation (2.9) where $S = u$, the flow velocity. These are discontinuities characterized by constant velocity and pressure and a jump in density and entropy. Although not the focus of this thesis, their interaction with shockwaves is still important.

## 2.3 The Finite Volume Method

To examine numerical anomalies within the shock capturing framework, the Finite Volume method will be used. In its simplest form, it also represents the basis of other classes of methods, such as Discontinuous Galerkin.

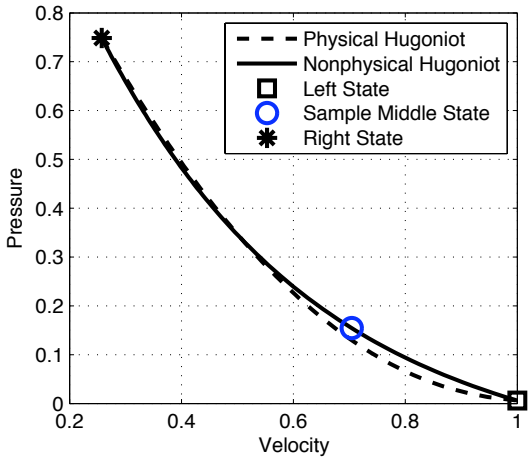


Figure 2.2: Representative Hugoniot curves for the stationary shock in the Euler equations. The physical Hugoniot is plotted through through L and the nonphysical Hugoniot through R. (Note that the curves are really in three-dimensional space, and do not actually intersect.)

For the general system of conservation laws in Equation (2.1), a cell average for a cell centered at $x_i$ can be defined as

$$\overline{\mathbf{u}_i} = \frac{1}{\Delta x_i} \int_{x_i - \Delta x_i/2}^{x_i + \Delta x_i/2} \mathbf{u} \ \mathrm{d}x. \tag{2.20}$$

Integrating in space leads to

$$\frac{\partial}{\partial t} \left( \int_{x_i - \Delta x/2}^{x_i + \Delta x/2} \mathbf{u} \ \mathrm{d}x \right) + \int_{x_i - \Delta x/2}^{x_i + \Delta x/2} \frac{\partial \mathbf{f}(\mathbf{u})}{\partial x} \ \mathrm{d}x = \mathbf{0} \tag{2.21}$$

and using the divergence theorem and the definition of a cell average results in

$$\frac{\partial \overline{\mathbf{u}_i}}{\partial t} + \frac{\mathbf{f}(x_i + \Delta x_i/2) - \mathbf{f}(x_i - \Delta x_i/2)}{\Delta x_i} = \mathbf{0}, \tag{2.22}$$

which are the semi-discrete conservation laws for the cell-averaged conserved variables. Evaluating the fluxes at the cell boundary can be done in several ways; here the flux will be evaluated from the solution to the Riemann problem of the adjacent

states, as $\hat{\mathbf{f}}(\mathbf{u}(x_i+\Delta x_i/2), \mathbf{u}(x_{i+1}-\Delta x_{i+1}/2))$, or with the cell-averaged representation, $\hat{\mathbf{f}}(\overline{\mathbf{u}}_i, \overline{\mathbf{u}}_{i+1})$. The equations in semi-discrete form are

$$\frac{\partial \overline{\mathbf{u}}_i}{\partial t} + \frac{1}{\Delta x_i}(\hat{\mathbf{f}}(\overline{\mathbf{u}}_i, \overline{\mathbf{u}}_{i+1}) - \hat{\mathbf{f}}(\overline{\mathbf{u}}_{i-1}, \overline{\mathbf{u}}_i)) = \mathbf{0}. \tag{2.23}$$

In this thesis, the time integration method is not of primary interest for the first-order spatial discretization and thus the first-order in time Forward Euler method is used. The cell average at time $t^{n+1}$ is then

$$\mathbf{u}_i^{n+1} = \mathbf{u}_i^n - \frac{\Delta t}{\Delta x}(\mathbf{f}(\mathbf{u}_i^n, \mathbf{u}_{i+1}^n) - \mathbf{f}(\mathbf{u}_{i-1}^n, \mathbf{u}_i^n)) \tag{2.24}$$

where the overbar and hat notation has been dropped for simplicity. For stability, the timestep is restricted by the CFL condition [10],

$$CFL = \max_i |\lambda_i| \frac{\Delta t}{\Delta x} \leq 1 \tag{2.25}$$

which ensures the grid speed, $\Delta x/\Delta t$, is greater than all characteristic speeds $\lambda_i$. This method is conservative, and if the solution converges as the grid is refined, the solution will converge to a weak solution by the Lax-Wendroff Theorem [47]. This does not however, guarantee it will converge to a unique solution and convergence is only guaranteed in the weak sense - there is still room for pointwise errors, provided they cancel out under integration. This is critical to explaining much of the anomalous behavior observed.

The analysis and experiments are restricted to first-order accuracy partly for simplicity, but also because experience suggests that not only do high-order schemes suffer all of the problems that afflict their first-order versions, merely providing better resolution of the spurious physics, but also reduce to a first-order scheme in the vicinity of shockwaves [7, 101].

## 2.4 Roe's Riemann Solver

Roe's Riemann solver [78] will be used throughout this work as the main Riemann solver for computing interface fluxes. It is exact for a single shockwave and provides nearly identical results to the exact Riemann solver for all of the anomalies examined. While other Riemann solvers are known to handle some of the numerical phenomena better, they do so by adding diffusion and smearing the solution [51], providing poor results in certain flow regions, such as those with shock-boundary layer interactions. Given a left state $\mathbf{u}_i$ and a right state $\mathbf{u}_{i+1}$, the flux between them is

$$\mathbf{f}_{i+\frac{1}{2}} = \frac{1}{2}(\mathbf{f}_i + \mathbf{f}_{i+1}) - |\tilde{\mathbf{A}}_{i+\frac{1}{2}}|(\mathbf{u}_i, \mathbf{u}_{i+1})|(\mathbf{u}_{i+1} - \mathbf{u}_i) \tag{2.26}$$

and the approximate flux Jacobian $\tilde{\mathbf{A}}(\mathbf{u}_i, \mathbf{u}_{i+1}) = \mathbf{A}(\tilde{\mathbf{u}}_{i+\frac{1}{2}})$ is constructed with the following properties:

1. The eigenvalue decomposition $\tilde{\mathbf{A}} = \tilde{\mathbf{R}}\tilde{\mathbf{\Lambda}}\tilde{\mathbf{L}}$ has real eigenvalues and linearly independent eigenvectors such that the new system remains hyperbolic.

2. Consistency, when $\mathbf{u}_i, \mathbf{u}_{i+1} \rightarrow \mathbf{u}$, $\tilde{\mathbf{A}}(\mathbf{u}, \mathbf{u}) = \mathbf{A}(\mathbf{u})$.

3. Conservation across discontinuities, $\Delta\mathbf{f} = \tilde{\mathbf{A}}\Delta\mathbf{u}$.

This final property leads to the flux description of Roe's approximate Riemann solver,

$$\mathbf{f}_{i+\frac{1}{2}} = \frac{1}{2}(\mathbf{f}_i + \mathbf{f}_{i+1}) - \text{sign}(\tilde{\mathbf{A}}_{i+\frac{1}{2}})(\mathbf{f}_{i+1} - \mathbf{f}_i) \tag{2.27}$$

which will also be used in subsequent chapters as the basis for a new flux function. $\tilde{\mathbf{A}} = \tilde{\mathbf{A}}(\tilde{\mathbf{u}})$ can be computed from the choice of the Roe-averaged variables, $\tilde{\mathbf{u}}$ and is

dependent on the system of equations. For the Euler Equations, they are

$$\tilde{u} = \frac{\sqrt{\rho_i}u_i + \sqrt{\rho_{i+1}}u_{i+1}}{\sqrt{\rho_i} + \sqrt{\rho_{i+1}}} \quad \tilde{H} = \frac{\sqrt{\rho_i}H_i + \sqrt{\rho_{i+1}}H_{i+1}}{\sqrt{\rho_i} + \sqrt{\rho_{i+1}}} \quad \tilde{a} = \sqrt{(\gamma - 1)\left(\tilde{H} - \frac{1}{2}\tilde{u}^2\right)}. \tag{2.28}$$

Of further note is that Roe's Riemann solver does not distinguish between entropy-satisfying shockwaves and entropy violating shockwaves. This becomes a problem for centered expansion wave, when the $k^{th}$ acoustic wave has diverging characteristics of opposite sign, $\lambda_{k,i} < 0 < \tilde{\lambda}_k$ or $\tilde{\lambda}_k < 0 < \lambda_{k,i+1}$, and the interface flux should be computed from inside the expansion. In this work, the entropy fix of Harten and Hyman [27] is used, adjusting the eigenvalues as

$$\tilde{\lambda}_k = \begin{cases} \frac{1}{2}\left(\frac{\tilde{\lambda}_k^2}{\delta_k} + \delta_k\right) & \text{if } |\tilde{\lambda}_k| < \delta_k \\ |\tilde{\lambda}_k| & \text{otherwise} \end{cases} \tag{2.29}$$

$$\delta_k = \max(0, (\tilde{\lambda}_k - \lambda_{k,L}), (\lambda_{k,R} - \tilde{\lambda}_k)). \tag{2.30}$$

## 2.5 Capturing Shocks

With the Riemann solver defined, the Finite Volume method is complete and the structure of captured shockwaves can be examined. To represent a shockwave discretely, finite volume methods average, or capture, shocks over several cells. These captured shocks contain intermediate states that are are not part of the exact solution but are required for the discrete representation. While the number of required intermediate states varies from scheme to scheme and depends on the Courant number and Riemann solver [73, 91], among other things, all conservative schemes must produce them and they do not disappear with grid refinement.

In the representative example in Figure 2.3, the intermediate states are not connected to the shock end states by a single shock; instead, they are connected in part by waves of other families. As these intermediate states move, waves of all families

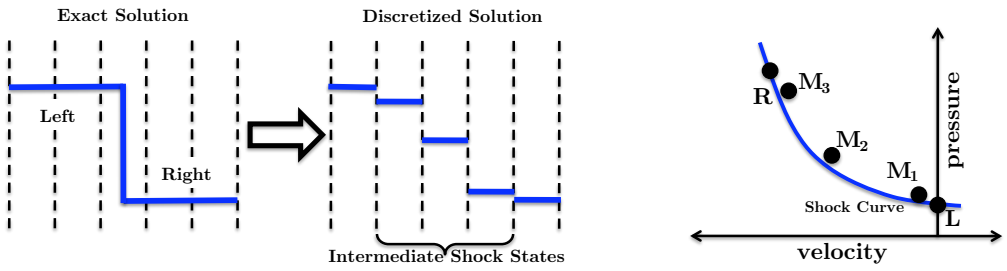


Figure 2.3: Representative single shock problem. (left) Exact Solution. (middle) Discretized exact solution for a single shockwave with resulting intermediate states.(right) Sample Hugoniot curve for the Euler Equations, and locations of intermediate states.

are created, and shed around the shock. These waves are largely responsible for the shock capturing anomalies described later in this work. In fact, the aptly named "start-up error" is a manifestation of the largest waves from this - in the first steps of simulations, the large jumps between shock states result in the strongest waves shed.

Of note for the Euler equations, is that wherever these intermediate states lie, they are always assumed to satisfy local thermal equilibrium in a cell-averaged sense, and therefore to obey the equilibrium equation of state (2.13). However, from the exact solution to the Navier-Stokes equations [103], it is known that local thermal equilibrium does not hold inside the shock itself. This suggests a form of 'interpretation' error, an error made in the philosophical approach taken when assigning meaning to the shock-captured solution.

Conservative schemes ensure that across an interface, physical quantities are passed from one cell to another with no losses. This does not however, guarantee correct shocks; it simply guarantees that errors on interfaces will cancel out [96]. This is why simulations of many problems result in the correct shock speed but incorrect shock location. Errors along the contact discontinuity are matched by errors in the shock, resulting in the correct shock states and shock speed, but incorrect shock position. To examine this and the role of intermediate shock states, the simplest case will be looked at first: the single stationary shock.

# CHAPTER III

# Shock-Capturing Anomalies

In this chapter, an analysis of shockwave structure in several canonical examples of anomalies in the Euler Equations is performed. Unlike previous analyses of these issues, these are analysed through a comparison with the stationary shockwave and an examination of the intermediate shock states. An ambiguity in sub-cell shock position is shown to be responsible for each anomaly, a claim further verified through the use of a system of equations with no such problem.

## 3.1 The Stationary Shock

To begin, a stationary (steady) shockwave can be constructed from the jump equations by choosing a left and right state such that the fluxes are equal, $\mathbf{f}(\mathbf{u}_L) = \mathbf{f}(\mathbf{u}_R)$. Allowing for $m$ intermediate states, $\mathbf{u}_1, \ldots, \mathbf{u}_j, \ldots, \mathbf{u}_m$, the stationary requirement from the semi-discretized form in Equation ((2.23)) is that all the interface fluxes are equal, that is

$$\mathbf{f}(\mathbf{u}_L) = \mathbf{f}(\mathbf{u}_L, \mathbf{u}_1) = \mathbf{f}(\mathbf{u}_1, \mathbf{u}_2) = \ldots = \mathbf{f}(\mathbf{u}_{m-1}, \mathbf{u}_m) = \mathbf{f}(\mathbf{u}_m, \mathbf{u}_R) = \mathbf{f}(\mathbf{u}_R) \qquad (3.1)$$

Choosing the left state with

$$\begin{aligned} \rho_L &= 1, \\ u_L &= 1, \\ p_L &= \frac{1}{\gamma M_L^2}, \end{aligned} \tag{3.2}$$

the corresponding right state for the shockwave is

$$\begin{aligned} \rho_R &= \frac{(\gamma+1)M_L^2}{(\gamma-1)M_L^2+2}, \\ u_R &= \frac{1}{\rho_R} = \frac{(\gamma-1)M_L^2+2}{(\gamma+1)M_L^2}, \\ p_R &= \frac{1}{\gamma M_L^2}\left(1+\frac{2\gamma}{\gamma+1}(M_L^2-1)\right). \end{aligned} \tag{3.3}$$

To examine the effect of the flux functions on the number of stationary states, the problem can be initialized with an arbitrary intermediate state and a fixed inflow boundary condition and run until steady state has been reached. Testing several common flux functions demonstrates the variable number of intermediate states and the dramatic effect of the choice of solver. Figure 3.1 show results for a Mach 10 shockwave and each flux function provides a different number of intermediate states but shares several key similarities, notably a significant momentum spike. Since no analytic representation of the set of stationary intermediate states exists for most flux functions, timestepping to steady state is required; thus there is no guarantee this is a unique set of intermediate states. This example just serves to represent the differences between several flux functions and their shock structure. As Roe's Riemann solver has the same single intermediate state as the exact Riemann solver [79, 5], it makes sense as the basis of the analysis.

The proof of a single intermediate state for both the exact and Roe's Riemann solver can be found in [79, 2, 84, 5]. A summary follows (see Figure 3.2). Defining the

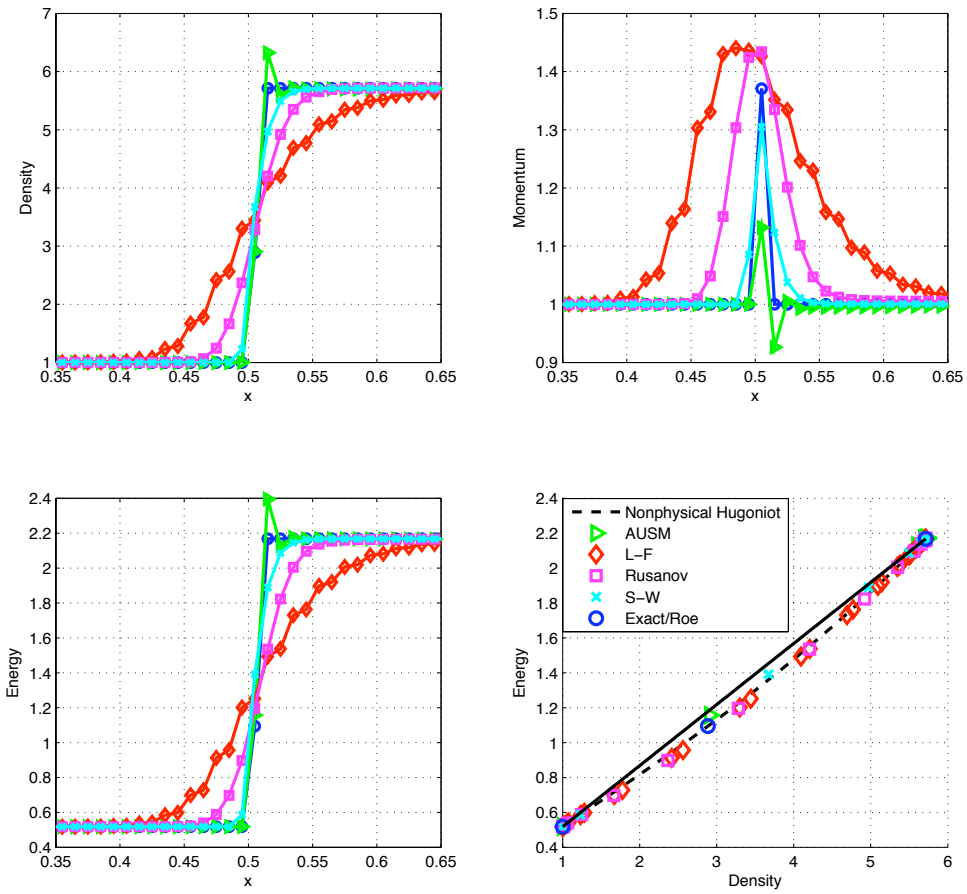


Figure 3.1: Comparison of results using various flux functions for a Mach 10 stationary shockwave. Results for Advection Upstream Splitting Method (AUSM) [50], Lax-Friedrichs (L-F) [45], Rusanov [81], Steger-Warming Flux Vector Splitting (S-W) [88], Roe [78], and the exact solver [91] are shown. A significant difference in shock structure is observed for each solver.

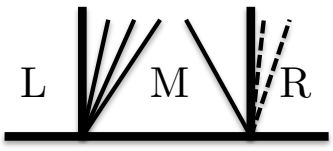


Figure 3.2: Wave diagram for the one-point stationary shockwave.

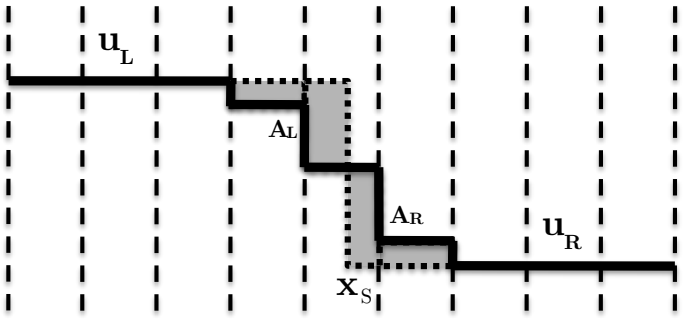


Figure 3.3: The equal area rule. For the conserved variable, $u$, the shock position, $x_S$, divides the discrete solution such that the two regions, $A_L$ and $A_R$ are equal in area.

intermediate state as $\mathbf{u}_M$, the requirement for the fluxes becomes $\mathbf{f}(\mathbf{u}_L) = \mathbf{f}(\mathbf{u}_L, \mathbf{u}_M) = \mathbf{f}(\mathbf{u}_M, \mathbf{u}_R) = \mathbf{f}(\mathbf{u}_R)$. On the LM interface, the flow is supersonic, so no left-going waves are generated at LM. On the MR interface, the compression from $\mathbf{u}_M$ to $\mathbf{u}_R$ is accomplished by a physical shock of the opposite family. This ensures that no right-going wave is generated at this interface and thus the set of possible states M lie on the nonphysical branch of the Hugoniot through R. All of the waves generated within the intermediate state remain trapped.

### 3.1.1 Ambiguity in Shock Position

So what is wrong with the stationary shock? Suppose a one-point shock was provided and one wanted to know the shock position within the cell. First, the method for computing shock position must be chosen. For a scalar conservation law, it can be determined using the equal-area rule [49] around the shock. As illustrated in Figure 3.3, the equal-area rule states that the shock position divides the discrete solution into two regions such that the integrated error in each region has the same absolute value. This comes directly from conservation principles and provides an unambiguous location for a shock that separates two uniform states.

One would hope that for a system of conservation laws a similar rule could be used to determine the shock position from any of the conserved variables, and that

these shock positions would agree, at least with each other if not the exact position. For the Euler equations, this is not the case. This is already known, although there does not seem to be any formal publication on the matter. The discrepancy can be proved for the aforementioned stationary shock.

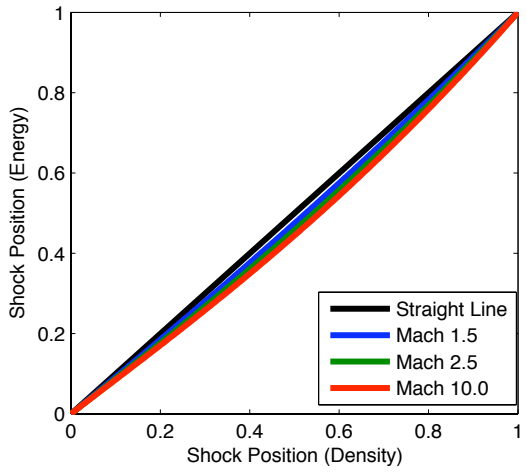


Figure 3.4: Shock position in energy vs shock position in density in the intermediate cell for initial Mach numbers of 1.5, 2.5, 4.0 and 10.0. The deviation from the straight line represents the ambiguity in shock position.

As the middle state is connected to the right state by the nonphysical branch of the Hugoniot, the shock position can be computed analytically by applying conservation of density or energy using

$$x_S(\rho) = \frac{\rho_M - \rho_R}{\rho_L - \rho_R} \qquad x_S(E) = \frac{E_M - E_R}{E_L - E_R}. \tag{3.4}$$

For the stationary shock in Equations (3.2) and (3.3), the family of middle states can be computed as in Kitamura, Roe, and Ismail [42] and Chauvat, Moschetta and

Gressier [8] by prescribing the shock position as $\varepsilon = 1 - x_S(\rho)$ and then

$$\begin{bmatrix} \rho_M \\ u_M \\ p_M \end{bmatrix} = \begin{bmatrix} \rho_L + \varepsilon(\rho_R - \rho_L) \\ u_L + \left(1 - (1 - x_S)\left(1 + \varepsilon \frac{M_L^2 - 1}{1 + \frac{\gamma-1}{2} M_L^2}\right)^{-\frac{1}{2}} \left(1 - \varepsilon \frac{M_L^2 - 1}{\frac{2\gamma}{\gamma-1} M_L^2 - 1}\right)^{-\frac{1}{2}}\right)(u_R - u_L) \\ p_L + \varepsilon \left(1 + (1 - \varepsilon)\frac{\gamma-1}{\gamma+1}\frac{M_L^2 - 1}{M_L^2}\right)^{-1}(p_R - p_L) \end{bmatrix} \tag{3.5}$$

Plots of $x_S(E)$ versus $x_S(\rho)$ are shown in Figure 3.4. At Mach 10, the maximum discrepancy is about $0.05\Delta x$ [1]. The situation is even worse if shock position is computed using momentum, because as the mass flux, it is equal for the left and right states, but not necessarily for the intermediate state. For the exact Riemann solver or Roe's Riemann solver, a momentum spike of as much as 40% is possible, and in general a spike is observed for all Riemann solvers, independent of the number of intermediate states, again, seen in Figure 3.1. Since the location of the intermediate state is due to the Hugoniot curve, so too is the ambiguity in shock position. If the Hugoniot were linear, there would be no ambiguity. This ambiguity can be directly related to each anomaly examined, starting with the wall heating phenomenon.

## 3.2 The Wall Heating Phenomenon

A notorious problem for those who compute high speed flow is the Noh problem [65], a seemingly trivial Riemann problem with initial data corresponding to the collision of two equal shocks, or equivalently the reflection of a single shock from a solid wall. The initial data is $\mathbf{u}_0 = (\rho_0, -\rho_0 u_0, E_0)^T$ but can be reduced to a one parameter family with Mach number as the free parameter and

$$\rho_0 = 1, \qquad u_0 = 1, \qquad p_0 = \frac{1}{\gamma M_0^2}. \tag{3.6}$$

[1] As the shock itself is $\mathcal{O}(1)$, an $\mathcal{O}(\Delta x)$ error in its position results in a much larger error than a classical error to a cell average in a smooth region of the solution, where the errors are $\mathcal{O}((\Delta x)^2)$.

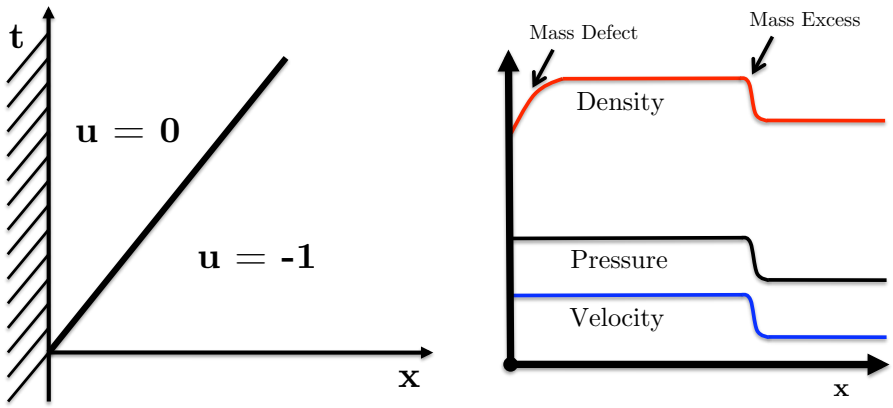


Figure 3.5: (left) Space-time representation of velocity in the Noh problem. (right) Representative solutions for the Noh problem after the shock has left the wall area. Note the density defect at the wall and corresponding density excess in the shock.

The solution behind the shock can be determined exactly from the jump conditions as

$$\rho = 1 + \frac{1}{S}, \qquad u = 0, \qquad p = p_0 + (1 + S), \tag{3.7}$$

with shock speed

$$S = \frac{1}{4}\left((\gamma - 3) + \sqrt{(\gamma + 1)^2 + 16\gamma p_0}\right). \tag{3.8}$$

Virtually all shock-capturing methods provide quite good solutions for pressure and velocity, but predict too small a density in a small region at the origin[2], as in Figure 3.5. In consequence the temperature there is too high, so that this and related phenomena have been called wall heating. In the more than thirty years since Noh proposed the problem, no satisfactory solution has been exhibited that would carry over to other settings, nor is there even any generally accepted explanation of the mechanism. The demonstration here is for a monatomic gas, with $\gamma = 5/3$.

After solving the Noh problem, letting the shockwave move sufficiently far from

[2]The difficulty is exacerbated by posing the problem in cylindrical or spherical geometry, but still occurs in one dimension. The one dimensional version is chosen for analysis to avoid the effects and complications of geometry or geometric source terms.

the wall such that the near wall region is at steady state, the shock position can be determined using the mass, momentum or energy in a control volume. Two control volumes are used to demonstrate the effect of shock position:

1. **Local** - contains only the region immediately around the shock.

2. **Global** - contains the whole domain, including the density defect.

Figures 3.6 and 3.7 show results for Mach 1.1 and $10^6$ shocks, calculated with a CFL number of 0.5. On the left, the complete solution for conserved variables is shown. In the middle, shock positions are calculated using a local control volume. All three conserved quantities produce different shock positions. The position calculated from the energy distribution agrees almost perfectly with the exact solution, but the position calculated from density is about $0.2\,\Delta x$ ahead of it. This can be interpreted as meaning that the shock contains excess mass.

On the right, shock positions have been calculated using the global control volume. The density and energy shock positions are equal, showing that the density defect observed at the wall exactly compensates the excess in the shock. With hindsight, this should have been expected. Conservation ensures that all of the mass that should be present really is present. Therefore, if it is deficient in one place it must be excessive in another. It seems plausible that if the ambiguity in shock position could be resolved, there might be no wall heating. In both control volumes, the shock position from momentum is computed incorrectly because while the wall boundary fluxes for mass and energy are zero, but the momentum flux includes pressure, which is incorrectly computed.

Further investigation into this problem leads to two key observations, as in Figure 3.8:

- The distance between shock positions computed by any two conserved variables is constant with time after the shock has settled.

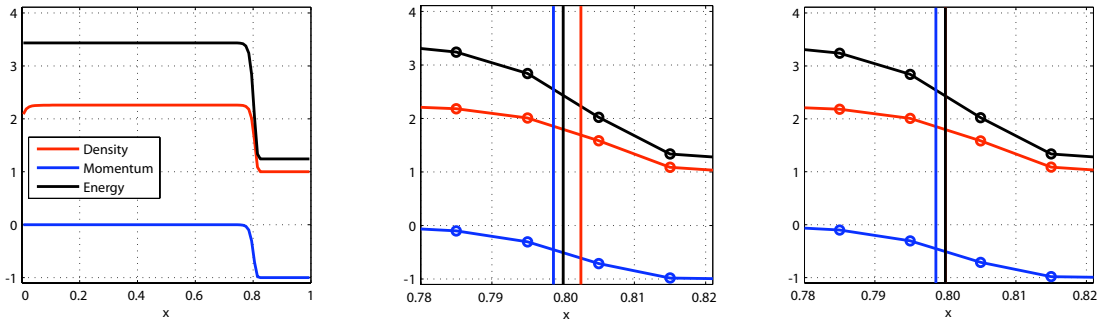


Figure 3.6: Conserved quantities for a Mach 1.1 shock. (left) Full solution. (middle) Sub-cell shock locations, denoted by vertical lines, computed using a local control volume. (right) Sub-cell shock locations computed using a global control volume.

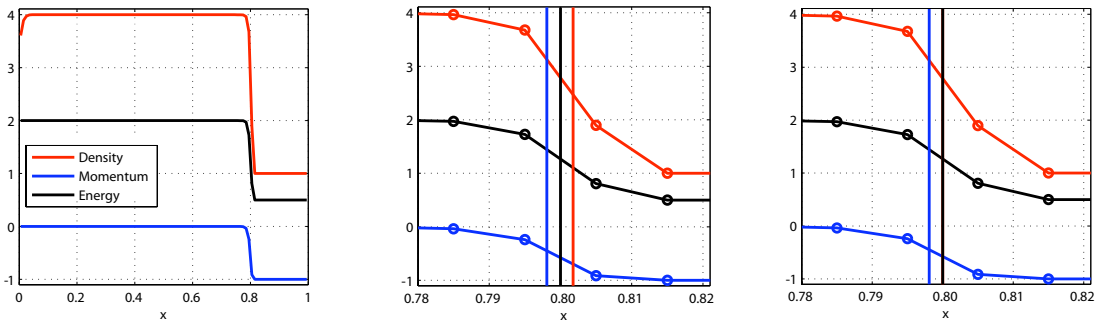


Figure 3.7: Conserved quantities for a Mach $10^6$ shock. Same three plots as Figure 3.6.

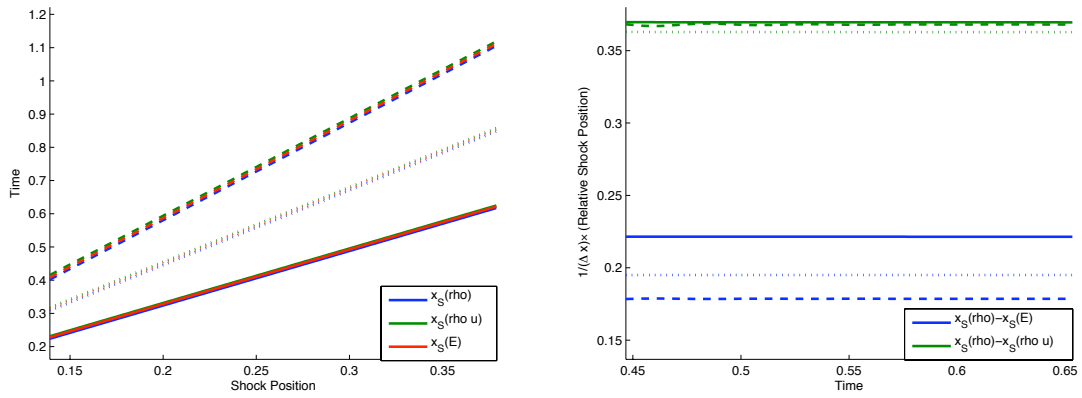


Figure 3.8: Results for Mach 1.5 (solid), Mach 2.5 (dotted), Mach 10.0 (dashed) shockwaves. (left) Shock position vs time. (right) Relative shock position vs time.

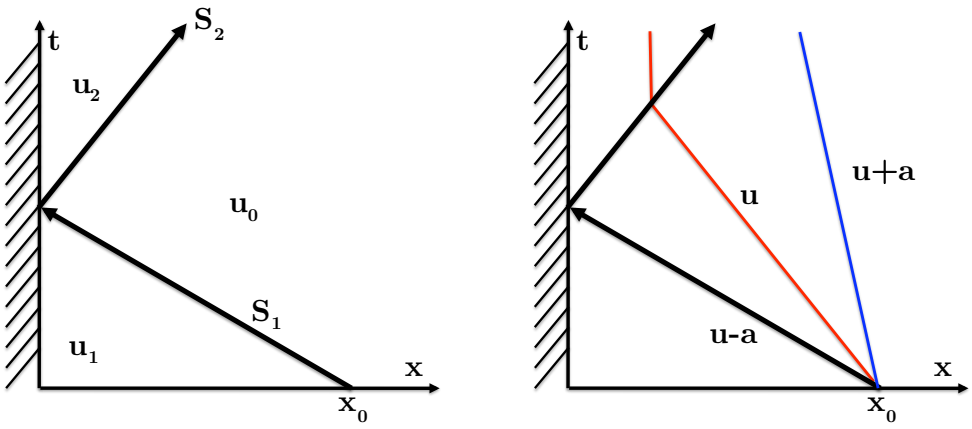


Figure 3.9: (left) Space-time illustration of the reflecting Noh problem, illustrating the three constant states present in the solution. (right) Space-time illustration of the waves produced - the start-up error is propagated along the $u$ and $u + a$ waves.

- The distance between shock positions computed by any two conserved variables is fairly independent of Mach number.

These observations demonstrate that despite the difference in sub-cell shock position, the shock speed in each conserved variable is the same and that while the shock strength may vary, the ambiguity remains the same and is directly compensated by the error at the wall. In other situations the 'missing mass' may appear somewhere else, but it will have to appear somewhere. The second observation would appear to contradict the theory in Section 3.1.1 that the ambiguity should get worse as the Mach number increases, however in the Noh problem, the moving shock now consists of multiple intermediate states and the theory for a single intermediate state does not apply. Nevertheless, since the ambiguity in shock position is directly related to the non-linearity of the jump conditions, so too is the wall heating phenomenon.

### 3.2.1 The Reflecting Noh Problem

Another variant of the Noh problem is the reflecting Noh problem. Developed for this work, the shock is started a prescribed distance away from the wall and allowed

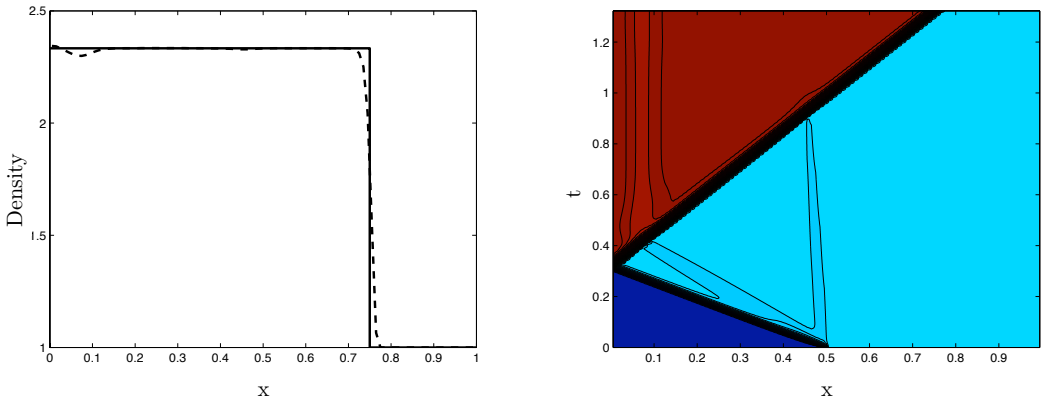


Figure 3.10: (left) Density for the reflected Noh problem after the reflected shock has moved away from the wall. (right) Space-Time contours of density.

to reflect off the wall, as in Figure 3.9. States $\mathbf{u}_0$ and $\mathbf{u}_2$ are the initial and post shock state from the original Noh problem, and $\mathbf{u}_1$ is chosen so that the velocity is zero and a single shock moves towards the wall, leading again to Equation (3.7), this time, the shock is of the opposite family, with speed

$$S_1 = \frac{1}{4}\left((\gamma - 3) - \sqrt{(\gamma+1)^2 + 16\gamma p_0}\right). \tag{3.9}$$

Unlike the original Noh problem, care needs to be taken to ensure that $p_1$ remains positive, in this case corresponding to an upper bound on the Mach number,

$$M_0^2 < \frac{2}{\gamma(\gamma-1)}. \tag{3.10}$$

Results for the Mach 1.17 shockwave are shown in Figure 3.10. The defect at the wall is now an overshoot, with the density defect spread to locations corresponding to the initial waves produced from the first shock. This demonstrates that the original Noh problem is a combination of a wall effect and the "start-up error", one of the most common forms of shock related error [35].

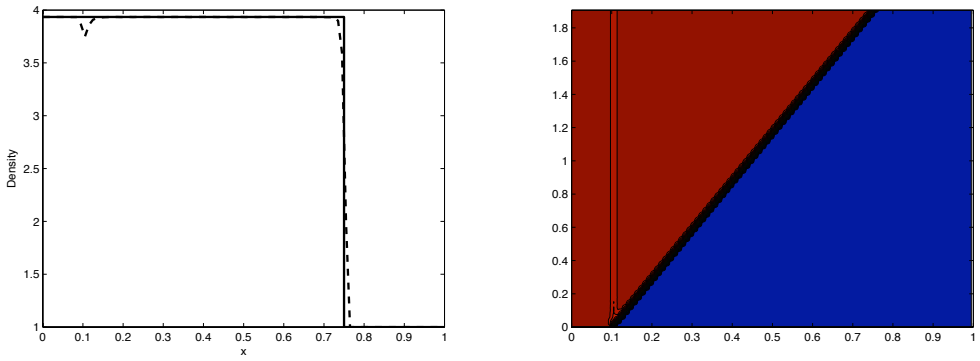


Figure 3.11: (left) Density profile for the single shock problem at time T =1.9. (right) Space-Time contours of density. The start up error is observed at $x = 0.1$.

### 3.2.2 The Start-up Error

The start-up error occurs in the initialization of a shockwave in a Riemann problem consisting of two states connected by a single shock where an initial wave is shed to allow the shockwave to reach a satisfactory shock structure. Initially, the shock position is identical for each conserved variable, thus to achieve the ambiguous shock structure the shockwave would like to have, waves must be shed.

Using any single shock Riemann problem, this error can be visualized. This will help understand where the missing mass actually goes to. The Noh problem is particularly good for this as the flow is stagnant behind the shock so errors that are produced along the contact discontinuity will remain within the flow domain. To initialize the problem, choose the left state from Equation (3.7) and the right state from Equation (3.6). Results are shown in Figure 3.11 for the problem initiated at $x = 0.1$ with an initial Mach number of 10.0. The start-up error is evident and while shock position is not shown, there must be an ambiguity with excess mass in the shock to compensate for the defect in density. Since

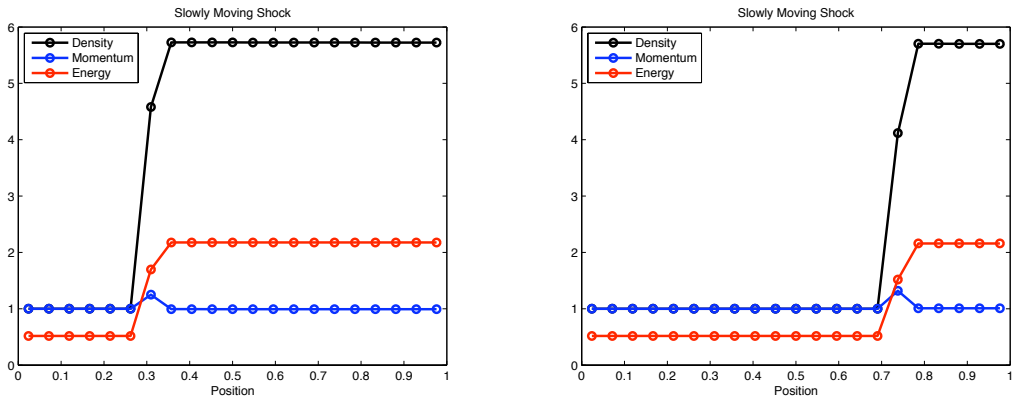


Figure 3.12: (left) A 1% perturbation to create a slowly moving shock moving to the left. (right) A 1% perturbation to create a slowly moving shock moving to the right.

## 3.3 The Slowly Moving Shockwave Phenomenon

Another known example of a numerical anomaly is the slowly moving shockwave phenomenon. Examined in detail by Roberts [73], Arora and Roe [1] and by Karni and Canic [38] among others, it is characterized by spurious waves that are thrown off by slowly moving shocks. These waves are purely numerical, but once created, they are propagated as though they were real. The cause of this phenomenon is that not all waves produced by solving Riemann problems involving the intermediate states are of the same family as the shockwave. While the term "slowly moving" can be interpreted in many ways, it is generally used to refer to shocks where the characteristics change sign across the shock, although in practice this is not a necessary condition.

To show that nonlinearity and sub-cell ambiguity are directly responsible for the spurious waves, experiments were conducted by slightly perturbing the stationary shock. This limiting case will be produced by prescribing the left state from the stationary shock defined in Equations (3.2) and (3.3). By slightly perturbing this right state along the direction of the Hugoniot, slowly moving shocks in either direction can be created. Figure 3.12 shows two equal and opposite perturbations of a Mach 10 stationary shockwave.

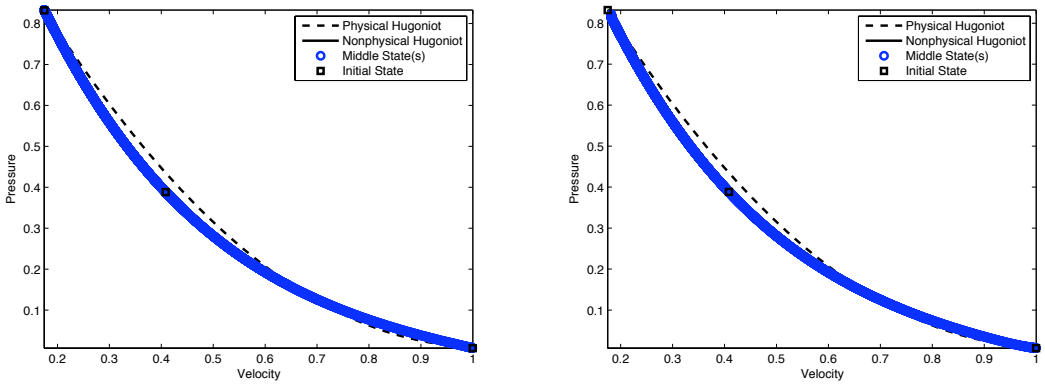


Figure 3.13: Intermediate states of the slowly moving shock in velocity-pressure space. While the intermediate states do not lie exactly on the nonphysical Hugoniot, they do lie slightly off of it, on a curve corresponding to two other end states. (left) Intermediate states of the left slowly moving shock. (right) Intermediate states of the right slowly moving shock.

In a previous investigation by Arora and Roe [1] plots were made in phase space showing every state that appears in the solution at any time step. This reveals the locus that is followed by the intermediate states. Some of the loci presented in [1] were highly intricate. Here, shockwaves were tested that moved even more slowly, to check that approaching the limit of zero speed causes the locus to approach the steady equilibrium locus. In other words, the goal was to determine if the slowly moving shock was a regular or singular perturbation of a stationary shock. In general, it seems that the perturbation was usually regular, with exceptions discussed in the next section, and not treated here.

Each snapshot of a slowly moving shock can then be viewed very closely as a sample of the stationary cases. Figure 3.13, shows that the locus for a shock moving very slowly to the left is the same as that for a shock moving very slowly to the right. This is independent of shock strength, so only results for the one shock are shown.

To see the connection with the curved Hugoniot, consider that as the shock moves across the grid, the amount of discrepancy between its positions, as calculated from each conserved variable, will change periodically. The discrepancy will repeat itself

every time that the shock has crossed one more cell. If this is interpreted as meaning that the shock has excess mass that varies with the same period, there must be, by conservation, a mass deficit elsewhere. This accounts for the periodic shedding of the spurious waves. With this connection made, the singular cases of the perturbed stationary shock can be examined.

## 3.4 The Carbuncle Phenomenon

Often in hypersonic flow computations, regions of anomalous shock structure occur, generically called "carbuncles". A related, and probably relevant, behavior can be seen in one dimension and is described as a 'one-dimensional carbuncle'. As analysed by Barth [2], Serre [84], and Dumbser et al. [12] not all of the equilibrium solutions (involving an intermediate state lying on the nonphysical Hugoniot through the right state) are stable. The attempt to compute a stationary shock at a position corresponding to one of these unstable equilibria results in a shock that does not remain stationary. Either the shock moves to a stable location, or, under suitable boundary conditions that exactly conserve mass, it enters into a limit cycle. That cycle involves the shedding of spurious waves and their reflection from the downstream boundary. These unstable equilibria only exist at high Mach numbers, with the critical Mach number for $\gamma = 7/5$ at about Mach 6.

As done previously, the intermediate point is specified by the shock position in density, $x_S$ and the shock is defined by Equations (3.2), (3.3) and (3.5). Several cases where the initial intermediate state lies off of either Hugoniot are tested to observe their behavior. Thus, cases are examined where the initial data corresponds to either a stable or an unstable location, and the initial profile does or does not represent an equilibrium solution. In Figure 3.14, four cases are shown.

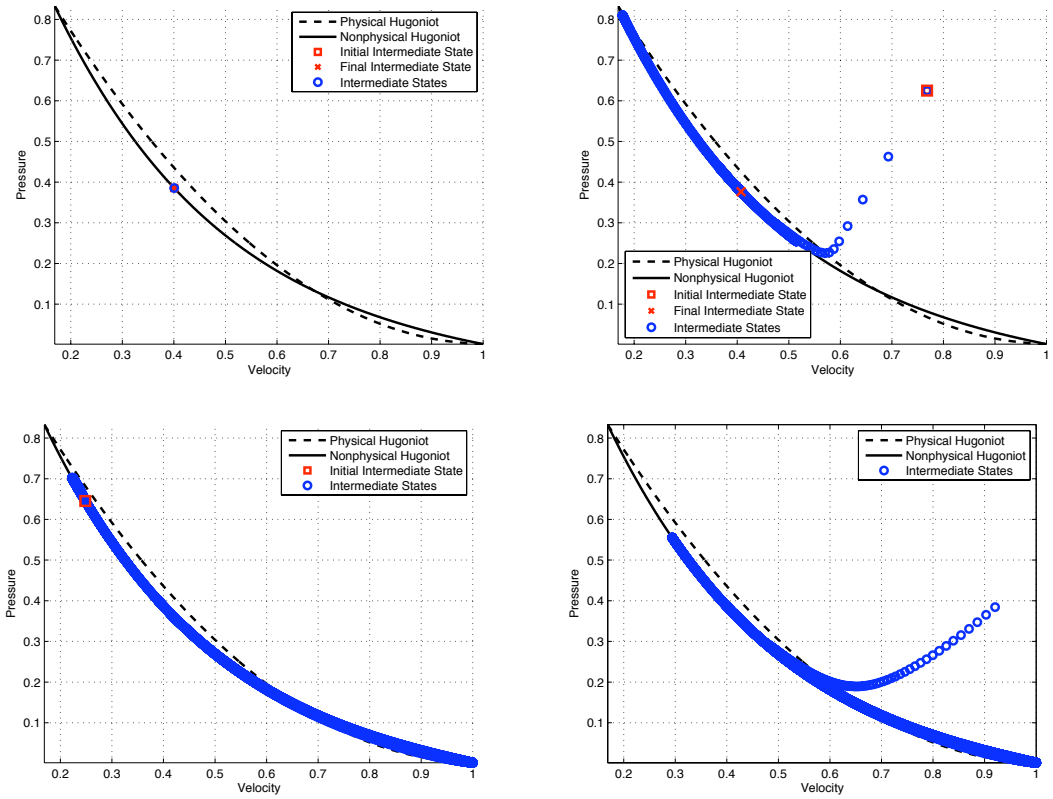


Figure 3.14: Intermediate states of the one-dimensional carbuncle for a Mach 20 shock. (top) Two carbuncle free cases. On the left, $x_S = 0.5$ and the initial intermediate state lies on the nonphysical Hugoniot. On the right, the initial intermediate state is off both Hugoniot curves.(bottom) Two cases with carbuncles. (left) $x_S = 0.8$. On the (right) the initial intermediate state is again off both Hugoniot curves.

**Stable location, equilibrium data** As would be expected, the method exactly preserves the initial data.

**Stable location, nonequilibrium data** The locus of intermediate states moves directly to the equilibrium locus and then travels along it to find the equilibrium that conserves mass.

**Unstable location, equilibrium data** The intermediate states "hunt" back and forth along the equilibrium curve, without finding a stable location.

**Unstable location, nonequilibrium data** The intermediate states track quickly onto the equilibrium locus, but are not able to find a stable location.

In those cases where no stable equilibrium exists, examining intermediate states reveals that all lie on the nonphysical Hugoniot curve, identical to those seen in Figure 3.13 for a left and right moving shockwave. Viewing the carbuncle in this frame, it is observed that in one dimension, it is no more than a slowly moving shock that is unable to find a stable position, moving in one direction and then the other within the cell. Since the slowly moving shock phenomenon is due to the nonlinearity of the Hugoniot curve and the resulting sub-cell ambiguity, the connection between the carbuncle and the ambiguity is made. Kitamura [42], however, showed that some methods were unstable in two dimensions even though stable in one dimension, so this cannot be a complete explanation.

## 3.5 A Linear Hugoniot?

If much of the odd behavior of captured shocks is associated with curvature of the Hugoniot, it is interesting to ask the question, 'what if the Hugoniot were linear?'. This is mathematically possible, even if the conservation laws are nonlinear. In fact, there is a substantial literature on "straight line systems", for example Temple [90] and Bressan and Jensen [4]. Arora and Roe [1] claimed that 2 x 2 systems with linear Hugoniots do not suffer from the slowly moving shock phenomenon. Here, a 3 x 3 system used as a model of magnetohydrodynamics by Myong and Roe [63] is examined. Defining three conserved quantities, $u, a$, and $b$, the system is

$$\frac{\partial}{\partial t}\begin{bmatrix} u \\ a \\ b \end{bmatrix} + \frac{\partial}{\partial x}\begin{bmatrix} \frac{1}{2}\left(u^2+a^2+b^2\right) \\ ua \\ ub \end{bmatrix} = \mathbf{0} \tag{3.11}$$

where $u$ is velocity-like and $a, b$ represent transverse magnetic fields and are kept positive to avoid the formation of compound waves. The flux Jacobian is

$$\mathbf{A} = \begin{bmatrix} u & a & b \\ a & u & 0 \\ b & 0 & u \end{bmatrix} \tag{3.12}$$

with eigendecomposition

$$\Lambda = \begin{bmatrix} u-c & 0 & 0 \\ 0 & u & 0 \\ 0 & 0 & u+c \end{bmatrix}, \qquad \mathbf{R} = \begin{bmatrix} -c & 0 & c \\ a & -b & a \\ b & a & b \end{bmatrix} \tag{3.13}$$

and propagation speed $c = \sqrt{a^2 + b^2}$ (which is also conserved). The Riemann invariants are

$$\mathbf{L}\mathrm{d}\mathbf{u} = \frac{1}{c^2} \begin{bmatrix} \frac{1}{2}c(-\mathrm{d}u + \mathrm{d}c) \\ -b\mathrm{d}a + a\mathrm{d}b \\ \frac{1}{2}c(\mathrm{d}u + \mathrm{d}c) \end{bmatrix}. \tag{3.14}$$

In this system, the jump conditions simplify to the linear relation $u_L \pm c_L = u_R \pm c_R$. This relation is identical to the invariant for a expansion wave, $\mathrm{d}u \pm \mathrm{d}c = 0$, thus conserved quantities through expansion waves and shockwaves come from different branches of the same curve. This is a truly remarkable property, and one of the reasons this system is examined. Along with shockwaves and expansions, there is also a contact discontinuity, with both $u$ and $c$ constant across it, and jumps in $a$ and $b$. Since both the physical and nonphysical Hugoniot are linear and identical, it is expected that there would be agreement in shock position and that there would be no evidence of any of the aforementioned phenomena. Indeed this is the case.

Only results for a Noh-like problem and the slowly moving shock are shown, since there is no ambiguity in stationary shock position and an exhaustive numerical study

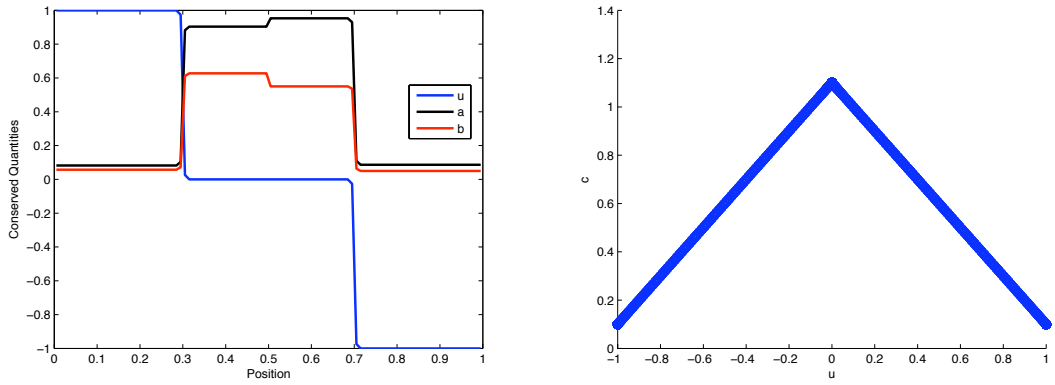


Figure 3.15: The Noh-like problem for Equations (3.11) with Mach 10. On the left, the solution after the reflecting shocks have moved sufficiently far away from the wall. While there are jumps in $a$ and $b$ across the contact discontinuity, there is no error present. On the right, all solution states are plotted in $c$ vs $u$ space. All states lie on either Hugoniot curve.

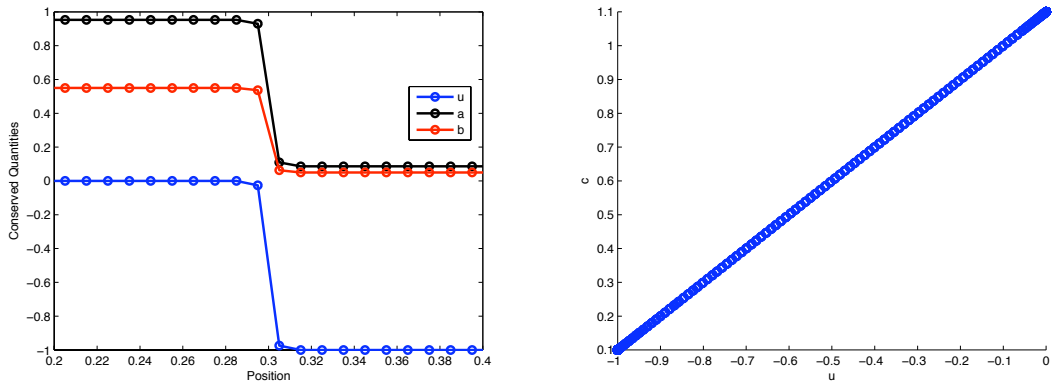


Figure 3.16: The Slowly moving shock problem for Equations (3.11) with Mach 10. (left) The solution after the shock has passed through several cells. (right) All solution states are plotted in $c$ vs $u$ space. All states lie on the correct Hugoniot curve.

of carbuncle-like issues reveals no evidence of any similar problem. For the Noh problem, an analogous symmetric problem with two reflecting shockwaves separated by a stationary contact discontinuity is constructed. In Figure 3.15, there is no error made along the contact discontinuity, and thus no 'wall heating'-like behavior. In Figure 3.16, a single shock moves slowly through the domain. In both problems, there are no spurious waves shed, and all intermediate states lie on the Hugoniot. While this system does not prove that nonlinearity is the sole cause of all of these issues, it suggests that correct placement of intermediate states may result in better solutions and the alleviation of many numerical shockwave anomalies.

## 3.6 Summary

In this chapter, four well established numerical phenomenon were connected to the nonlinearity of the Rankine-Hugoniot jump conditions through two main effects. First, the effect of sub-cell shock location ambiguity was noted for the stationary shock, and the connection to wall heating was shown. The inconsistency in shock position was shown to be exactly compensated by the inconsistency at the wall. Second, slowly moving shockwaves were examined, and by simply perturbing a stationary shock, the phenomenon was observed. An investigation into the one dimensional carbuncle showed that in one dimension, it behaves like a trapped slowly moving shock. Although this is not enough to establish a causal connection, it is certainly intriguing, given that all these phenomena can be linked to the nonlinearity in the Hugoniot curve. Finally, a model system was described with linear jump conditions and shown not to suffer any of the numerical shock anomalies prevalent in Euler solutions. This strengthens the belief that it is the nonlinearity of the Hugoniot which has led to these problems.

# CHAPTER IV

# New Flux Functions

The goal is to construct a flux function that would avoid the anomalies studied. Since all of these anomalies can be largely traced to the ambiguity in shock position within the stationary shock, it seems that a scheme that allows for one point stationary shocks and no positional ambiguity would alleviate, if not remove these problems. Ideally, the flux would follow the classic form, $\mathbf{f}_{i+\frac{1}{2}} = \mathbf{f}(\mathbf{u}_i, \mathbf{u}_{i+1})$ however, it is likely that this will not be possible. After a detailed investigation, it is apparent there is no Riemann solver (two-state flux function) yielding a one-point stationary shock such that the intermediate state is only on a straight line connecting the left and right state.

To compute interface fluxes, the idea of a flux function, $\mathbf{f}_{i+\frac{1}{2}} = \mathbf{f}(\mathbf{u}_{i-m}, \ldots, \mathbf{u}_{i+n})$, rather than a Riemann solver is needed. Since the intermediate shock states have no true physical meaning, only serving to connect the endpoints of the shock, it seems logical to begin by determining how much of these states to trust. The conserved quantities should be trusted, if for no other reason than to preserve conservation of the system, however there is freedom in the choice of the flux allocated to each cell. This abandons the condition of local thermodynamic equilibrium for these intermediate states, a reasonable idea since it does not hold within a real physical shock. This will be done by defining an alternate definition of flux within a shock, referred to

herein on as an interpolated flux, and denoted by $\mathbf{f}^*$. Inside a one-point stationary shock, the interpolated flux is constructed such that $\mathbf{f}_M^* = \mathbf{f}_L = \mathbf{f}_R$ when there is no ambiguity. With this definition in place, two interface flux functions are designed to utilize interpolated fluxes and preserve the stationary property.

## 4.1 Interpolated Fluxes

The first step is to define interpolated fluxes, $\mathbf{f}_i^*$, that behave more smoothly near shocks than the actual fluxes. The interpolated fluxes are constructed to have the following properties:

1. If the problem is linear so that the Jacobian matrix $\mathbf{A}(\mathbf{u})$ is constant, then $\mathbf{f}_i^* = \mathbf{f}_i$, the interpolated flux equals the equilibrium flux, $\mathbf{f}(\mathbf{u}_i)$.

2. If the problem is nonlinear, but the data is smooth, then $\mathbf{f}_i^* = \mathbf{f}_i + \mathcal{O}((\Delta x)^2)$.

3. If the problem is nonlinear and involves a one-point stationary shock, then $\mathbf{f}_i^*$ is constant, not only on each side of the shock, but also in the intermediate cell, unlike the equilibrium flux.

To begin, suppose the flux is interpolated from one side as

$$\mathbf{f}_i^* = \mathbf{f}_{i-1} + \tilde{\mathbf{A}}_i(\mathbf{u}_i - \mathbf{u}_{i-1}) \tag{4.1}$$

for some choice of flux Jacobian, $\tilde{\mathbf{A}}_i$, and interpolated from the other side as

$$\mathbf{f}_i^* = \mathbf{f}_{i+1} - \tilde{\mathbf{A}}_i(\mathbf{u}_{i+1} - \mathbf{u}_i). \tag{4.2}$$

These two equations are consistent if

$$\mathbf{f}_{i+1} - \mathbf{f}_{i-1} = \tilde{\mathbf{A}}_i(\mathbf{u}_{i+1} - \mathbf{u}_{i-1}). \tag{4.3}$$

The simplest matrix having this property is the cell-centered Roe matrix, similar to the edge-based Roe matrix defined in Section 2.4. Averaging Equations (4.1) and (4.2) leads to a centered construction of the interpolated flux

$$\mathbf{f}_i^* = \frac{1}{2}(\mathbf{f}_{i-1} + \mathbf{f}_{i+1}) - \frac{1}{2}\tilde{\mathbf{A}}_{i-1,i+1}(\mathbf{u}_{i+1} - 2\mathbf{u}_i + \mathbf{u}_{i-1}). \tag{4.4}$$

With the definition in place, it is simple to show that for a captured stationary shock having one intermediate state with no positional ambiguity, the interpolated flux is identical everywhere. To avoid ambiguity, the intermediate state must be a linear combination of the left and right states

$$\mathbf{u}_M = x_S\mathbf{u}_L + (1 - x_S)\mathbf{u}_R \tag{4.5}$$

for $x_S \in [0, 1]$, where $\mathbf{f}(\mathbf{u}_L) = \mathbf{f}(\mathbf{u}_R)$ and $\tilde{\mathbf{A}}_{LR}(\mathbf{u}_R - \mathbf{u}_L) = \mathbf{f}_R - \mathbf{f}_L = \mathbf{0}$. The interpolated fluxes computed using Equation (4.1) are

$$\mathbf{f}_L^* = \mathbf{f}_L + \tilde{\mathbf{A}}_{LM}(\mathbf{u}_L - \mathbf{u}_L) = \mathbf{f}_L \tag{4.6}$$

$$\mathbf{f}_M^* = \mathbf{f}_L + \tilde{\mathbf{A}}_{LR}(\mathbf{u}_M - \mathbf{u}_L) = \mathbf{f}_L + (1 - x_S)\tilde{\mathbf{A}}_{LR}(\mathbf{u}_R - \mathbf{u}_L) = \mathbf{f}_L \tag{4.7}$$

$$\mathbf{f}_R^* = \mathbf{f}_M + \tilde{\mathbf{A}}_{MR}(\mathbf{u}_R - \mathbf{u}_M) = \mathbf{f}_M + \mathbf{f}_R - \mathbf{f}_M = \mathbf{f}_R = \mathbf{f}_L \tag{4.8}$$

Identical results are obtained using Equations (4.2) or (4.4). While it is clear that a non-monotone shock structure ($x_S \notin [0, 1]$) will also lead to the same result, this results in a rarefaction shock at either the left-middle or middle-right edge. Any measure that eliminates rarefaction shocks will therefore eliminate the non-monotone solutions.

Having verified that using interpolated fluxes gives the unambiguous stationary shock structure, more of the mathematical properties of the interpolated fluxes can be examined. Taking a Taylor series expansion of the centered form in Equation (4.4)

results in

$$\mathbf{f}_i^* \approx \mathbf{f}_i + \frac{(\Delta x)^2}{2}(\mathbf{f}_{xx} - \tilde{\mathbf{A}}_i \mathbf{u}_{xx}). \tag{4.9}$$

With the first and second derivatives of the flux expressed as $\mathbf{f}_x = \mathbf{A}\mathbf{u}_x$ and $\mathbf{f}_{xx} = \mathbf{A}_x\mathbf{u}_x + \mathbf{A}\mathbf{u}_{xx}$, this can be further simplified to

$$\mathbf{f}_i^* = \mathbf{f}_i + \frac{(\Delta x)^2}{2}(\mathbf{A}_x\mathbf{u}_x + (\mathbf{A} - \tilde{\mathbf{A}}_i)\mathbf{u}_{xx}). \tag{4.10}$$

Since $\tilde{\mathbf{A}}_i$ is a symmetric centered average of $\mathbf{A}_i$, it can be expanded as $\tilde{\mathbf{A}}_i = \mathbf{A}_i + \mathcal{O}(h^2)$ and finally the interpolated flux can be written simply as

$$\mathbf{f}_i^* = \mathbf{f}_i + \frac{(\Delta x)^2}{2}\mathbf{A}_x\mathbf{u}_x + \mathcal{O}((\Delta x)^4) = \mathbf{f}_i + \frac{1}{2}(\Delta\mathbf{A})(\Delta\mathbf{u}) + \mathcal{O}((\Delta x)^2), \tag{4.11}$$

a second-order correction to the flux, corrected by the product of the derivatives of the flux Jacobian and conserved variables.

## 4.2 New Flux Function - A

With interpolated fluxes defined, a new flux function can be described similar to the original Roe framework, referred to as new flux function A,

$$\mathbf{f}^A_{i+\frac{1}{2}} = \frac{1}{2}(\mathbf{f}_i^* + \mathbf{f}_{i+1}^*) - \frac{1}{2}\text{sign}(\tilde{\mathbf{A}}_{i+\frac{1}{2}})(\mathbf{f}_{i+1}^* - \mathbf{f}_i^*) \tag{4.12}$$

with Roe's Riemann solver obtained if $\mathbf{f}_i^* = \mathbf{f}_i$. Thus the new method recovers Roe's method for linear problems or smooth solutions. Physically speaking, this new function trusts the values of the conserved quantities, but does not necessarily trust the flux functions, and corrects them in the vicinity of a shock.

Flux function A can be expanded as

$$
\begin{aligned}
\mathbf{f}^{A}_{i+\frac{1}{2}} &= \frac{1}{2}(\mathbf{f}^{*}_{i} + \mathbf{f}^{*}_{i+1}) - \frac{1}{2}\text{sign}(\tilde{\mathbf{A}}_{i+\frac{1}{2}})(\mathbf{f}^{*}_{i+1} - \mathbf{f}^{*}_{i}) && (4.13)\\
&= \frac{1}{2}\left(\mathbf{f}_{i+1} - \tilde{\mathbf{A}}_{i}(\mathbf{u}_{i+1} - \mathbf{u}_{i}) + \mathbf{f}_{i} + \tilde{\mathbf{A}}_{i+1}(\mathbf{u}_{i+1} - \mathbf{u}_{i})\right) \\
&\quad -\frac{1}{2}\text{sign}(\tilde{\mathbf{A}}_{i+\frac{1}{2}})\left(\mathbf{f}_{i} + \tilde{\mathbf{A}}_{i+1}(\mathbf{u}_{i+1} - \mathbf{u}_{i}) - \mathbf{f}_{i+1} + \tilde{\mathbf{A}}_{i}(\mathbf{u}_{i+1} - \mathbf{u}_{i})\right) && (4.14)\\
&= \frac{1}{2}(\mathbf{f}_{i+1} + \mathbf{f}_{i}) + \frac{1}{2}(\tilde{\mathbf{A}}_{i+1} - \tilde{\mathbf{A}}_{i})(\mathbf{u}_{i+1} - \mathbf{u}_{i}) \\
&\quad -\frac{1}{2}\text{sign}(\tilde{\mathbf{A}}_{i+\frac{1}{2}})(\mathbf{f}_{i} - \mathbf{f}_{i+1} + (\tilde{\mathbf{A}}_{i+1} + \tilde{\mathbf{A}}_{i})(\mathbf{u}_{i+1} - \mathbf{u}_{i})) && (4.15)\\
&= \frac{1}{2}(\mathbf{f}_{i+1} + \mathbf{f}_{i}) - \frac{1}{2}|\tilde{\mathbf{A}}_{i+\frac{1}{2}}|(\mathbf{u}_{i+1} - \mathbf{u}_{i}) + \frac{1}{2}\left((\mathbf{I} - \text{sign}(\tilde{\mathbf{A}}_{i+\frac{1}{2}}))\tilde{\mathbf{A}}_{i+1}\right. \\
&\quad \left.-(\mathbf{I} + \text{sign}(\tilde{\mathbf{A}}_{i+\frac{1}{2}}))\tilde{\mathbf{A}}_{i} + 2|\tilde{\mathbf{A}}_{i+\frac{1}{2}}|\right)(\mathbf{u}_{i+1} - \mathbf{u}_{i}). && (4.16)
\end{aligned}
$$

The first two terms in Equation (4.16) are Roe's original solver and the third term contains a "viscosity"-like matrix. This matrix is proportional to $\partial_x \mathbf{A} \partial_x \mathbf{u}$ and vanishes for linear systems, is second-order for nonlinear systems, and contributes a third-order effect in smooth regions. Close to a shock, this term is $\mathcal{O}(1)$ and has a first-order effect, as it must. In fact, for any Riemann problem, the viscosity term is zero and the new flux function reduces to Roe's Riemann Solver.

### 4.2.1 Observations

#### 4.2.1.1 Continuity of the Flux Function

There are two obvious issues with this formulation. First off is through the diffusion component of the Riemann solver, $\text{sign}(\tilde{\mathbf{A}}_{i+\frac{1}{2}})(\mathbf{f}^{*}_{i+1} - \mathbf{f}^{*}_{i})$. In this term, since the interpolated flux difference is computed with different quantities than the flux Jacobian and the sign function is discontinuous, the flux function is not continuous either. This is a particular problem when eigenvalues of $\tilde{\mathbf{A}}_{i+\frac{1}{2}}$ are very close to zero, where small errors can result in a sign change. To alleviate this problem, a standard

approximation is used, defining the sign function as

$$\text{sign}(x) \approx \frac{x}{\sqrt{x^2 + \varepsilon^2}} \tag{4.17}$$

where in this thesis, experience suggests a choice of $\varepsilon^2 \approx \mathcal{O}(10^{-8})$.

#### 4.2.1.2 Expansion Shockwaves

To no surprise, as the flux function uses a Roe matrix, it cannot distinguish between a physical shock and an expansion shock. Since adjusting the magnitude of the wavespeeds does not make a difference, a variant of the entropy fix in Equation (2.30) is used, with an additional diffusive term containing the adjusted wavespeeds

$$\mathbf{f}^{entropy}_{i+\frac{1}{2}} = -\frac{1}{2}\mathbf{R}_{i+\frac{1}{2}}|\delta\mathbf{\Lambda}_{i+\frac{1}{2}}|\mathbf{L}_{i+\frac{1}{2}}(\mathbf{u}_{i+1} - \mathbf{u}_i) \tag{4.18}$$

added to the flux function.

## 4.3 New Flux Function - B

To overcome the difficulties of new flux function A, another flux function, B, is developed. Inspired by Roe's Riemann solver, it can be written as

$$\mathbf{f}^{B}_{i+\frac{1}{2}} = \frac{1}{2}(\mathbf{f}^{*}_{i} + \mathbf{f}^{*}_{i+1}) - \frac{1}{2}|\overline{\mathbf{A}}_{i+\frac{1}{2}}|(\mathbf{u}_{i+1} - \mathbf{u}_i) \tag{4.19}$$

where $\overline{\mathbf{A}}_{i+\frac{1}{2}}$ is the Roe matrix across cells $i-1$ and $i+2$,

$$\overline{\mathbf{A}}_{i+\frac{1}{2}}(\mathbf{u}_{i+2} - \mathbf{u}_{i-1}) = \mathbf{f}_{i+2} - \mathbf{f}_{i-1} \tag{4.20}$$

It is clear that this flux function allows for a one-point stationary shock if the intermediate state is collinear with the end states in state space since at every interface,

the difference in conserved variables is either zero or a null vector of the Roe matrix that spans the left and right states. Just like flux function A, this reduces to Roe's Riemann solver for a single jump in data. For this function, an entropy fix is more traditional since it can be included directly within the Roe matrix. Flux function B can also be written as a correction to Roe's Riemann solver as

$$\begin{aligned}
\mathbf{f}^B_{i+\frac{1}{2}} &= \frac{1}{2}(\mathbf{f}^*_i + \mathbf{f}^*_{i+1}) - \frac{1}{2}\left|\overline{\mathbf{A}}_{i+\frac{1}{2}}\right|(\mathbf{u}_{i+1} - \mathbf{u}_i) && (4.21)\\
&= \frac{1}{2}\left(\mathbf{f}_{i+1} - \tilde{\mathbf{A}}_i(\mathbf{u}_{i+1} - \mathbf{u}_i) + \mathbf{f}_i + \tilde{\mathbf{A}}_{i+1}(\mathbf{u}_{i+1} - \mathbf{u}_i)\right)\\
&\quad -\frac{1}{2}|\overline{\mathbf{A}}_{i+\frac{1}{2}}|(\mathbf{u}_{i+1} - \mathbf{u}_i) && (4.22)\\
&= \frac{1}{2}(\mathbf{f}_i + \mathbf{f}_{i+1}) - \frac{1}{2}|\tilde{\mathbf{A}}_{i+\frac{1}{2}}|(\mathbf{u}_{i+1} - \mathbf{u}_i)\\
&\quad +\frac{1}{2}\left(|\tilde{\mathbf{A}}_{i+\frac{1}{2}}| + \tilde{\mathbf{A}}_{i+1} - \tilde{\mathbf{A}}_i - |\overline{\mathbf{A}}_{i+\frac{1}{2}}|\right)(\mathbf{u}_{i+1} - \mathbf{u}_i) && (4.23)
\end{aligned}$$

## 4.4 Burgers' Equation

While the new methodology is designed for the Euler equations, it is important to understand its effect on simpler models. The simplest scalar, nonlinear hyperbolic equation, Burgers' equation is a model equation for simple waves of the Euler equations. While not susceptible to the anomalous behavior of interest, it is important to ensure the new methods do not harm its solutions and still maintain a reasonable solution quality.

In the inviscid limit, the equation for the velocity $u(x,t)$ can be written as

$$u_t + f_x = u_t + \left(\frac{1}{2}u^2\right)_x = u_t + uu_x = 0. \tag{4.24}$$

The velocity is convected with speed $u$ so that continuous solutions satisfy

$$u(x,t) = u_0(x - u(x,t)t) \tag{4.25}$$

for initial condition $u(x,0) = u_0(x)$. Shockwaves are represented by the jump conditions $\Delta(\frac{1}{2}u^2) = S\Delta u$ and move with speed $S = \frac{1}{2}(u_L + u_R)$. The Roe-averaged velocity is just the arithmetic average, $\tilde{u} = \frac{1}{2}(u_L + u_R)$. Since there is only variable, there can be no ambiguity in shock position. The interpolated flux for this system is

$$\begin{aligned} f_i^* &= \frac{1}{2}(f_{i+1} + f_{i-1}) - \frac{1}{4}(u_{i-1} + u_{i+1})(u_{i+1} - 2u_i + u_{i-1}) && (4.26) \\ &= \frac{1}{4}\left[u_{i+1}^2 + u_{i-1}^2 - (u_{i-1} + u_{i+1})(u_{i+1} - 2u_i + u_{i-1})\right] && (4.27) \\ &= \frac{1}{2}[u_i(u_{i+1} + u_{i-1}) - u_{i-1}u_{i+1}] && (4.28) \end{aligned}$$

The interpolated flux is not without its flaws. This flux may be negative and therefore not realizable. This will happen if

$$\frac{(u_{i+1} + u_{i-1})u_i}{u_{i+1}u_{i-1}} < 1, \tag{4.29}$$

represented by the unshaded part of Figure 4.1 as a function of the ratios of data from neighboring cells, $u_{i-1}/u_i$ and $u_{i+1}/u_i$. Clearly such data will only arise exceptionally, but perhaps the interpolated flux should be avoided for these cases. If so, there may be situations where a similar difficulty arises for the Euler equations.

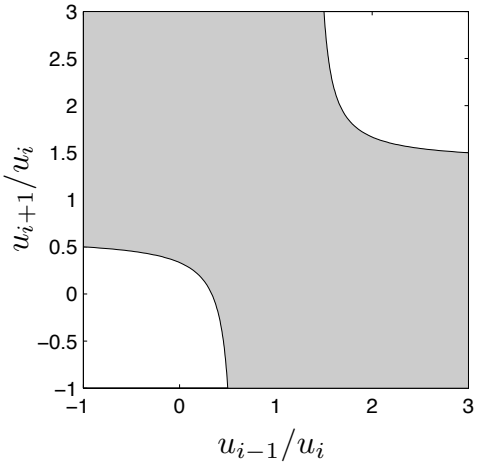


Figure 4.1: Physically realizable region of interpolated flux for Burgers' Equation

Writing both new flux functions can be done by first expanding the sum of interpolated fluxes,

$$f_i^* + f_{i+1}^* = \frac{1}{2}(u_i^2 + u_{i+1}^2) + \frac{1}{2}((u_{i+2} - u_{i-1}) - (u_{i+1} - u_i))(u_{i+1} - u_i) \tag{4.30}$$

and putting it together as

$$f_{i+\frac{1}{2}}^A = \frac{1}{2}(f_i^* + f_{i+1}^*) - \frac{1}{4}\text{sign}(u_{i+1} + u_i)(u_{i+2} + u_{i-1})(u_{i+1} - u_i) \tag{4.31}$$

$$f_{i+\frac{1}{2}}^B = \frac{1}{2}(f_i^* + f_{i+1}^*) - \frac{1}{4}|u_{i-1} + u_{i+2}|(u_{i+1} - u_i). \tag{4.32}$$

This illustrates that the difference between flux functions A and B is in the choice of wavespeed used within the sign function.

### 4.4.1 Total Variation Diminishing

First introduced by Harten [26] total variation diminishing (TVD) is a property of numerical schemes that ensures they preserve monotonicity and do not create local extrema. Initially introduced as total variation non-increasing, it was developed as a property to establish the convergence of finite difference schemes to weak solutions. These days, it has taken on a more general meaning of 'nice', is a good property to have and has been influential in the design of many numerical methods.

Defining the discrete total variation as

$$TV(u) = \sum_i |u_i - u_{i-1}|, \tag{4.33}$$

a method is TVD if

$$TV(u^{n+1}) \leq TV(u^n). \tag{4.34}$$

The approach used to determine whether the new flux functions are TVD is based

on the original work of Harten [22]. The flux functions are said to be TVD if

$$\frac{\Delta t}{\Delta x}\left|\frac{f^*_{i+1}-f^*_i}{u_{i+1}-u_i}\right| \leq q^*_{i+\frac{1}{2}} \leq 1 \tag{4.35}$$

is satisfied, where $q^*_{i+\frac{1}{2}}$ is the numerical viscosity coefficient obtained by writing the flux function in the form

$$f_{i+\frac{1}{2}} = \frac{1}{2}(f^*_i + f^*_{i+1}) - \frac{1}{2}\frac{\Delta x}{\Delta t} q^*_{i+\frac{1}{2}}(u_{i+1}-u_i). \tag{4.36}$$

This condition for TVD simplifies to

$$\frac{1}{2}\frac{\Delta t}{\Delta x}\left|u_{i+2}+u_{i-1}\right| \leq q^*_{i+\frac{1}{2}} \leq 1 \tag{4.37}$$

and the new flux functions can be checked. For flux function A, the viscosity coefficient is

$$q^{*,A}_{i+\frac{1}{2}} = \frac{1}{2}\frac{\Delta t}{\Delta x}\mathrm{sign}(u_{i+1}+u_i)(u_{i+2}+u_{i-1}) \tag{4.38}$$

and the lower bound of Equation (4.37) reduces to

$$\left|(u_{i+2}+u_{i-1})\right| \leq \mathrm{sign}(u_{i+1}+u_i)\mathrm{sign}(u_{i+2}+u_{i-1})\left|(u_{i+2}+u_{i-1})\right|. \tag{4.39}$$

and thus flux function A is not TVD, since this condition does not hold for all data. For flux function B, the viscosity coefficient is

$$q^{*,B}_{i+\frac{1}{2}} = \frac{1}{2}\frac{\Delta t}{\Delta x}|u_{i-1}+u_{i+2}| \tag{4.40}$$

and the lower bound of Equation (4.37) is trivially satisfied, therefore flux function B is TVD by this approach. For both flux functions, the upper bound is a CFL-like

condition and can be satisfied through the proper choice of timestep.

This analysis demonstrates an advantage of flux function B and suggests where changes to flux function A need to be made to prevent the growth of solution extrema. The results from analysis of the interpolated flux from both a physicality and TVD perspective strongly point towards interpolated fluxes only being used if the data is monotone. At this point, since this is just a scalar result (and a scalar property), it is not clear which variables should be monotone in a system of equations, but is definitely worth considering in the future development and understanding of both new flux functions.

#### 4.4.1.1 TVD of the Interpolated Flux

It seems that the interpolated flux should also follow some sort of TVD property. Given the flux information, the interpolated flux should not produce extrema. One way to ensure this for the interpolated flux to be bounded by the neighboring fluxes,

$$0 \leq \frac{f_i^* - f_{i-1}}{f_{i+1} - f_{i-1}} \leq 1, \tag{4.41}$$

which reduces to

$$0 \leq \frac{u_i - u_{i-1}}{u_{i+1} - u_{i-1}} \leq 1, \tag{4.42}$$

again, a condition on the monotonicity of the data. This reassuring, but does not guarantee TVD of the conserved data itself.

### 4.4.2 Numerical Results

To quantitatively compare flux functions A and B, several numerical tests are used. In each case, a CFL number of 0.5 is used and no waves are permitted to reach the boundary, to avoid the effects of boundary conditions. First, two smooth expansion wave tests are done, a right going expansion wave, with $u_L = 0.1$ and $u_R = 0.9$ and

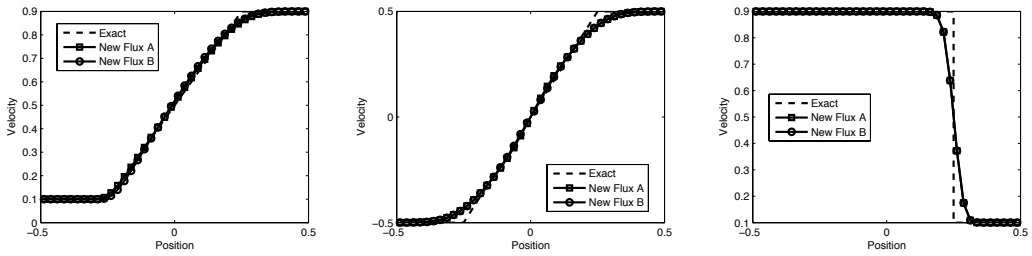


Figure 4.2: (left) Right going expansion wave for Burgers' Equation. (middle) Centered expansion wave. (right) Right moving shockwave.

a centered expansion wave with $u_L = -0.5$ and $u_R = 0.5$. Results in Figure 4.2 demonstrate the ability of each flux to simulate expansion waves. In both cases, flux function A and flux function B perform comparably and there is no obvious benefit to one or the other. Next, a single right moving shockwave with speed 0.5 and initial conditions $u_L = 0.1$ and $u_R = 0.9$ is simulated. In this case, again in Figure 4.2, both flux functions perform nearly identically. In each case, the initial data is monotone so the differences are small, but if the data was not monotone, flux function B would appear to be better, simply based on analysis. In practice, a lot of the differences can be removed through the choice of entropy-fix, so results for non-monotone cases are not shown. Nonetheless, Burgers' equation does provide several interesting analytic results and can be used in shaping the development future flux functions.

## 4.5 Euler Equations

From equation (4.4), the first two components of the interpolated flux for the Euler equations are

$$\begin{aligned} \mathbf{f}^*_{i,1} &= \rho_i u_i \\ \mathbf{f}^*_{i,2} &= \left(p_i + \rho_i u_i^2\right) + \frac{3-\gamma}{2}\left(\frac{\rho_{i-1}\rho_{i+1}(u_{i-1}-u_{i+1})^2}{(\sqrt{\rho_{i-1}}+\sqrt{\rho_{i+1}})^2} - \rho_i\left(\tilde{u}_i - u_i\right)^2\right) \end{aligned} \quad (4.43)$$

Examining these components, the interpolation process does not affect the mass flux. This is expected since the mass flux is simply the momentum, a conserved quantity. In effect, interpolation has done exactly as intended, leaving conserved quantities alone and making an adjustment to the pressure, which assumes local thermodynamic equilibrium.

### 4.5.1 Canonical Test Problems

To demonstrate the performance of both new flux functions, several canonical test problems are used. In each case, a CFL number of 0.5 is used along with a uniform grid. To enforce boundary conditions, ghost cells are added on the boundaries, with an additional ghost cell added to compute the interpolated flux. While there are other methods for enforcing boundary conditions with the new flux functions, it is not the focus of this work. As in Chapter III, $\gamma = 1.4$ is used unless otherwise specified.

#### 4.5.1.1 Sod's Problem

Sod's shocktube problem [87] is one of the most common test problems and a benchmark Riemann problem for almost all shock-capturing codes. The initial conditions are

$$\begin{bmatrix} \rho_L \\ u_L \\ p_L \end{bmatrix} = \begin{bmatrix} 1.0 \\ 0.0 \\ 1.0 \end{bmatrix}, \qquad \begin{bmatrix} \rho_R \\ u_R \\ p_R \end{bmatrix} = \begin{bmatrix} 0.125 \\ 0.0 \\ 0.1 \end{bmatrix}. \tag{4.44}$$

with the interface at $x = 0$. Results are shown in Figure 4.3 for flux functions A and B, with Roe's Riemann solver and the exact solution for comparison. All three flux functions show nearly indistinguishable results and perform as expected on this problem, since the shock is far from stationary.

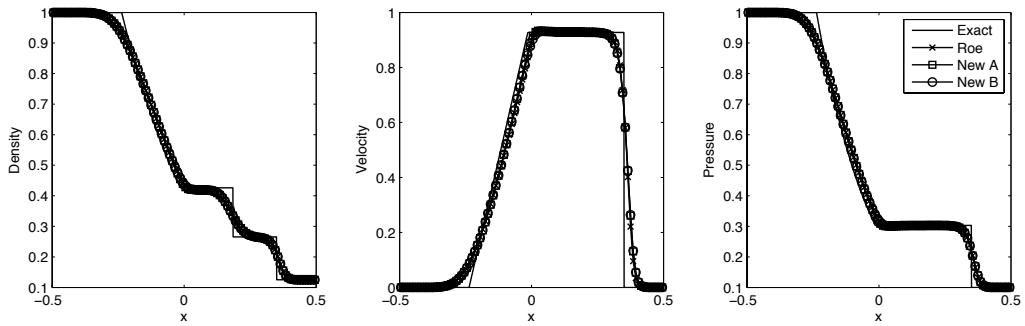


Figure 4.3: Numerical results for Sod's Shocktube Problem.

#### 4.5.1.2 Woodward and Colella Double Blast Wave

A notoriously tough test problem, the Woodward and Colella double blast wave [97] describes the interaction of two strong shocks. The domain is of unit length with walls on both ends and three regions with a constant density and velocity, $\rho = 1$ and $u = 0$ and pressure defined as

$$p = \begin{cases} 1000 & 0.0 \leq x \leq 0.1 \\ 0.01 & 0.1 < x < 0.9 \\ 100 & 0.9 \leq x \leq 1.0. \end{cases} \tag{4.45}$$

Results are shown in Figure 4.4 for a grid with 200 cells. With no analytic solution available, a fine grid solution on 1000 cells is shown for comparison. Again, both new flux functions perform comparably to Roe's Riemann solver and do an adequate job representing the flow solution.

#### 4.5.1.3 Shu-Osher Problem

The Shu-Osher problem [86] is a well known test problem where a Mach 3 shock-wave interacts with a wave in density designed to test how well numerical methods resolve small scale flow features in the presence of shocks. While generally used as a test for higher-order methods, it is still a good test for the new flux functions to

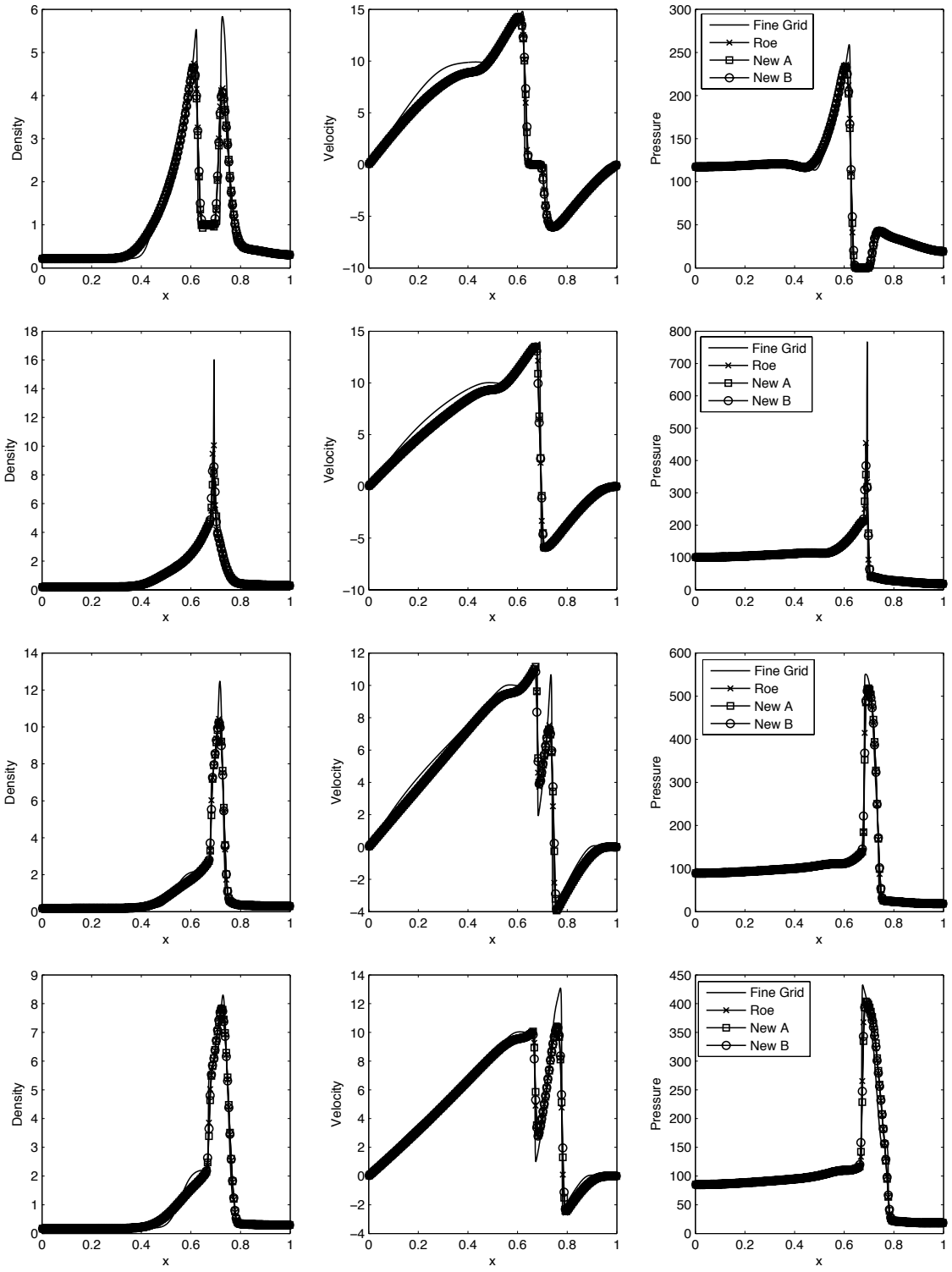


Figure 4.4: Numerical results for the Double Blast Wave problem at $t = 0.24, 0.28, 0.32, 0.34$ representing before, during, and after the two shocks have interacted.

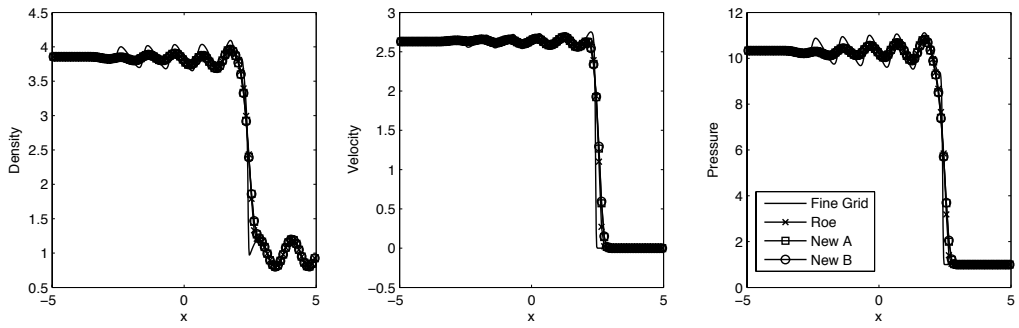


Figure 4.5: Numerical results for the Shu-Osher test problem at $t = 1.8$.

see how well they handle interacting shocks and contact discontinuities. A domain of $-5 \leq x \leq 5$ is used with left and right states separated at $x = -4$ and initial conditions

$$\begin{bmatrix} \rho_L \\ u_L \\ p_L \end{bmatrix} = \begin{bmatrix} 3.857143 \\ 2.629369 \\ 10.33333 \end{bmatrix}, \qquad \begin{bmatrix} \rho_R \\ u_R \\ p_R \end{bmatrix} = \begin{bmatrix} 1.0 + 0.2\sin(5x) \\ 0.0 \\ 1.0 \end{bmatrix}. \tag{4.46}$$

and $\gamma = 1.4$. One hundred cells are used and a fine grid solution of five hundred cells is used for comparison. Again, both new flux functions perform comparably to Roe's Riemann solver, as shown in Figure 4.5. The results in this problem and the previous two problems are not all that surprising given the similarity of the new fluxes to Roe's Riemann solver in most circumstances. Of utmost importance is that interpolating the fluxes does not broaden the shocks or result in smoothing of other flow features.

### 4.5.2 Numerical Shockwave Anomalies

Since both new fluxes perform reasonably well on standard test problems, they are tested on the anomalies described in Chapter III. By construction, both fluxes compute a stationary shock with no positional ambiguity, so the stationary shock is not examined.

#### 4.5.2.1 The Slowly Moving Shock Phenomenon

To determine how well they maintain the unambiguous shock structure as the shockwave moves, the slowly moving shock phenomenon is examined. Rather than construct it by perturbing the stationary case, the exact solution for a shock of speed $S$ is used with the left state from (3.2) and the right state as

$$\begin{bmatrix} \rho_R \\ u_R \\ p_R \end{bmatrix} = \begin{bmatrix} \frac{S-1}{S-\frac{2(S-1)}{\gamma+1}+\frac{2}{M_L^2(\gamma+1)(S-1)}-1} \\ \frac{2(S-1)}{\gamma+1} - \frac{2}{M_L^2(\gamma+1)(S-1)} + 1 \\ \frac{2(S-1)^2}{\gamma+1} - \left(\frac{2}{\gamma+1} - \frac{1}{\gamma}\right)\frac{1}{M_L^2} \end{bmatrix}. \tag{4.47}$$

with the problem initialized as a Riemann Problem. Results are shown for the Mach 10 shockwave for three different shock speeds.

Looking at the results in Figure 4.6 for the slowest shock speed, both new fluxes greatly reduce the momentum spike in the slowly moving shock. Flux function A appears to completely remove it, while flux function B leaves a very small spike behind. Of utmost importance is that the new flux functions have not smeared out the shockwave - there is still only one intermediate state at any particular time. The state space plots demonstrate the linearly placed intermediate shock states. It is clear that the ambiguity in shock position has been dramatically reduced. This is expected, since in this case, the shock is very close to stationary.

For a slightly faster shock, in Figure 4.7, both fluxes again significantly reduce the momentum spike and perform well, although the difference between flux function A and flux function B is clearer. For this problem, flux function A maintains a much more linear shock profile than flux function B. For an even faster shock in Figure 4.8, the momentum spike with Roe's flux is smaller and the anomalous behavior is less pronounced. In each momentum plot, there is also evidence of a small start-up error. Again, the new fluxes suffer less from this effect as well. As the shock speed

is increased and more intermediate states are needed in the shock, the new fluxes are less able to preserve the one point shock and as seen in state space, deviate more from the linear profile.

Combining all these results and looking specifically at the momentum, where the largest error is observed, leads to Figure 4.9. In this figure, the error is defined as

$$\text{Relative Maximum Momentum Error } = \frac{\max_{x,t}(\rho u) - \rho_R u_R}{\rho_R u_R} \times 100, \tag{4.48}$$

which is a measure of the momentum overshoot. Flux function A reduces the error the most, outperforming flux function B on this problem for all Mach numbers.

#### 4.5.2.2 Wall Heating

With the strong performance on the slowly moving shock phenomenon, the new fluxes are tested on the Noh Problem. The same conditions from Section 3.2 are used with a CFL number of 0.5. While there is some dependency on CFL number, the trends displayed and overall performance remains the same. Comparing the new fluxes to Roe's Riemann solver in Figure 4.10, all three methods compute velocity and pressure equivalently. Looking at the density defect at the wall, flux function A dramatically outperforms flux function B, especially for the Mach 10 shock, likely due to the flux function A's Looking at the relative wall density error, defined as

$$\text{Relative Wall Density Error } = \frac{\rho_{wall} - \rho_{exact}}{\rho_{exact}} \times 100 \tag{4.49}$$

in Figure 4.11 shows that for all Mach numbers, flux function A reduces the error significantly while flux function B performs comparably to Roe's Riemann solver, reducing the density defect slightly in comparison. Thus reducing the ambiguity in shock position can reduce the density defect at the wall. The improvement is greatest at higher Mach numbers, when the shock speed is slowest.

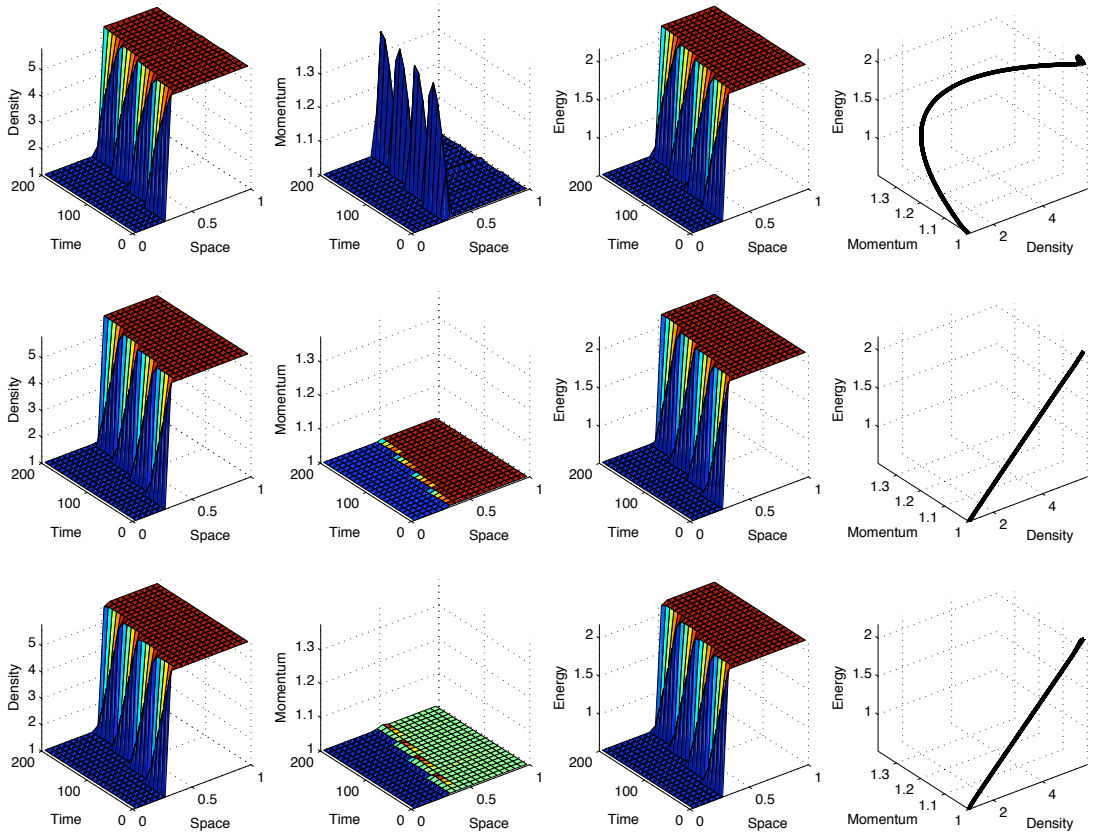


Figure 4.6: Results for the slowly moving shock problem with $S = 0.0001$. (top) Roe's Riemann Solver. (middle) Flux function A. (bottom) Flux function B. For each flux, density, momentum, and energy are shown as a function of space and time. On the right, the results are plotted in conserved state space.

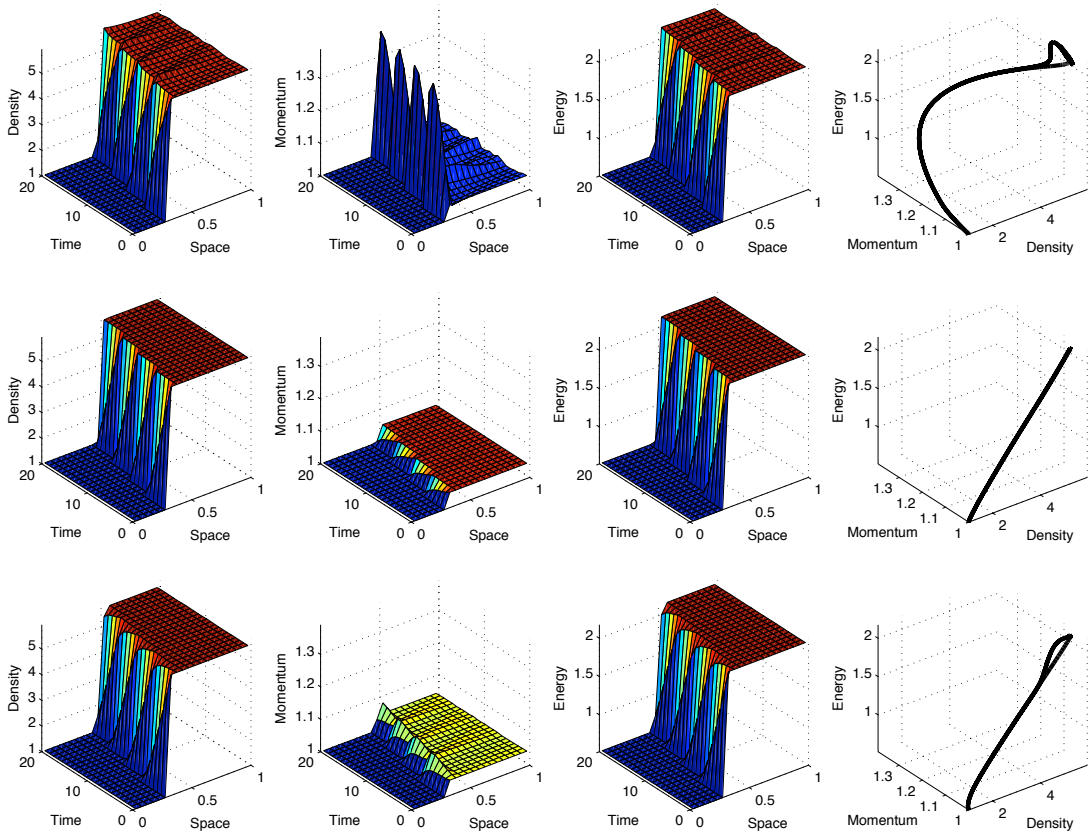


Figure 4.7: Results for the slowly moving shock problem with $S = 0.001$. Same plots as Figure 4.6.

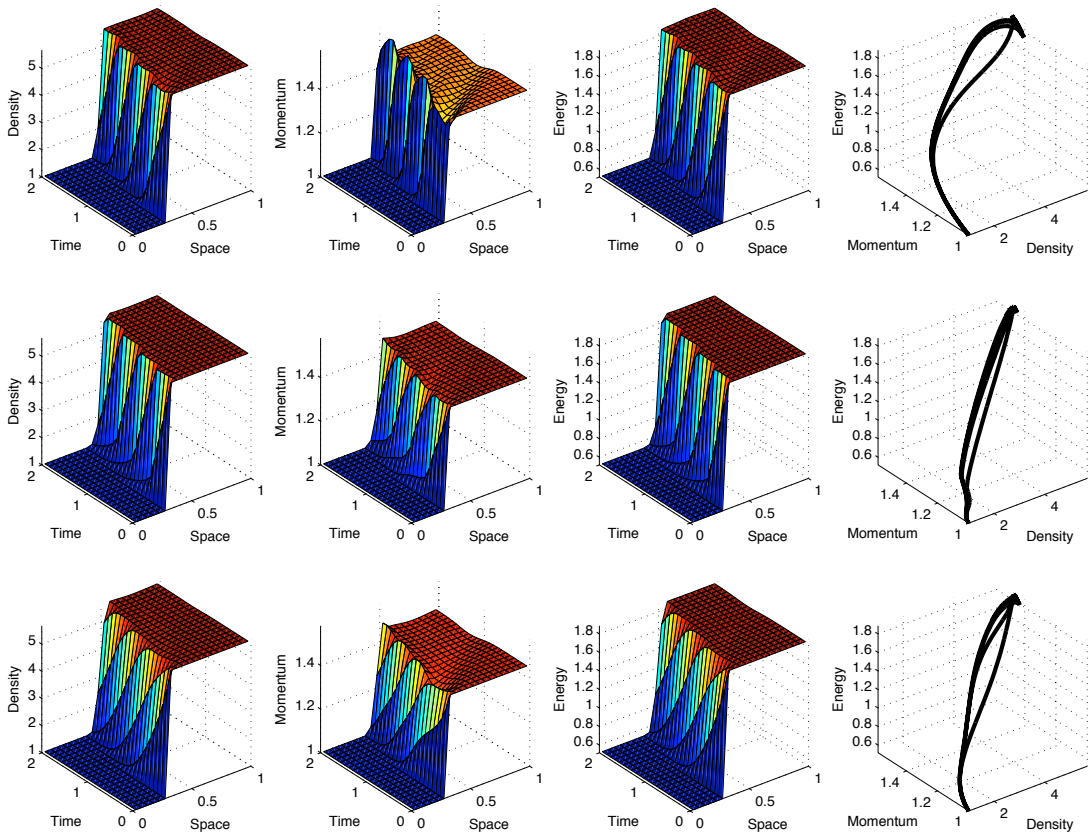


Figure 4.8: Results for the slowly moving shock problem with $S = 0.1$. Same plots as Figure 4.6.

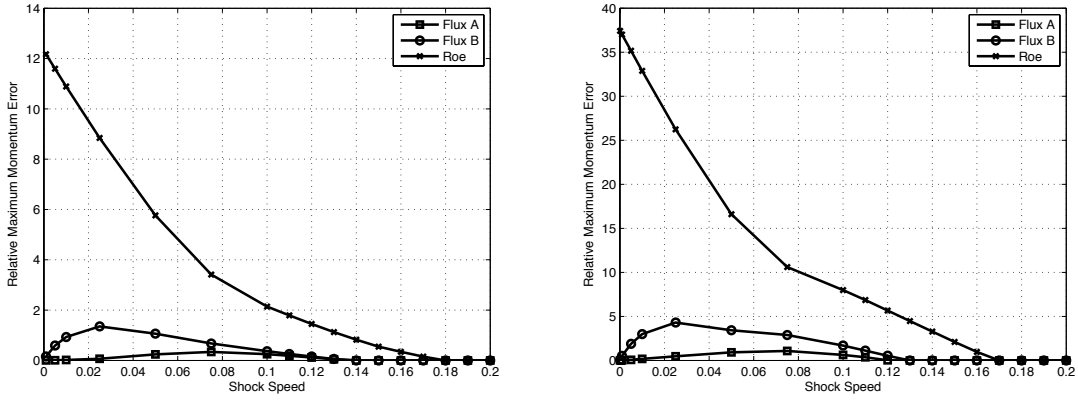


Figure 4.9: Relative Maximum Momentum Error vs Shock Speed for Roe's Riemann Solver ($\times$), flux function A ($\square$), and flux function B ($\circ$) for Mach 2.0 (left) and Mach 10.0 (right). Both new flux functions reduce the momentum spike significantly for all shock speeds.

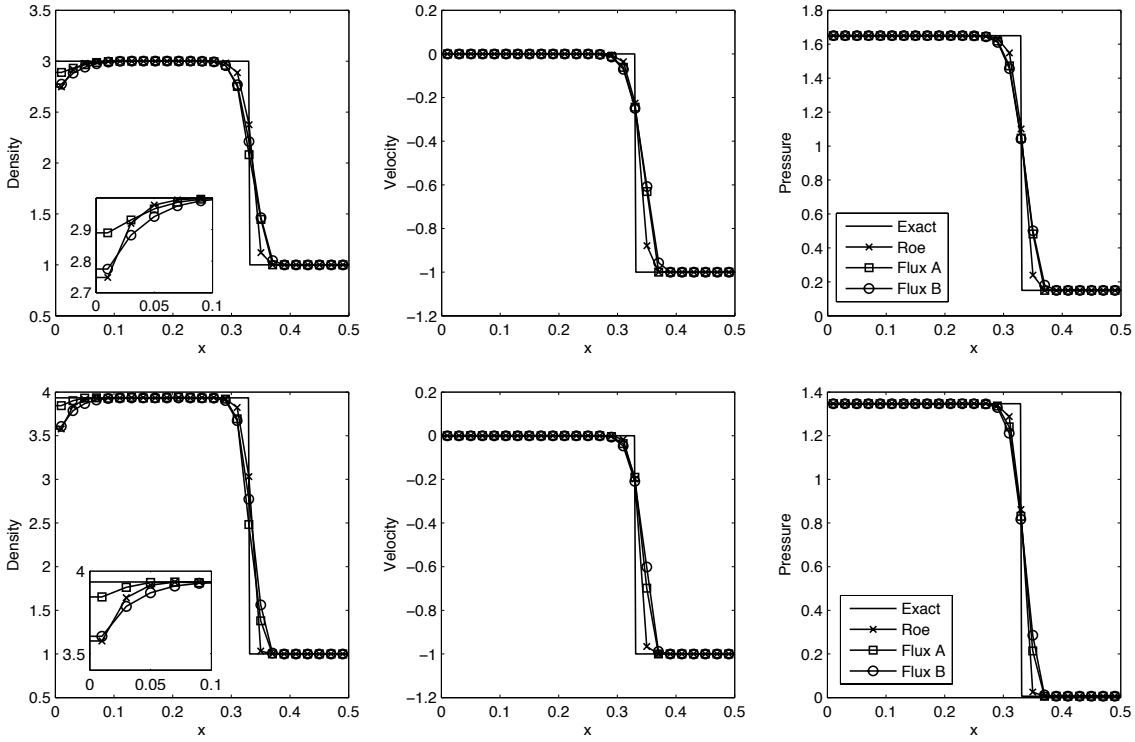


Figure 4.10: Density, velocity and pressure results for the Noh problem with initial Mach number of 2 (top) and Mach number of 10 (bottom).

#### 4.5.2.3 One-dimensional Carbuncle

Numerically, neither flux function A or flux function B show any sign of the carbuncle after extensive testing. To further confirm that all intermediate states are stable and the fluxes are carbuncle-free, the work of Barth is followed [2]. Starting with a one-point stationary shock, the residual function corresponding to the net flux through the intermediate state is

$$\mathbf{r}(\mathbf{u}_M; \mathbf{u}_L, \mathbf{u}_R) = \mathbf{f}_{MR} - \mathbf{f}_{LM} \tag{4.50}$$

for the shock with left and right endpoints $\mathbf{u}_L$ and $\mathbf{u}_R$. This function has a zero eigenvalue and a singular Jacobian matrix, $\det\left[\frac{\partial \mathbf{r}}{\partial \mathbf{u}_M}\right] = 0$, since all middle states $\mathbf{u}_M$ are stationary points. To determine the sensitivity to the zero eigenvalue, examine

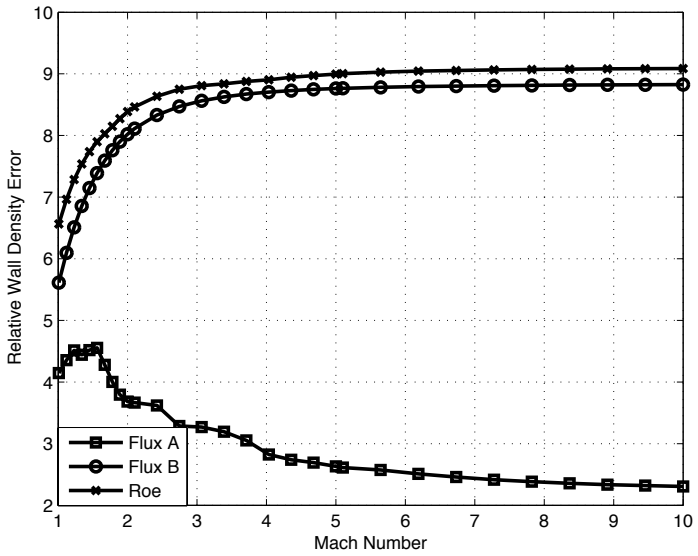


Figure 4.11: Relative Wall Density Error vs Mach number for Roe's Riemann Solver ($\times$), flux function A ($\square$), and flux function B ($\circ$).

the semi-discrete equations on a grid with unit spacing,

$$\frac{\partial \mathbf{u}_M}{\partial t} + \mathbf{r}(\mathbf{u}_M; \mathbf{u}_L, \mathbf{u}_R) = \mathbf{0}. \tag{4.51}$$

Near a stationary solution, $\mathbf{u}^*$, the residual, $\mathbf{r}(\mathbf{u}^*; \mathbf{u}_L, \mathbf{u}_R)$, is zero and the residual can be linearized with $\mathbf{u}_M = \delta\mathbf{u} + \mathbf{u}^*$ as

$$\mathbf{r}(\mathbf{u}_M) = \mathbf{r}(\mathbf{u}^* + \delta\mathbf{u}) = \mathbf{r}(\mathbf{u}^*) + \frac{\partial \mathbf{r}(\mathbf{u}^*)}{\partial \mathbf{u}_M}\delta\mathbf{u} \tag{4.52}$$

such that $\delta\mathbf{u}$ is governed by

$$\frac{\partial(\delta\mathbf{u})}{\partial t} + \frac{\partial \mathbf{r}(\mathbf{u}^*)}{\partial \mathbf{u}_M}\delta\mathbf{u} = 0 \tag{4.53}$$

and the solution can be determined from the eigenvalues, $\lambda_i$, and eigenvectors, $\mathbf{r}_i$, of the residual Jacobian,

$$\delta\mathbf{u}(t) = \alpha_1\mathbf{r}_1 + \alpha_2\mathbf{r}_2 e^{-\lambda_2 t} + \alpha_3\mathbf{r}_3 e^{-\lambda_3 t} \tag{4.54}$$

where $\lambda_1$ corresponds to the stationary eigenvalue and is zero. Stability and carbuncle free requires $\lambda_2, \lambda_3 \geq 0$ to ensure the stability of $\mathbf{u}_M$. To avoid boundary effects, the eigenvalues of $\frac{\partial \mathbf{r}}{\partial \mathbf{u}}$ are examined for a stationary shock problem using several extra cells. For this analysis, the initial middle state is created on the nonphysical branch of the Hugoniot for Roe's Riemann solver and on a straight line in state space for the new flux functions. The results are shown in Figure 4.12 for Roe's flux function and both new flux functions. At Mach 10 and 20, negative eigenvalues are seen only for the Roe flux. From this analysis, both new flux functions are carbuncle-free in one dimension.

## 4.6 Summary

In this chapter, two new flux functions were developed that have an unambiguous sub-cell shock position. On all of the shock anomalies in one-dimension, both fluxes show improvement on existing methods without smearing or diffusing the shock. On a range of other canonical problems, there is no major detriment to using the flux functions outside of shockwaves since they reduce to a second-order correction to Roe's Riemann solver and the differences are not observed in the first-order framework.

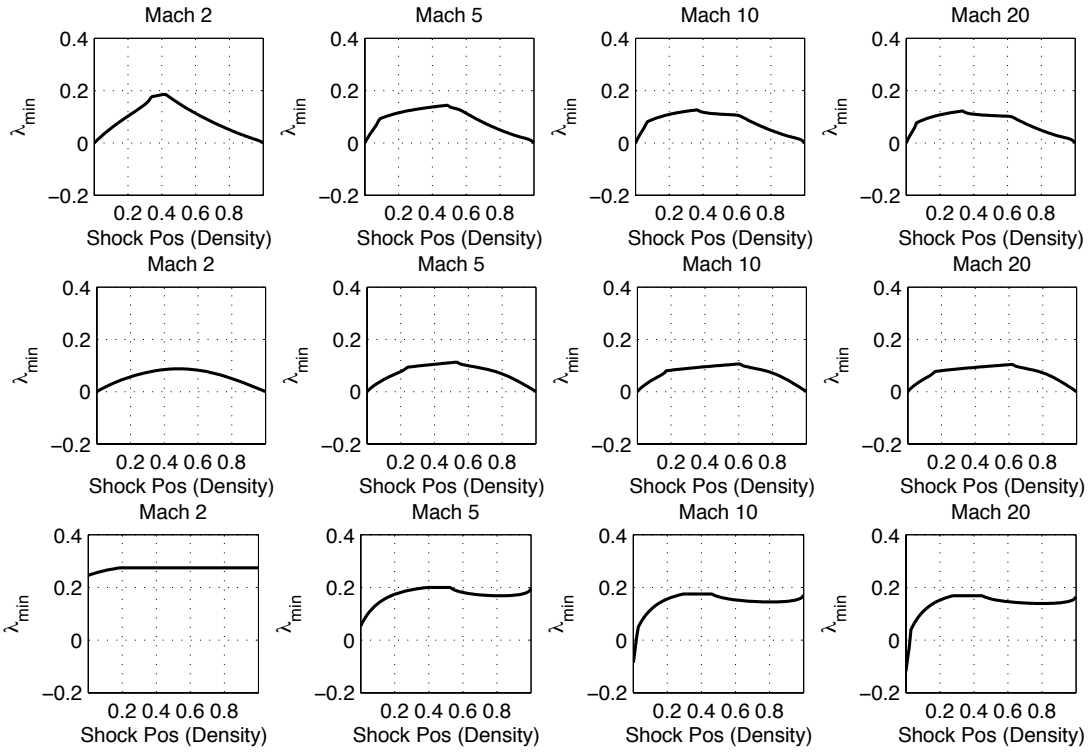


Figure 4.12: Stability Results for the one-dimensional carbuncle for flux function A (top), flux function B (middle), Roe's Flux (bottom) for 4 different Mach numbers. Only Roe's Flux has negative (unstable) eigenvalues.

# CHAPTER V

# Extensions

Both new flux functions show significant reduction of shockwave anomalies in one-dimension. For these methods to be practical, they need to be extended past first-order accuracy and to multi-dimensional problems. In this chapter, both of these extensions are developed. Although around strong shocks, higher-order methods reduce to first-order, the new fluxes should still fit within their framework and perform accurately in smooth regions. While there are many more complex methods for these extensions than the ones used, they serve as simply a verification of the capabilities and potential of the new flux functions.

## 5.1 Second-Order Accuracy

To extend the new flux functions to second-order accuracy, a MUSCL-type reconstruction is used [94]. In the one-dimensional case, in each cell, a linear reconstruction of both conserved variables and fluxes can be defined

$$\mathbf{u}_i(x) = \mathbf{u}_i + \mathbf{u}_{x,i}(x - x_i) \tag{5.1}$$

$$\mathbf{f}_i^*(x) = \mathbf{f}_i^* + \mathbf{f}_{x,i}^*(x - x_i) \tag{5.2}$$

by defining gradient functions $\mathbf{u}_{x,i}, \mathbf{f}^*_{x,i}$ of the left and right gradients,

$$\mathbf{u}_{x,i} = \mathbf{u}_{x,i}\left(\frac{\mathbf{u}_i - \mathbf{u}_{i-1}}{x_i - x_{i-1}}, \frac{\mathbf{u}_{i+1} - \mathbf{u}_i}{x_{i+1} - x_i}\right) \tag{5.3}$$

$$\mathbf{f}^*_{x,i} = \mathbf{f}^*_{x,i}\left(\frac{\mathbf{f}^*_i - \mathbf{f}^*_{i-1}}{x_i - x_{i-1}}, \frac{\mathbf{f}^*_{i+1} - \mathbf{f}^*_i}{x_{i+1} - x_i}\right). \tag{5.4}$$

To prevent oscillations produced by the reconstruction, limiters are required. A well known problem with second-order and higher schemes [23], these oscillations are different than those produced in the first-order scheme, but nonetheless problematic. To ensure that temporal errors do not reduce spatial accuracy, a second order Runge-Kutta method is used [24]

$$\mathbf{u}_i^{n+\frac{1}{2}} = \mathbf{u}_i^n + \frac{\Delta t}{\Delta x}(\mathbf{f}^n_{i+\frac{1}{2}} - \mathbf{f}^n_{i-\frac{1}{2}}). \tag{5.5}$$

$$\mathbf{u}_i^{n+1} = \frac{1}{2}(\mathbf{u}_i^n + \mathbf{u}_i^{n+\frac{1}{2}}) + \frac{\Delta t}{2\Delta x}(\mathbf{f}^{n+\frac{1}{2}}_{i+\frac{1}{2}} - \mathbf{f}^{n+\frac{1}{2}}_{i-\frac{1}{2}}). \tag{5.6}$$

If a Riemann solver is used, the interface fluxes are computed using reconstructed data at the edges, with

$$\mathbf{f}_{i+\frac{1}{2}} = \mathbf{f}(\mathbf{u}_i^+, \mathbf{u}_{i+1}^-) \tag{5.7}$$

where $\mathbf{u}_i^+$ and $\mathbf{u}_{i+1}^-$ are the edge values of the conserved variables defined as

$$\mathbf{u}_i^+ = \mathbf{u}_i + \frac{\Delta x}{2}\mathbf{u}_{x,i}, \qquad \mathbf{u}_{i+1}^- = \mathbf{u}_{i+1} - \frac{\Delta x}{2}\mathbf{u}_{x,i+1}. \tag{5.8}$$

Using a similar notation for edge values of the interpolated fluxes

$$\mathbf{f}_i^{*,+} = \mathbf{f}_i^* + \frac{\Delta x}{2}\mathbf{f}^*_{x,i}, \qquad \mathbf{f}_{i+1}^{*,-} = \mathbf{f}^*_{i+1} - \frac{\Delta x}{2}\mathbf{f}^*_{x,i+1} \tag{5.9}$$

there are several ways to utilize the reconstructions within the new flux functions. Flux function A can be computed using only interpolated flux reconstructions (re-

ferred to as A-U1F2) as

$$\mathbf{f}^A_{i+\frac{1}{2}} = \frac{1}{2}(\mathbf{f}^{*,+}_i + \mathbf{f}^{*,-}_{i+1}) - \frac{1}{2}\text{sign}(\tilde{\mathbf{A}}(\mathbf{u}_i, \mathbf{u}_{i+1}))(\mathbf{f}^{*,-}_{i+1} - \mathbf{f}^{*,+}_i) \qquad \text{A-U1F2} \qquad (5.10)$$

or reconstructing both interpolated fluxes and conserved variables as

$$\mathbf{f}^A_{i+\frac{1}{2}} = \frac{1}{2}(\mathbf{f}^{*,+}_i + \mathbf{f}^{*,-}_{i+1}) - \frac{1}{2}\text{sign}(\tilde{\mathbf{A}}(\mathbf{u}^+_i, \mathbf{u}^-_{i+1}))(\mathbf{f}^{*,-}_{i+1} - \mathbf{f}^{*,+}_i) \qquad \text{A-U2F2.} \qquad (5.11)$$

For flux function B, there is more flexibility on how the reconstructions should be used. Three particular variations of B are tested in this thesis: reconstructing only interpolated fluxes, reconstructing only conserved variables, and reconstructing both. They are expressed as follows.

$$\mathbf{f}^B_{i+\frac{1}{2}} = \frac{1}{2}(\mathbf{f}^{*,+}_i + \mathbf{f}^{*,-}_{i+1}) - \frac{1}{2}\left|\tilde{\mathbf{A}}(\mathbf{u}_{i-1}, \mathbf{u}_{i+2})\right|(\mathbf{u}_{i+1} - \mathbf{u}_i) \qquad \text{B-U1F2} \qquad (5.12)$$

$$\mathbf{f}^B_{i+\frac{1}{2}} = \frac{1}{2}(\mathbf{f}^{*}_i + \mathbf{f}^{*}_{i+1}) - \frac{1}{2}\left|\tilde{\mathbf{A}}(\mathbf{u}_{i-1}, \mathbf{u}_{i+2})\right|(\mathbf{u}^-_{i+1} - \mathbf{u}^+_i) \qquad \text{B-U2F1} \qquad (5.13)$$

$$\mathbf{f}^B_{i+\frac{1}{2}} = \frac{1}{2}(\mathbf{f}^{*,+}_i + \mathbf{f}^{*,-}_{i+1}) - \frac{1}{2}\left|\tilde{\mathbf{A}}(\mathbf{u}_{i-1}, \mathbf{u}_{i+2})\right|(\mathbf{u}^-_{i+1} - \mathbf{u}^+_i) \qquad \text{B-U2F2} \qquad (5.14)$$

For flux function B, the Roe-averaged flux Jacobian was kept as only a function of the cell-averaged data, since it is not computed locally.

## 5.2 Two Dimensions

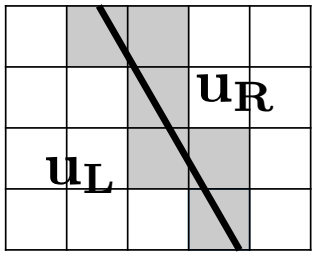


Figure 5.1: Oblique shock in two dimensions. Intermediate states shown in gray.

The addition of a second spatial dimension does not change the underlying philosophy. In one dimension, the straight line in conserved state space contains the projections of the exact solution onto cell-averaged space. In two dimensions, the same statement is true; cell-averages of the exact solution in each intermediate state are on this line. Numerically, there are still intermediate shock states which contain data that should not be trusted (Figure 5.1) and ideally these should be forced on to the straight line connecting end states. In the stationary case, each intermediate shock state is adjacent to at least two end states of the shock, although not necessarily aligned in the $x$ or $y$ direction. Thus the interpolated flux in the $x$-direction should lie on a straight line in flux space with the interpolated flux in the $y$-direction. This requires a genuinely two-dimensional method, using interpolated fluxes computed from information in both directions, which at this point is left for future work.

Nevertheless, with the strong performance in one dimension, a simple extension of the one-dimensional method is a natural first step. Given a system of hyperbolic conservation laws in two dimensions in conservation form

$$\mathbf{u}_t \quad + \quad \mathbf{f}(\mathbf{u})_x + \mathbf{g}(\mathbf{u})_y = \mathbf{0}, \tag{5.15}$$

or quasi-linear form

$$\mathbf{u}_t \quad + \quad \mathbf{A}(\mathbf{u})\mathbf{u}_x + \mathbf{B}(\mathbf{u})\mathbf{u}_y = \mathbf{0}, \tag{5.16}$$

with flux Jacobians $\mathbf{A} = \frac{\partial \mathbf{f}}{\partial \mathbf{u}}, \mathbf{B} = \frac{\partial \mathbf{g}}{\partial \mathbf{u}}$, the first-order finite volume method in one dimension can be extended to two dimensions using the update equations

$$\frac{\mathbf{u}_{i,j}^{n+1} - \mathbf{u}_{i,j}^{n}}{\Delta t} + \frac{\mathbf{f}_{i+\frac{1}{2},j}^{n} - \mathbf{f}_{i-\frac{1}{2},j}^{n}}{\Delta x_{i,j}} + \frac{\mathbf{g}_{,j+\frac{1}{2}}^{n} - \mathbf{g}_{i,j-\frac{1}{2}}^{n}}{\Delta y_{i,j}} = \mathbf{0}. \tag{5.17}$$

with each flux being treated in its respective direction. In each cell, there is now a

pair of interpolated fluxes,

$$\mathbf{f}^*_{i,j} = \frac{1}{2}(\mathbf{f}_{i-1,j} + \mathbf{f}_{i+1,j}) - \frac{1}{2}\tilde{\mathbf{A}}_{i-1,i+1,j}(\mathbf{u}_{i+1,j} - 2\mathbf{u}_{i,j} + \mathbf{u}_{i-1,j}) \tag{5.18}$$

$$\mathbf{g}^*_{i,j} = \frac{1}{2}(\mathbf{g}_{i,j-1} + \mathbf{g}_{i,j+1}) - \frac{1}{2}\tilde{\mathbf{B}}_{i,j-1,j+1}(\mathbf{u}_{i,j+1} - 2\mathbf{u}_{i,j} + \mathbf{u}_{i,j-1}). \tag{5.19}$$

Both flux functions A and B follow from Equations (4.12) and (4.19). To ensure stability, a CFL condition similar to Equation (2.25) is used, with

$$CFL = \max_i |\lambda_{i,x}| \frac{\Delta t}{\Delta x} + \max_i |\lambda_{i,y}| \frac{\Delta t}{\Delta y} \leq 1. \tag{5.20}$$

For all the second-order methods described, the extension to two-dimensions follows, with a gradient in both $x$ and $y$ direction constructed and limited independently.

### 5.2.1 Euler Equations

Only experiments on the Euler equations are performed with either extension. In two dimensions, the Euler equations are

$$\frac{\partial}{\partial t}\begin{bmatrix} \rho \\ \rho u \\ \rho v \\ E \end{bmatrix} + \frac{\partial}{\partial x}\begin{bmatrix} \rho u \\ \rho u^2 + p \\ \rho uv \\ \rho uH \end{bmatrix} + \frac{\partial}{\partial y}\begin{bmatrix} \rho v \\ \rho uv \\ \rho v^2 + p \\ \rho vH \end{bmatrix} = \mathbf{0} \tag{5.21}$$

with equation of state $p = (\gamma - 1)\left(E - \frac{1}{2}\rho(u^2 + v^2)\right)$. The flux Jacobians and Roe's Riemann solver are similar to that in one-dimension and can be found in [91].

## 5.3 Second-Order Accuracy Results

### 5.3.1 Simple Waves

To verify the accuracy of the second-order extension, several simple wave tests are done. The first is a simple travelling density wave with solution

$$\rho = \rho_\infty + A\sin[\pi(x + y - (u_\infty + v_\infty)t)] \tag{5.22}$$

$$u = u_\infty \tag{5.23}$$

$$v = v_\infty \tag{5.24}$$

$$p = p_\infty \tag{5.25}$$

on a periodic domain of $0 \leq x, y \leq 2$. Both a two-dimensional version and a one-dimensional version, obtained by setting $y = 0$ and $v_\infty = 0$, are examined. In the two examples shown, $A = 0.5$, $\rho_\infty = p_\infty = 1$ and the velocities are $u_\infty = 0.5, v_\infty = 1$. A CFL number of 0.5 is used the error is measured at a time of $t = 4.0$, corresponding to one complete period in $x$. The spatial error is computed from the exact solution using the L-2 norm of density. The results in Figure 5.2 demonstrate that second-order accuracy is achieved for both new flux functions in both one and two dimensions. For flux function A, second-order accuracy is achieved provided the interpolated fluxes are reconstructed, regardless of how the conserved variables are treated. For flux function B, second-order accuracy is achieved with only the reconstruction of the conserved variables, though reconstructing interpolated fluxes does reduce the error by about 50%. This result, while somewhat surprising, is actually true of Roe's Riemann solver as well, where if the fluxes are computed using cell-centered conserved variables, second-order accuracy can still be achieved.

Next, two one-dimensional simple acoustic waves described by Lowrie [56] with

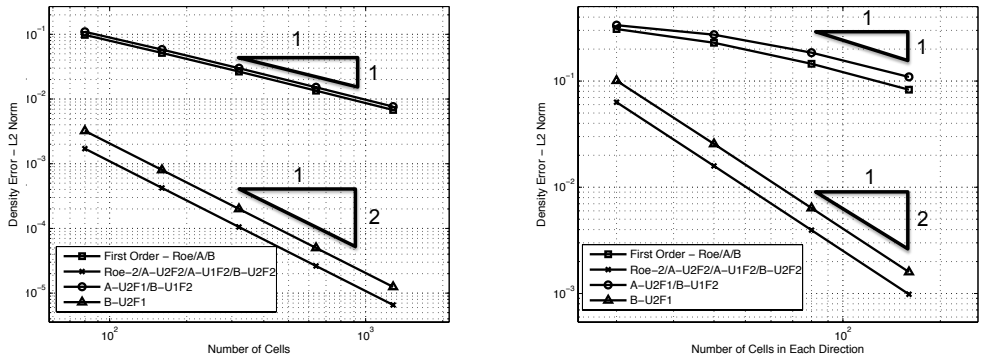


Figure 5.2: Error Convergence for the 1D (left) and 2D (right) moving density wave. First-order convergence is obtained using the original first-order method and with reconstructions of only conserved variables for A (U2F1) or interpolated fluxes for B (U1F2). Second-order accuracy is obtained for both new flux functions using the other choices of reconstructed variables (A-U2F2, A-U1F2, B-U2F2, B-U2F1).

initial conditions

$$\frac{u(x)}{a_\infty} = M_\infty + \frac{2}{\gamma+1}\frac{V(x)}{a_\infty} \tag{5.26}$$

$$\frac{\rho(x)}{\rho_\infty} = \left[1 + \frac{\gamma-1}{2}\left(\frac{u(x)}{a_\infty} - M_\infty\right)\right]^{\frac{2}{\gamma-1}} \tag{5.27}$$

$$\frac{p(x)}{p_\infty} = \left[1 + \frac{\gamma-1}{2}\left(\frac{u(x)}{a_\infty} - M_\infty\right)\right]^{\frac{2\gamma}{\gamma-1}} \tag{5.28}$$

are used, where $V = u + a$, and $V$ is a solution to Burgers' equation. First, a smooth solution sharpening into a shockwave, with initial condition

$$V(x) = \frac{1}{2\pi t_s}\cos(2\pi x) \tag{5.29}$$

is examined, where $t_s$ corresponds to the time of shock formation. The reference quantities are $M_\infty = a_\infty = \rho_\infty = p_\infty = 1.0$ and shock formation time is 2.0. For accuracy, a smooth solution is required, so the spatial error is measured prior to the shock formation, at $t = 1.0$, when the solution is still relatively smooth. Again, a CFL number of 0.5 is used in each case and the L-2 norm of density error is

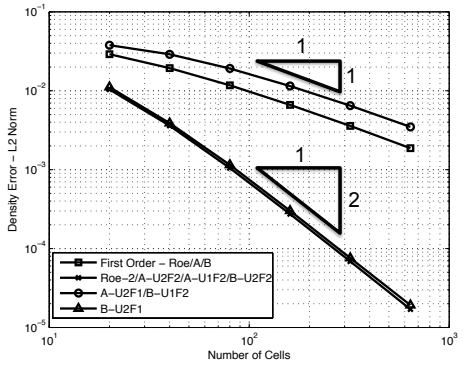


Figure 5.3: Error convergence for the simple compression wave.

measured. Results in Figure 5.3 demonstrate second-order accuracy similar to that for the traveling density wave.

Since second-order accuracy is achieved for the compression wave, a smooth expansion wave is examined, with initial condition

$$V(x) = 0.04 \tanh(10(x - 0.5)). \tag{5.30}$$

The reference Mach number, $M_\infty$, is set to -1.0 to keep the expansion wave centered inside the domain. A CFL number of 0.5 is used and a similar set of results to the previous tests are generated. In Figure 5.4, first-order and second-order results are presented. Unlike the simple compression wave, there are differences between the reconstruction choices in the new flux functions. While the same orders of accuracy as before are achieved, there is some difference in the magnitude of the error.

### 5.3.2 Isentropic Vortex

With the new flux functions achieving second-order accuracy for simple waves, a slightly more complex problem is examined: an isentropic vortex. First described in

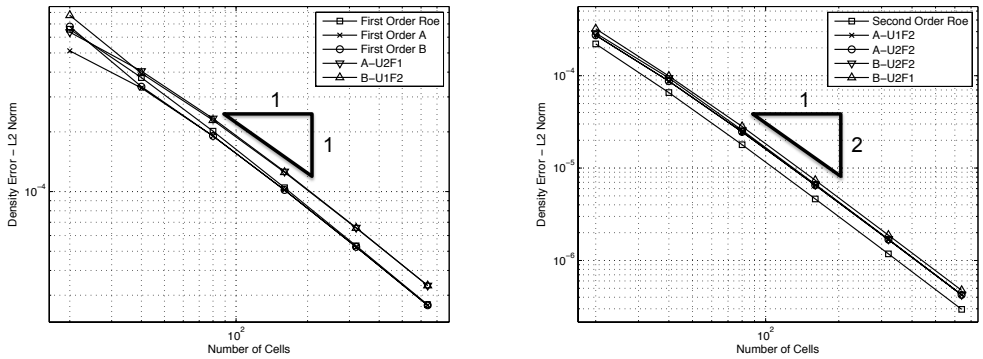


Figure 5.4: Error convergence for the simple expansion. First order results (left) and second order results (right).

1998 [29], its solution is defined by the following expressions

$$\frac{u(x,y,t)}{a_\infty} = \frac{u_\infty}{a_\infty} - \frac{K}{2\pi a_\infty}\bar{y}e^{\alpha(1-\bar{r}^2)/2} \tag{5.31}$$

$$\frac{v(x,y,t)}{a_\infty} = \frac{v_\infty}{a_\infty} + \frac{K}{2\pi a_\infty}\bar{x}e^{\alpha(1-\bar{r}^2)/2} \tag{5.32}$$

$$\frac{\rho(x,y,t)}{\rho_\infty} = \left(1 - \frac{K^2(\gamma-1)}{8\alpha\pi^2 a_\infty}e^{\alpha(1-\bar{r}^2)}\right)^{\frac{1}{\gamma-1}} \tag{5.33}$$

$$\frac{p(x,y,t)}{p_\infty} = \left(1 - \frac{K^2(\gamma-1)}{8\alpha\pi^2 a_\infty}e^{\alpha(1-\bar{r}^2)}\right)^{\frac{\gamma}{\gamma-1}} \tag{5.34}$$

where the coordinates are defined relative to the vortex center as

$$\bar{x} = x - x_0 - u_\infty t \tag{5.35}$$

$$\bar{y} = y - y_0 - v_\infty t \tag{5.36}$$

$$\bar{r} = \sqrt{\bar{x}^2 + \bar{y}^2}. \tag{5.37}$$

For these results, a domain of $0 \leq x, y, \leq 10$ with periodic boundary conditions is used and the parameters chosen as $\alpha = 1, \rho_\infty = 1, p_\infty = 1/\gamma, u_\infty = v_\infty = 2, (x_0, y_0) = (5, 5)$ and $K = 5$. After one period, the spatial error is analysed. Results in Figure 5.5 again demonstrate second-order accuracy.

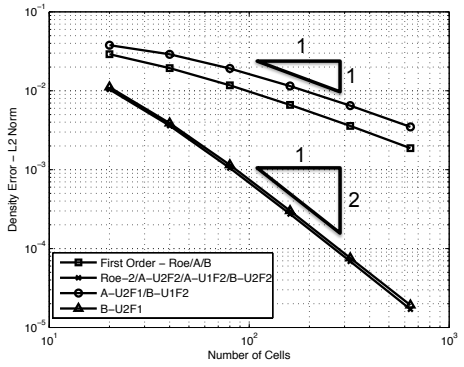


Figure 5.5: Error convergence for the isentropic vortex.

### 5.3.3 Summary

In this section, both new flux functions were tested on a range of smooth problems using a MUSCL-type extension to obtain second-order accuracy. In all problems, improved accuracy was achieved in several ways through reconstruction of conserved variables and/or interpolated fluxes. This was expected since for smooth problems, the interpolated flux is merely a second-order correction to the exact flux, such that the effect of both new flux functions is minimal.

## 5.4 Results for Two-dimensional Shocks.

### 5.4.1 Rotated Slowly Moving Shock Problem

The rotated slowly moving shock problem consists of the one-dimensional shock-wave defined in Equations (3.2) and (4.47) on a two-dimensional grid at an angle $\alpha$ to the grid. This problem is designed to determine the effectiveness of the new flux functions on slowly moving shocks that are not aligned with the grid. The grid is uniform with $0 \leq x \leq 2$ and $0 \leq y \leq 1$ such that the inflow and outflow boundaries are sufficiently far from the shock to minimize their effects. To allow for the boundary conditions to be easily implemented, shock angles are chosen such that the shock directly connects two grid points exactly. This ensures that every edge is either

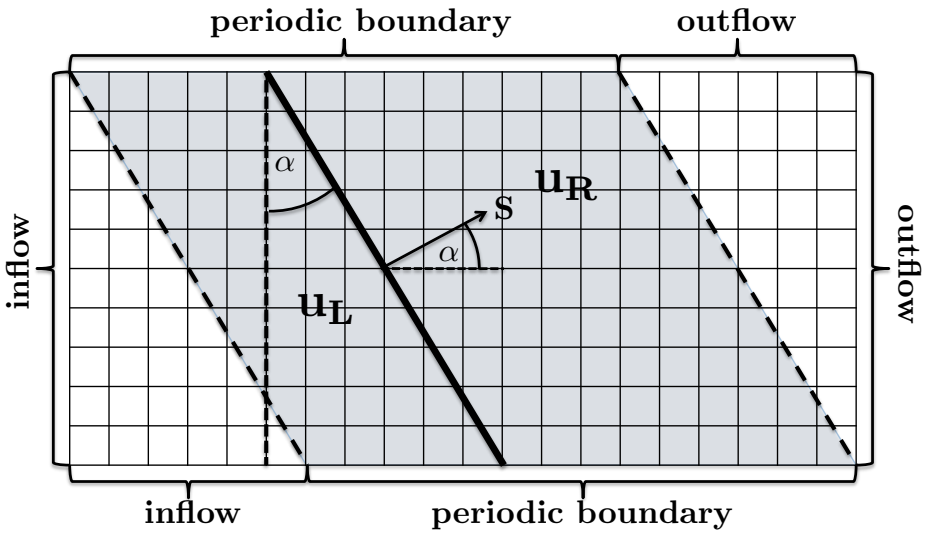


Figure 5.6: Initial set-up for the rotated slowly moving shock problem.

entirely inflow/outflow or skew-periodic. The top point of the shock in each test is $(x_0, y_0) = (0.5, 1)$. Only the first-order method is used since the second-order methods reduce to first-order around the shock and do not reduce the momentum spikes [37].

The results are shown in both the physical frame and the shock-aligned frame. At $\alpha = 0$, they are identical to the one-dimensional case. For $\alpha = 5.71°$ with $M_0 = 2.0$ and a shock speed of 0.01, the results in Figures 5.7 to 5.9 for Roe's flux and flux functions A and B show that both new flux functions reduce the momentum normal to the shockwave. The tangential momentum spike, however, is greater for both new flux functions. Both new fluxes significantly reduce the momentum spike normal to the shockwave for all angles (Figure 5.10) but worsen the spike tangential to the shock. For a faster moving shock at speed 0.1, the same trends continue for all angles, as seen in Figure 5.11.

Looking at a stronger shock, the tangential errors cause problems for both new fluxes. Specifically, for Mach 10 shock, the large tangential spikes lead to negative pressures, preventing a solution for $\alpha = 5.7°$ for both new flux functions. This is a result that is in agreement with the TVD analysis of Burgers' Equation in Section 4.4, where differences in sign between inner and outer wavespeeds can lead to the

growth of extrema. Nonetheless, as seen in the specific examples in Figures 5.12 to 5.16 and in the error plots in Figures 5.17 and 5.18, when the new flux functions do work, they show significant improvement normal to the shock.

### 5.4.2 1.5D Carbuncle

The one-and-a-half dimensional carbuncle consists of a planar shockwave in two-dimensions with identical conditions to the one dimensional problem in the $x$-direction and periodicity in the $y$-direction. The shockwave is initialized by prescribing the shock position in density, $x_S(\rho)$, and setting the remaining states based on the stable position of the intermediate state. The initial Mach number is 6.0 with a CFL number of 0.5 on a $50 \times 25$ uniform grid. 10,000 timesteps are run to check for instability. Similar to the work of Dumbser, a perturbation of $\mathcal{O}(10^{-6})$ is introduced. In this work, the perturbation has only been introduced to the intermediate state, leaving the pre- and post-shock states to preserve the initial properties of the stationary shock. Two main results are observed.

1. For perturbations in density, $x$-momentum, or energy that are identical in the y-direction, the result is the same as the one-dimensional case - all intermediate states are stable for both flux functions.

2. For either in density, $x$-momentum, or energy that are not identical in the y-direction or any perturbation to $y$-momentum (which is initially zero), both new flux functions are universally unstable.

In both of these situations, Roe's Riemann Solver was stable for certain intermediate shock positions and unstable for others. The new flux functions show no improvement over Roe's Riemann solver for this problem except in the purely one-dimensional case. Tangential perturbations prove difficult as they become unbounded and lead to failure of the solver.

### 5.4.3 Double Mach Reflection

To see how the new flux functions perform on a more practical problem with interacting shocks, the double Mach reflection is used. First described by Woodward and Colella [97], the double Mach reflection is designed to represent the interaction and reflection of a planar shockwave with a wedge. The initial conditions consist of a Mach 10 shockwave with initial position $x = \frac{1}{6} + \frac{y}{\sqrt{3}}$ and left and right states

$$\mathbf{u}_L = \begin{bmatrix} 8 \\ 57.16 \\ -33.00 \\ 563.54 \end{bmatrix} \qquad \mathbf{u}_R = \begin{bmatrix} 1.4 \\ 0.0 \\ 0.0 \\ 2.5 \end{bmatrix}. \tag{5.38}$$

The grid is uniform with $0 \leq x \leq 4$ and $0 \leq y \leq 1$. The wedge is modeled with a reflecting boundary condition, situated on the bottom from $x = 1/6$ to the end of the domain. The region prior to the wedge uses an inflow boundary condition as does the left side, at $x = 0$. The top boundary condition is set to the exact solution, following the shockwave in time and the right boundary condition is a simple outflow boundary condition. First-order results are shown in Figure 5.19. Both new fluxes perform well at the shock front but differ in the post-shock region, especially flux function A, which miscalculates the location of the interacting shock structure.

While second-order reconstructions as well as significantly finer grids were attempted, as the flow fields were resolved, both new fluxes experienced problems within the stagnation region near the wedge, due to the sensitivity to changes in velocity sign leading to either negative pressures or nonphysical fluxes, and failed to produce a physical solution.

### 5.4.4 Summary

The results show that even for oblique shocks, both new flux functions reduce errors normal to the shock front. Even with the simplistic implementation of the fluxes in two dimensions, there is a tangible gain for slowly moving shocks, suggesting a more intelligent treatment would produce even further benefits. Unfortunately, the second spatial dimension exacerbates the potential problems found in one dimension, such as nonphysicality of the interpolated fluxes and entropy-violating shockwaves. A particular problem is the performance of both new flux functions near oscillations in velocity, which can lead to negative pressures and densities.

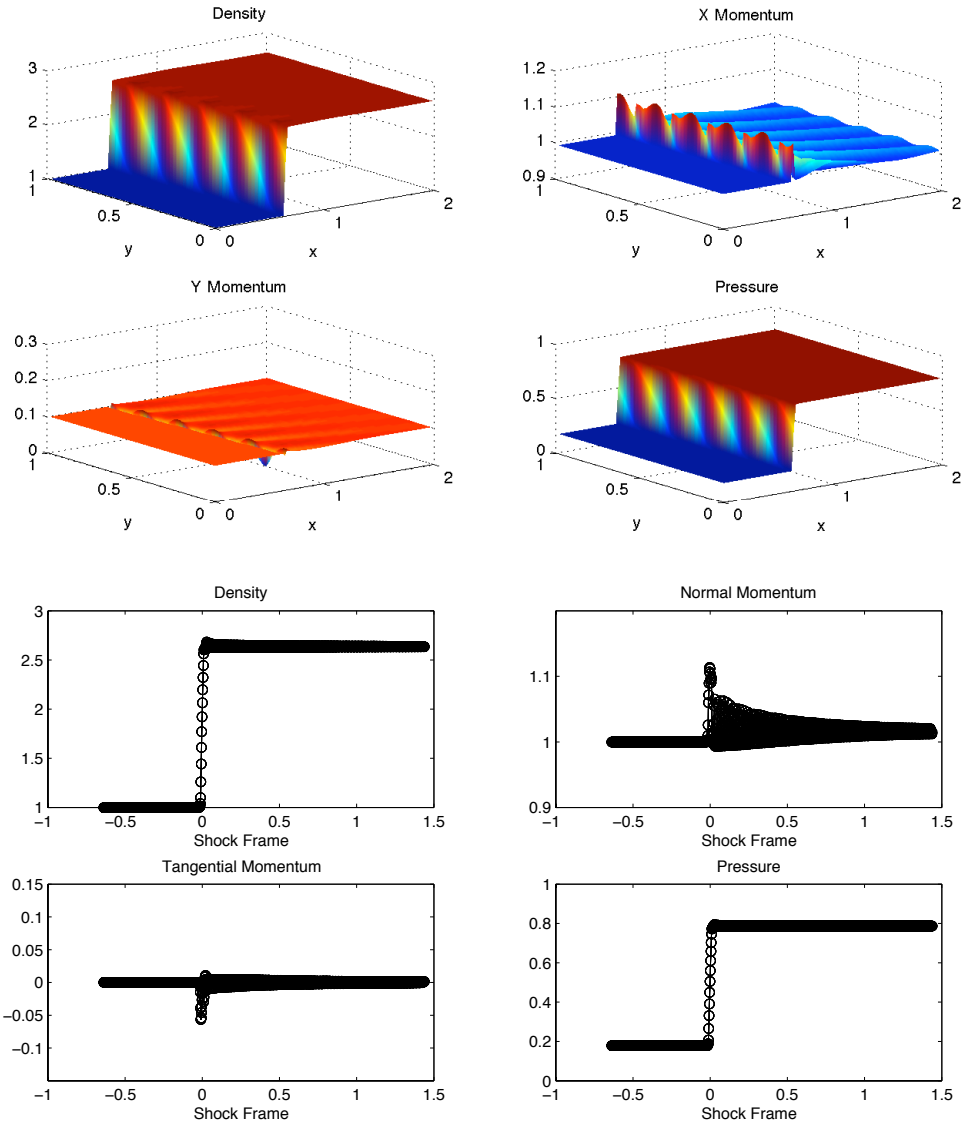


Figure 5.7: Results for the rotated slowly moving shock problem for Roe's Riemann solver with $M_0 = 2, S = 0.01$, and $\alpha = 5.71°$. Plots of density, x and y momentum, and pressure are shown in the physical frame, while density, normal and tangential momentum and pressure are shown in the shock frame.

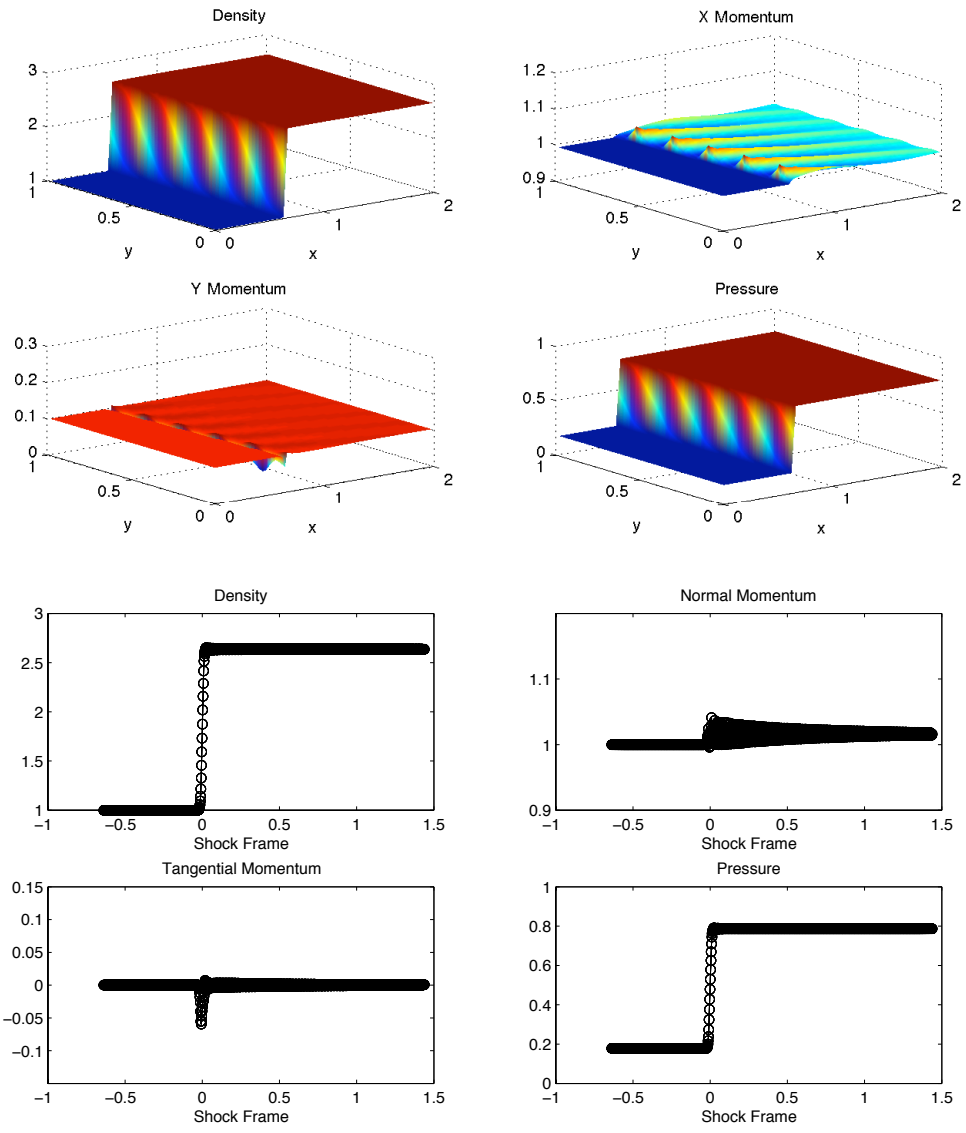


Figure 5.8: Results for the rotated slowly moving shock problem for flux function A. Same conditions and plots as Figure 5.7.

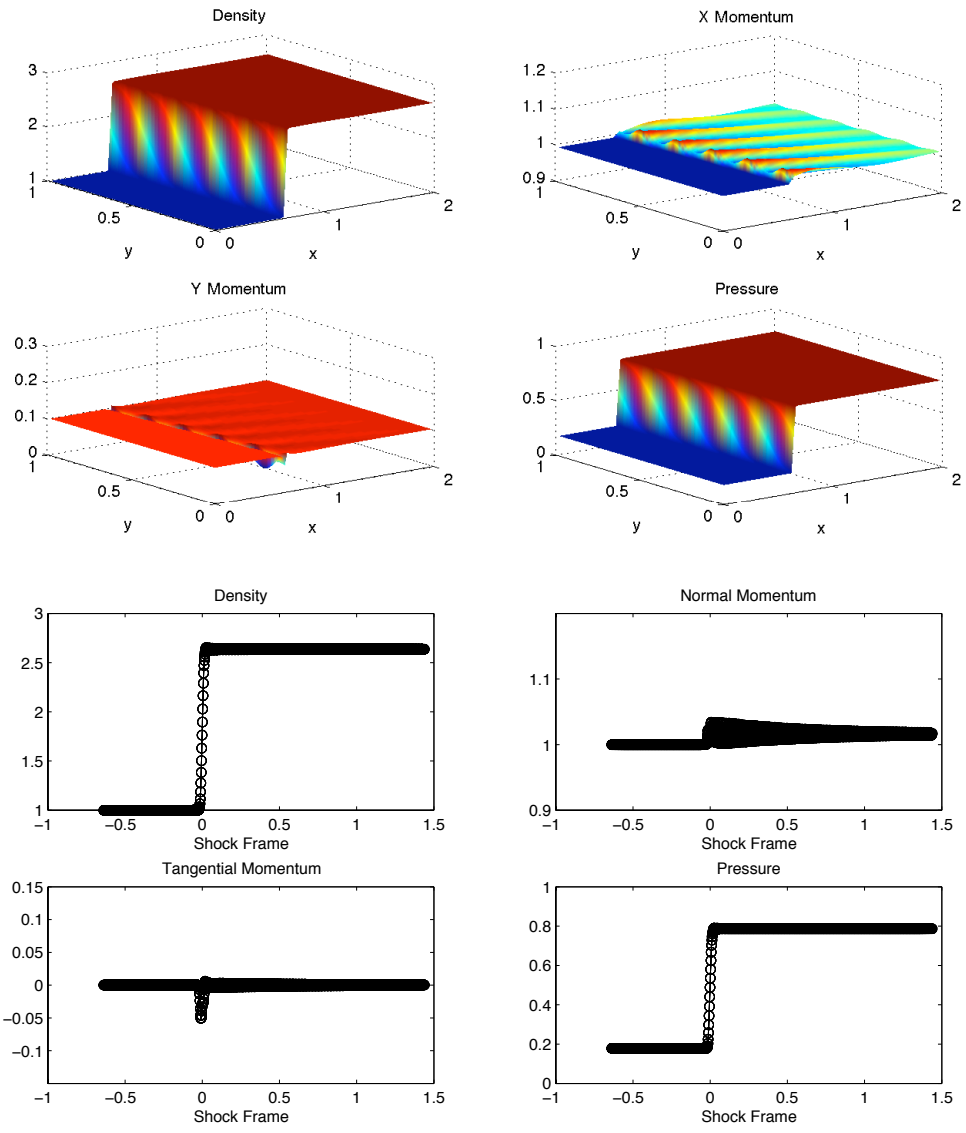


Figure 5.9: Results for the rotated slowly moving shock problem for flux function B. Same conditions and plots as Figure 5.7.

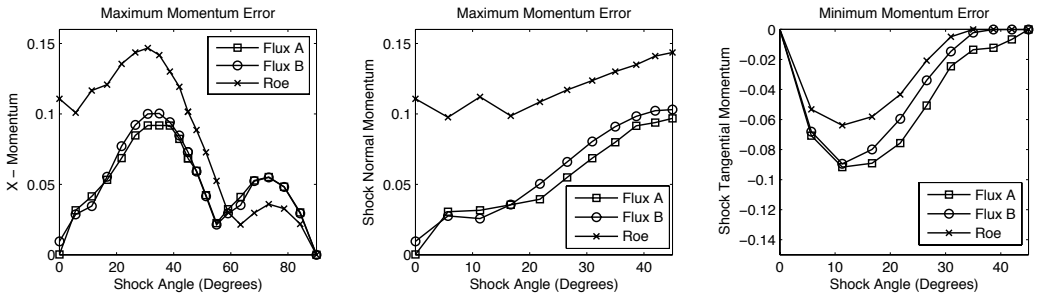


Figure 5.10: Errors in momentum for both new flux functions and Roe's Riemann solver for the Mach 2.0 shock with speed 0.01.

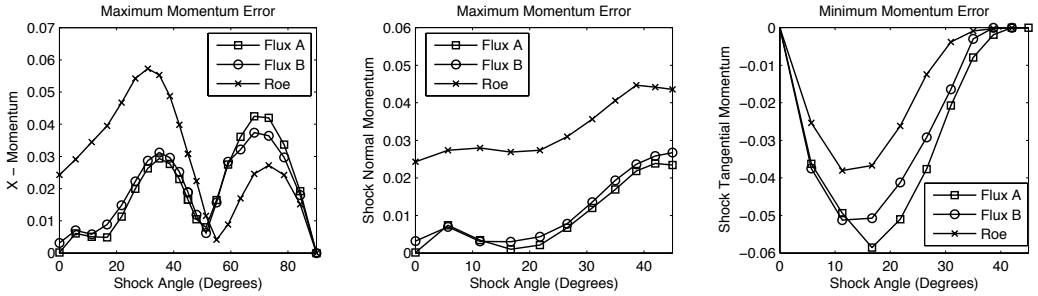


Figure 5.11: Errors in momentum for both new flux functions and Roe's Riemann solver for the Mach 2.0 shock with speed 0.1.

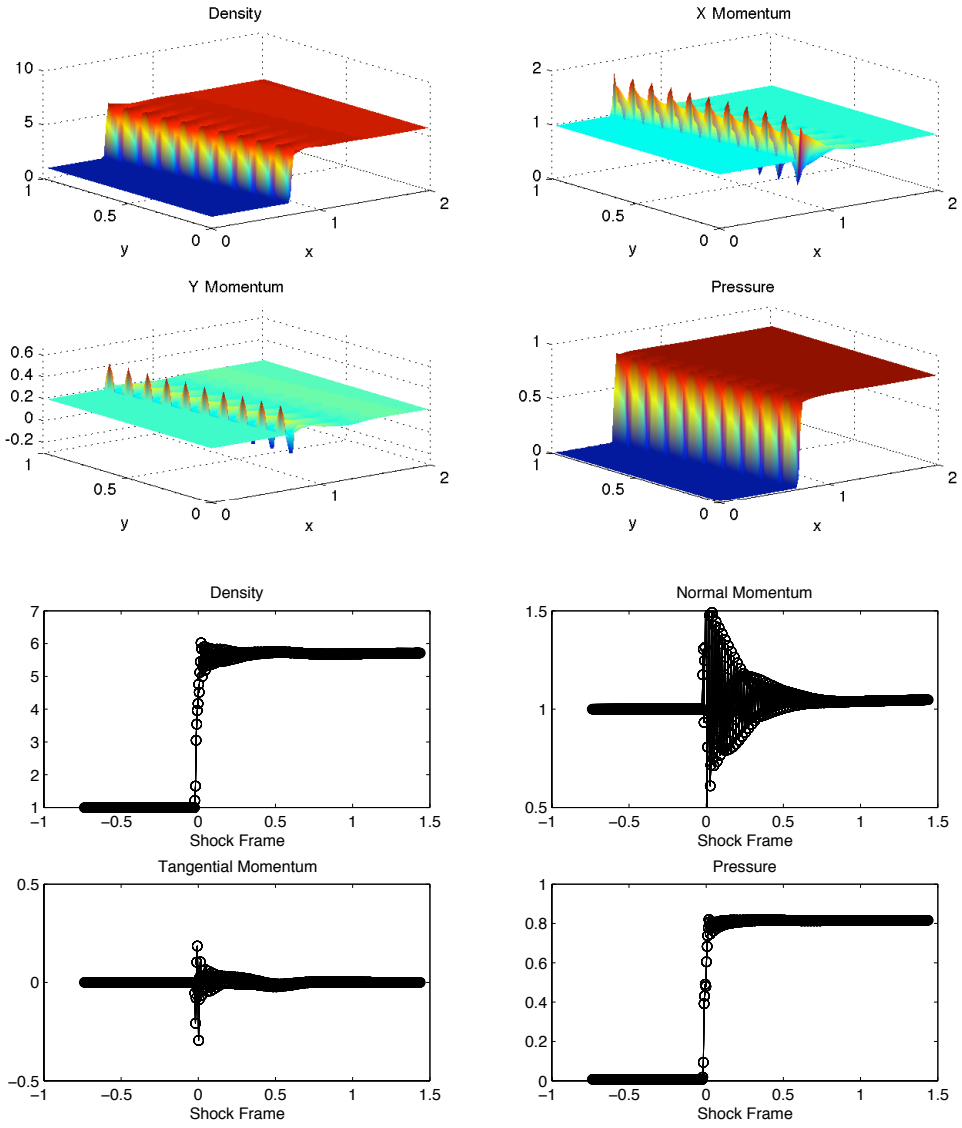


Figure 5.12: Results for the rotated slowly moving shock problem for Roe's Riemann solver with $M_0 = 10, S = 0.01$, and $\alpha = 11.4°$. Plots of density, x and y momentum, and pressure are shown in the physical frame, while density, normal and tangential momentum and pressure are shown in the shock frame.

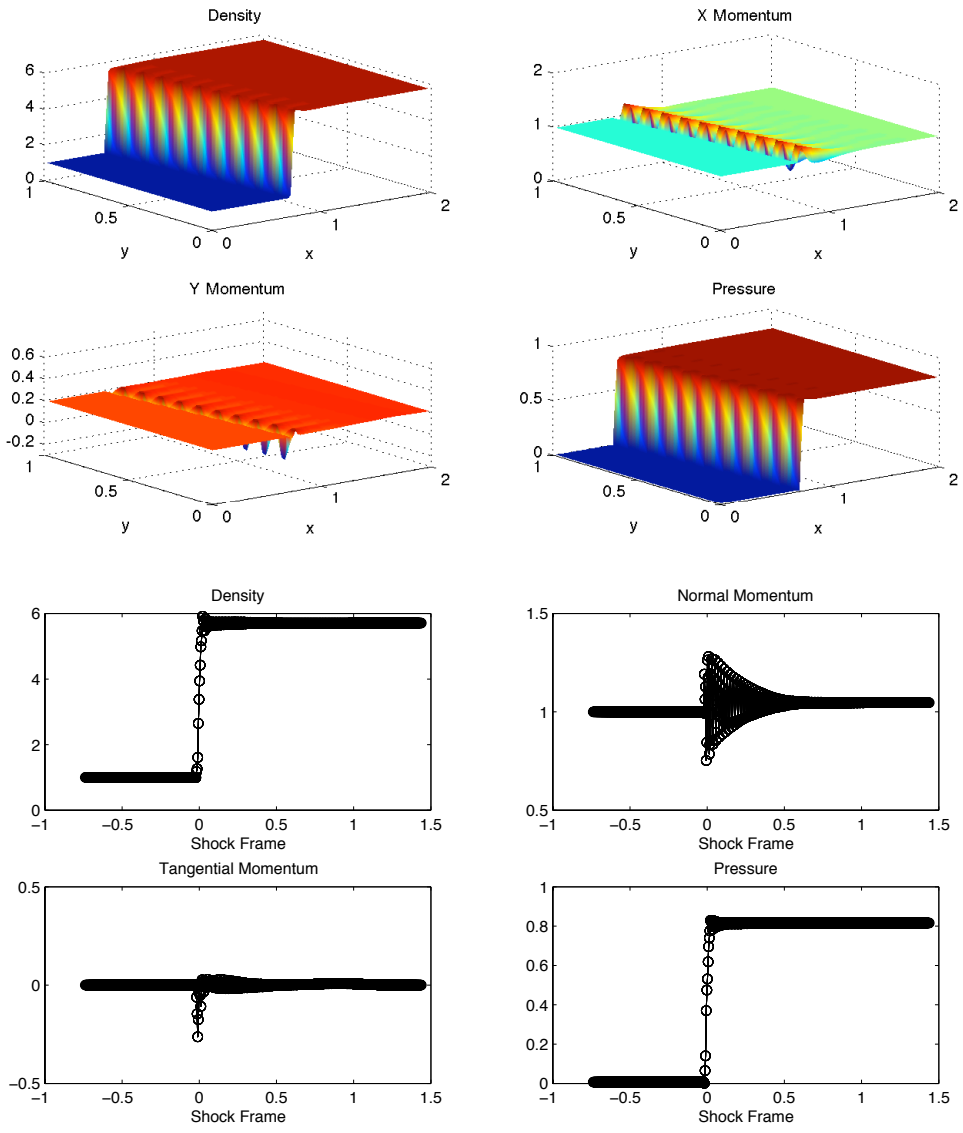


Figure 5.13: Results for the rotated slowly moving shock problem for flux function A. Same conditions and plots as Figure 5.12.

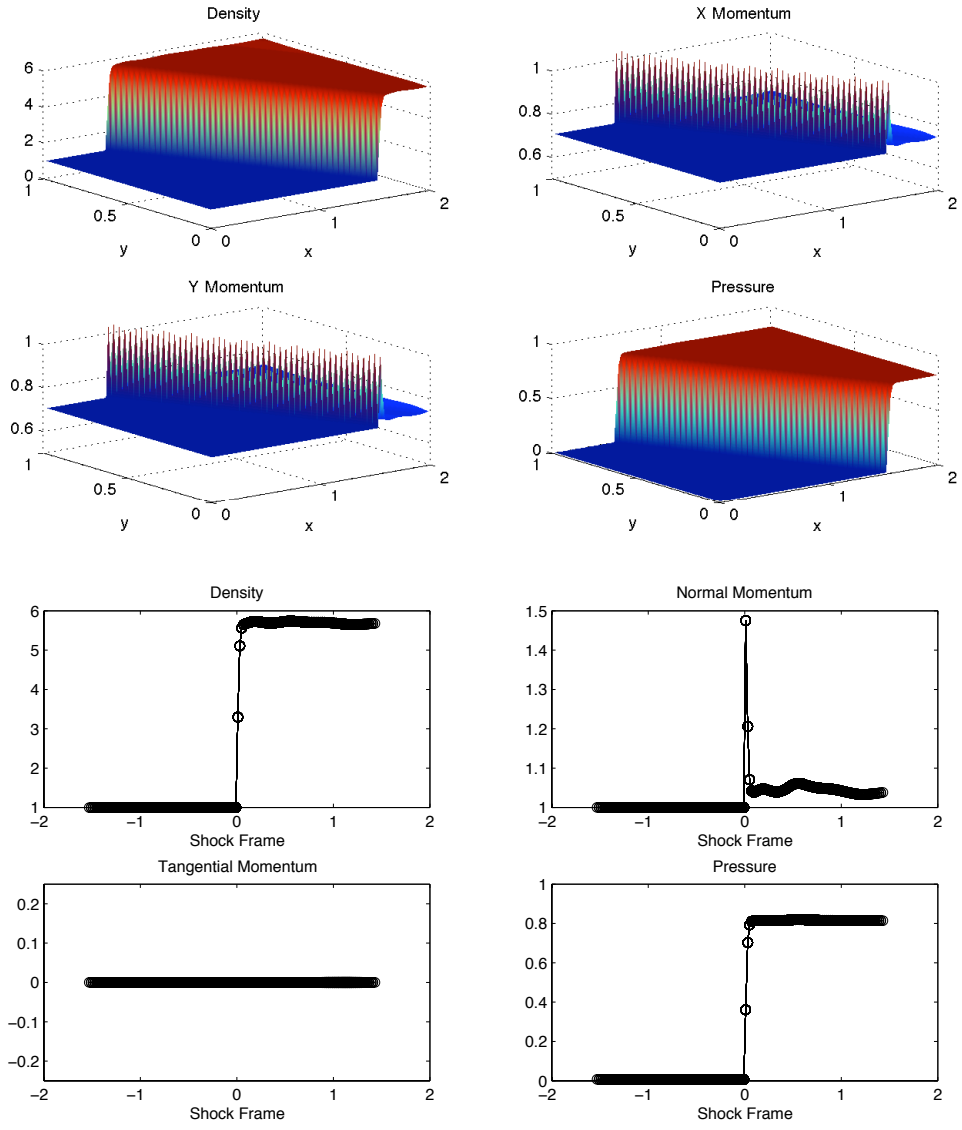


Figure 5.14: Results for the rotated slowly moving shock problem for Roe's Riemann solver with $M_0 = 10, S = 0.01$, and $\alpha = 41°$. Plots of density, x and y momentum, and pressure are shown in the physical frame, while density, normal and tangential momentum and pressure are shown in the shock frame.

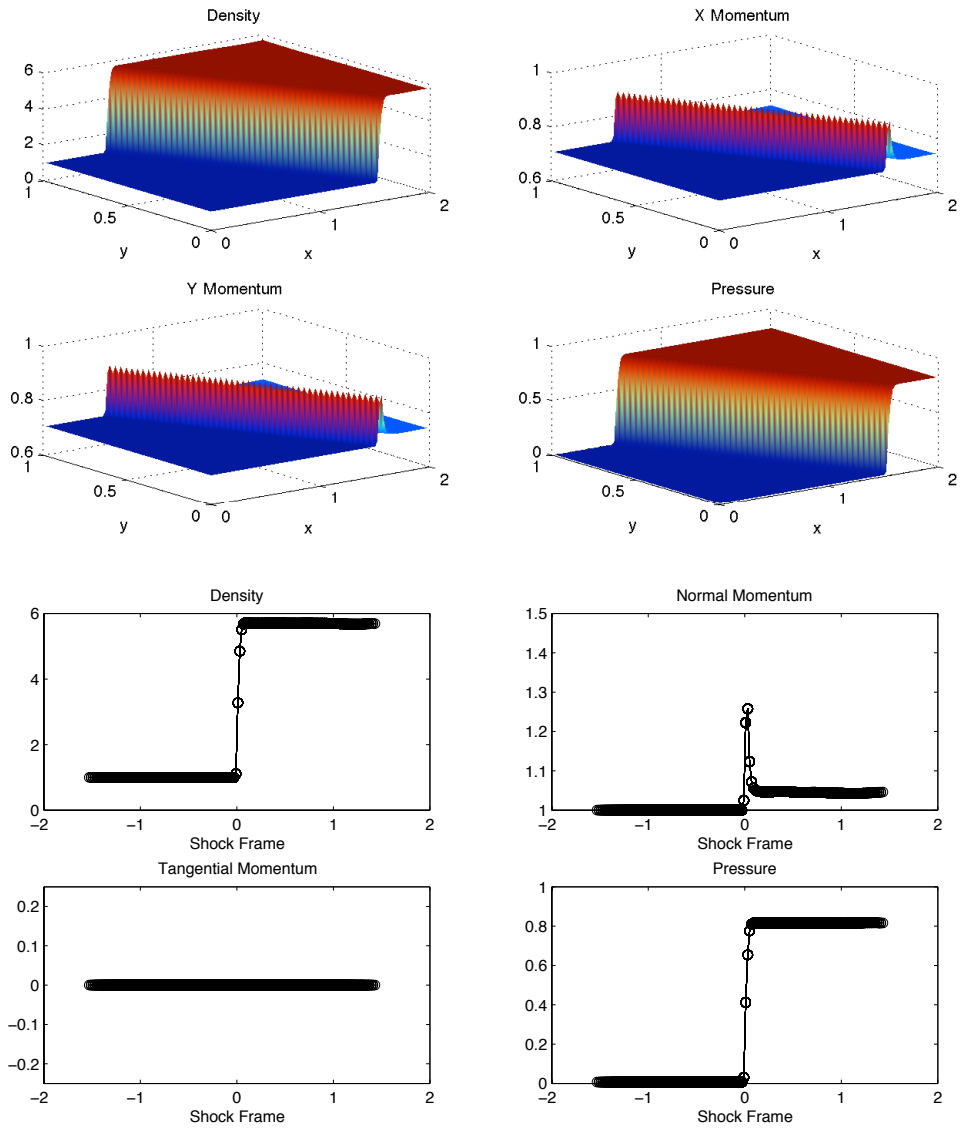


Figure 5.15: Results for the rotated slowly moving shock problem for flux function A. Same conditions and plots as Figure 5.14.

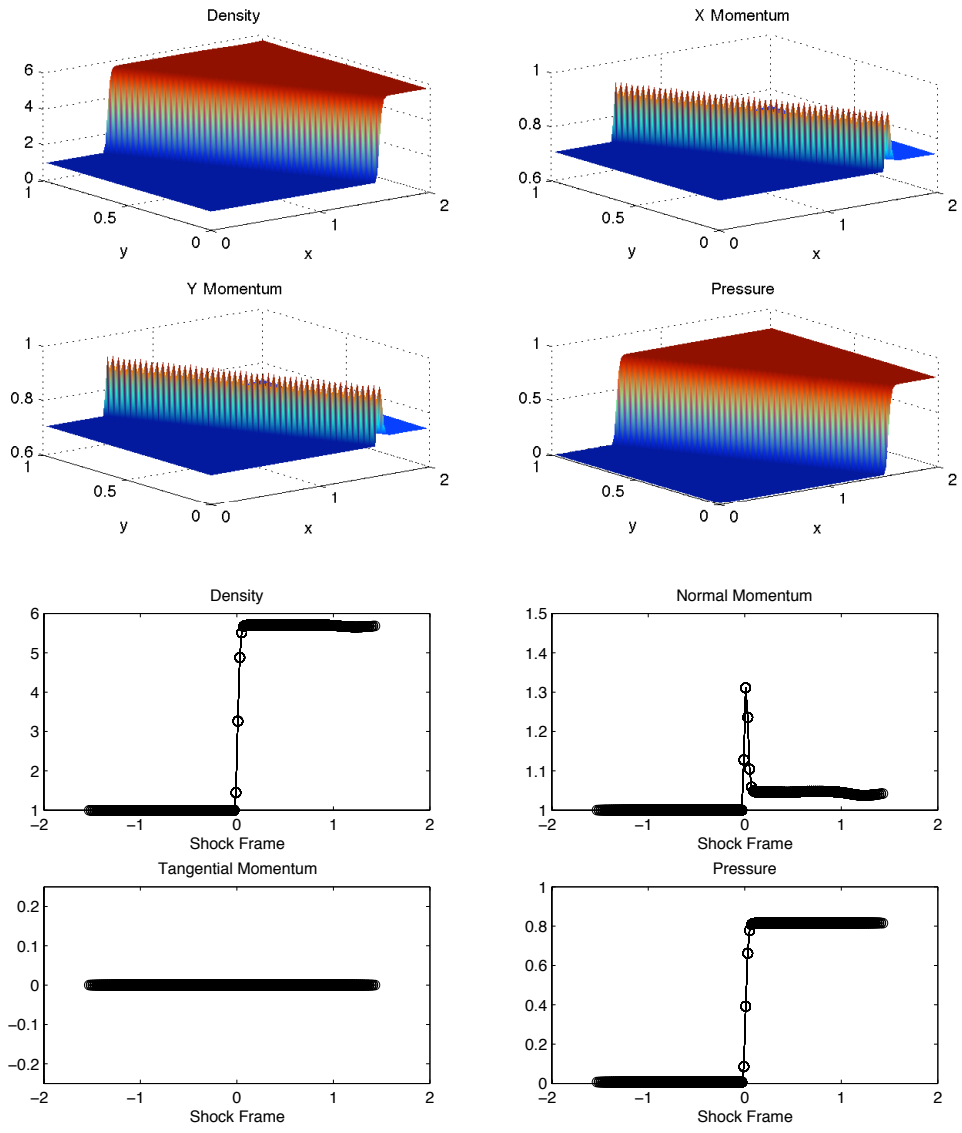


Figure 5.16: Results for the rotated slowly moving shock problem for flux function B. Same conditions and plots as Figure 5.14.

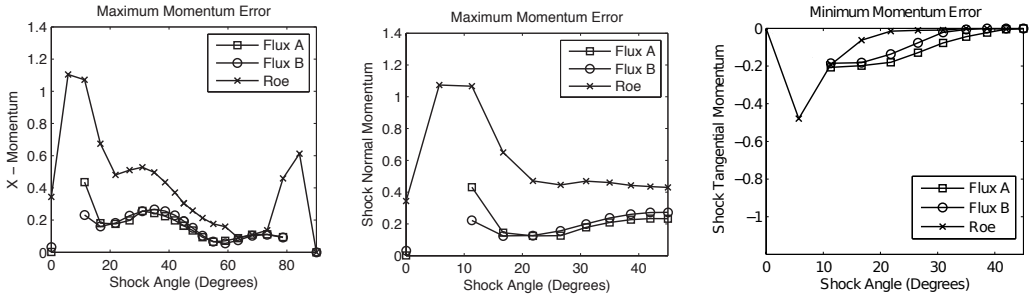


Figure 5.17: Errors in momentum for both new fluxes and Roe's Riemann solver for the Mach 10.0 shock with speed 0.01.

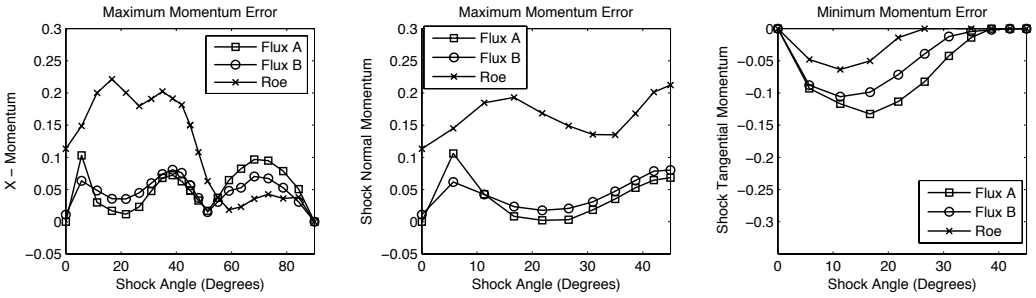


Figure 5.18: Errors in momentum for both new fluxes and Roe's Riemann solver for the Mach 10.0 shock with speed 0.1.

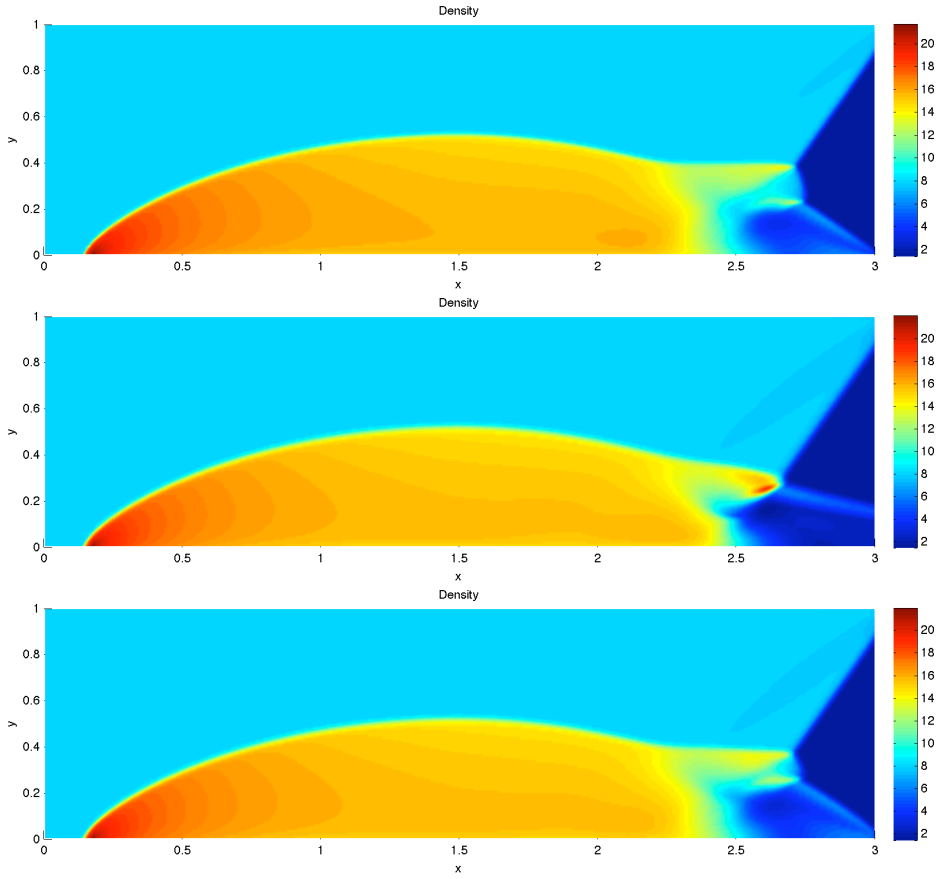


Figure 5.19: Density contours for the double mach reflection for a 480 x 120 grid at t = 0.2. (top) Roe. (middle) Flux A. (bottom) Flux B.

# CHAPTER VI

# Conclusions and Future Work

All captured shocks contain intermediate states between their end states. These intermediate states should not be taken literally; in particular it should not be assumed that they are in local thermodynamic equilibrium. Using the equilibrium equation of state for these intermediate states gives rise to intermediate states which differ from the projection of the exact solution into cell averages and to an ambiguity in the shock location. This ambiguity is linked to much of the anomalous behavior in shock-capturing schemes, represented by three canonical examples: the wall heating phenomenon, the slowly moving shock phenomenon, and the carbuncle. To eliminate the ambiguity, the intermediate states must agree on the location of the shock, and can use their own equation of state to achieve this numerical property. Since the equation of state within the shock is incorrect, it makes sense to choose an alternate 'incorrect' equation of state, one that solely serves to ensure the best numerical shock structure.

In the early stages of this research, it had been thought that this ideal shock structure could be achieved through the correct choice of equation of state, defining a numerical equation of state within each cell and switching to it within a shock. This equation of state would result in a linear Hugoniot curve and thus allow for an unambiguous one-point stationary shock. A nice idea, but for the Euler equations

no satisfactory equation was found. This led to the idea that more information was needed than just a single state; that thinking outside the box was necessary.

Going back to the stationary shock, all of the fluxes need to be equal. Numerically, this is achieved by having each interface flux, regardless of the conserved quantities and their corresponding fluxes in each cell, identical. This is somewhat unsettling, given that the fluxes computed from intermediate states do not agree with those of the stationary shock itself. This would be acceptable if there existed a Riemann solver, that is, a two-state flux function, with an unambiguous sub-cell shock position. After many attempts and sleepless nights, it was conjectured that no such Riemann solver existed and the more general idea of a flux function was needed.

With all this in mind, an alternate definition of the flux was introduced: the interpolated flux. The interpolated flux is constructed such that the internal fluxes of a stationary shock are equal to the external fluxes only if there is one intermediate state and with no sub-cell ambiguity. By enforcing a one-point shock, the interpolated flux stencil is kept small and the shock is well resolved; it contains the minimum number of intermediate states. The interpolated flux is also constructed to leave linear or straight-line systems untouched and have a minimal effect in smooth regions of the solution.

Two new flux functions were developed to utilize this tool. The first one, flux function A, is constructed based on the flux-wave approach [48] - decomposing the Riemann problem into jumps in interpolated flux across each wave, using wavespeeds to determine the direction of their contribution to the interface flux. The second one, flux function B, is based on the classical Roe Riemann solver, again using interpolated fluxes but relying on conserved variables to determine the jumps across each wave and the contribution of each wave to the interface flux.

On all of the shock anomalies in one-dimension, both fluxes showed improvement on existing methods without noticeably smearing or diffusing the shock. For a range

of other canonical problems, there was no major detriment to using the flux functions outside of shockwaves since they reduce to a second-order correction to Roe's Riemann solver and the differences were not observed in the first-order framework. From the TVD analysis with Burgers' equation, both flux functions were shown to not be TVD and could produce local extrema and unbounded solutions. In practice, through the use of an entropy fix, these problems were not observed in one dimension on either Burgers' equation or the Euler equations.

Of particular concern comes from the large literature base on Roe's Riemann solver. Over the past thirty years, numerous papers have been written about several flaws of this solver, such as expansion shocks and near-vacuum conditions [27, 15]. As both new fluxes are similar, they are presumably equally susceptible to these problems and could require more than just the standard fixes. As these problems are well documented and have existing fixes, it was speculated that there are fixes for both new flux functions and these problems do not compromise the utility of the method.

Looking at more complex problems, both flux functions were extended to two-dimensions. This tended to exacerbate the one-dimensional problems, observed in their repeated failures on each shock problem examined. Oscillations in velocity tended to grow indefinitely, leading to negative pressures or densities resulting in solver failure. The entropy fixes used in one-dimension were insufficient to alleviate these problems. Nevertheless, both new fluxes reduced momentum spikes normal to the shock, even when the shock was not aligned with the grid.

In smooth regions of the flow, second-order accuracy was achieved using a MUSCL-type approach, reconstructing both interpolated fluxes and conserved variables. While computationally expensive, these results suggest there is potential for both flux functions to fit within existing finite volume methods, a necessity for others who wish to implement this approach. At this point though, there does not seem to be any reason

to use either new flux in smooth regions; existing Riemann solvers can be used with no loss in accuracy, though switches are not desirable and introduce their own set of challenges.

With all the challenges associated with interpolated fluxes and both new flux functions, they still serve to validate the philosophy and approach taken in this thesis. *By enforcing a linear shock structure and unambiguous sub-cell shock position, numerical shockwave anomalies are dramatically reduced.* Some would argue that this approach is the same as others - add artificial viscosity. However, these new methods use dissipation to control shock structure rather than to approach the true viscous solution and do not in any way broaden the captured discontinuities. Regardless, the results are promising and open many doors in the quest for the perfect shock-capturing scheme. The strong performance on shockwaves and relatively weak performance on expansions also suggest that shocks and expansions should be treated differently, using an entirely different approach on each.

For the new flux functions to be practical, two main developments are needed:

- **Improved robustness.** The most pressing issue with both new fluxes in one dimension, is in their robustness, specifically their failures near expansion shocks and sensitivity to near vacuum conditions in one-dimension. While an entropy fix along the lines of Harten and Hyman [27] was suggested, there is no guarantee of its effectiveness and a deeper examination into the entropy fix is required. A known failure of Roe's Riemann solver is in near vacuum conditions, where the density is low and the solver cannot preserve the positivity of density [15]. As both new flux functions reduce to second-order corrections to Roe's Riemann solver in smooth regions, they are also susceptible to this issue. One approach

to mitigate both these issues stems from

$$\mathbf{f}_{i+\frac{1}{2}} = \frac{1}{2}(\mathbf{f}^*_i + \mathbf{f}^*_{i+1}) - \frac{1}{2}\overline{\mathbf{R}}_{i+\frac{1}{2}}\mathbf{Q}_{i+\frac{1}{2}}(\overline{\lambda}_{i+\frac{1}{2}}, \tilde{\lambda}_{i+\frac{1}{2}})\overline{\mathbf{L}}_{i+\frac{1}{2}}(\mathbf{u}_{i+1} - \mathbf{u}_i) \tag{6.1}$$

where $\mathbf{Q}$ is a function of the inner and outer wavespeeds, similar to a limiter, and $\mathbf{L}$ and $\mathbf{R}$ are the eigenvectors from the outer data. This approach is suggested by the analysis of Burgers' equation, which states that the TVD property can only be achieved under certain conditions of wavespeeds and wavestrengths. This formulation should alleviate these problems or at least allow for known fixes for Roe's Riemann solver to be easily integrated in.

- **Genuinely two-dimensional methods.** To overcome the problem stemming from oscillations tangential to a shock front, a truly two-dimensional version of the interpolated fluxes is required. As discussed in Section 5.2, when a steady shock runs obliquely across a two-dimensional grid, any intersected cell will contain an intermediate state, and is therefore not trustworthy. Ideally, all such cells should be detected and forced onto the straight line connecting the end states of the shock. The fluxes in these cells should all have the same interpolated fluxes. This would require constructing interpolated fluxes from more than just their one-dimensional neighbors, possibly using a five or nine cell stencil. This guarantees that for the stationary shock, at least one neighbor contains an end state of the shock (trustworthy information).

Alongside these pressing needs, several other potential uses for this research in the future include:

- **Adaptive Riemann solvers.** An alternate approach to make either flux function practical is through an adaptive Riemann solver. Using some form of shock detection, a hybrid approach can be taken using the new flux functions around

shocks and switching to an alternate solver in smooth regions. This approach is fairly common and seems like a logical place for the new flux functions.

- **Improving convergence rates for steady problems with shocks.** When time-marching to steady state, many simulations suffer from slow convergence rates as a result of the inability of the shock to reach a stable position. Since both new flux functions have all positions stable, at least in one dimension, this problem might be overcome and should be investigated.

# BIBLIOGRAPHY

# BIBLIOGRAPHY


[1] Arora, M., and Roe, P. L. On postshock oscillations due to shock capturing schemes in unsteady flows. *Journal of Computational Physics 130*, 1 (1997), 25–40.

[2] Barth, T. J. Some notes on shock resolving flux functions. part 1: Stationary characteristics. *NASA Technical Memorandum* (1989).

[3] Bressan, A., Jenssen, H., and Baiti, P. An instability of the godunov scheme. *Communications on Pure and Applied Mathematics 59*, 11 (2006), 1604–1638.

[4] Bressan, A., and Jenssen, H. K. Convergence of the godunov scheme for straight line systems. *Hyperbolic Problems: Theory, Numerics, Applications: Eighth International Conference in Magdeburg 1* (2001), 187–196.

[5] Bultelle, M., Grassin, M., and Serre, D. Unstable godunov discrete profiles for steady shock waves. *SIAM Journal on Numerical Analysis 35*, 6 (1998), 2272–2297.

[6] Cameron, I. G. An analysis of the errors caused by using artificial viscosity terms to represent steady-state shock waves. *Journal of Computational Physics 1* (1966), 1–20.

[7] Carpenter, M. H., and Casper, J. H. Accuracy of shock capturing in two spatial dimensions. *AIAA Journal* (1999), 488–498.

[8] Chauvat, Y., Moschetta, J., and Gressier, J. Shock wave numerical structure and the carbuncle phenomenon. *International Journal for Numerical Methods in Fluids 47*, 89 (2005), 903–909.

[9] Courant, R., and Friedrichs, K. Supersonic flow and shock waves. *Interscience* (1948).

[10] Courant, R., Friedrichs, K., and Lewy, H. On the partial difference equations of mathematical physics. *IBM Journal of Research and Development 11*, 2 (1928), 215–234.

[11] Donat, R., and Marquina, A. Capturing shock reflections: an improved flux formula. *Journal of Computational Physics 125* (1996), 42–58.

[12] Dumbser, M., Moschetta, J.-M., and Gressier, J. A matrix stability analysis of the carbuncle phenomenon. *Journal of Computational Physics 197*, 2 (2004), 647–670.

[13] D'yakov, S. Shock wave stability. *Zh. Eksp. Teor. Fiz* (1954), 288.

[14] Efraimsson, G., and Kreiss, G. A note on the effect of artificial viscosity on solutions of conservation laws. *Applied Numerical Mathematics 21* (1996), 155–173.

[15] Einfeldt, B., Munz, C., Roe, P., and Sjogreen, B. On godunov-type methods near low densities. *Journal of Computational Physics 92* (1991), 273–295.

[16] Elling, V. The carbuncle phenomenon is incurable. *Acta Mathematica Scientia, Series B 29*, 6 (2010), 1647–1656.

[17] Emery, A. An evaluation of several differencing methods for inviscid fluid flow problems. *Journal of Computational Physics 2* (1968), 306–331.

[18] Fedkiw, R., Marquina, A., and Merriman, B. An isobaric fix for the overheating problem in multimaterial compressible flows. *Journal of Computational Physics 148*, 2 (1999), 545–578.

[19] Gehmeyr, M., Cheng, B., and Mihalas, D. Noh's constant-velocity shock problem revisited. *Shock Waves 7*, 5 (1997), 255–274.

[20] Glaister, P. An approximate linearised riemann solver for the euler equations for real gases. *Journal of Computational Physics 74* (1988), 382–408.

[21] Gnoffo, P. Private communication.

[22] Godlewski, E., and Raviart, P.-A. Hyperbolic systems of conservation laws. *Mathematiques & Applications* (1991).

[23] Godunov, S. K. A difference method for numerical calculation of discontinuous solutions of the equations of hydrodynamics. *Matematicheskii Sbornik* (1959).

[24] Gottlieb, S., Shu, C.-W., and Tadmor, E. Strong stability-preserving high-order time discretization methods. *SIAM review 43*, 1 (2001), 89–112.

[25] Guermond, J.-L., and Pasquetti, R. Entropy-based nonlinear viscosity for fourier approximations of conservation laws. *Comptes Rendus Mathematique 346* (2008), 801–806.

[26] Harten, A. High resolution schemes for hyperbolic conservation laws. *Journal of Computational Physics 49* (1983), 357–393.

[27] Harten, A., and Hyman, J. M. Self adjusting grid methods for one-dimensional hyperbolic conservation laws. *Journal of Computational Physics 50* (1983), 235–269.

[28] Henderson, S. Study of the issues of computational aerothermodynamics using a riemann solver. *Ph.D. Thesis* (2007).

[29] Hu, C., and Shu, C.-W. Weighted essentially non-oscillatory schemes on triangular meshes. *Journal of Computational Physics 150* (1999), 97–127.

[30] Hui, W., and Kudriakov, S. On wall overheating and other computational difficulties of shock-capturing methods. *Computational Fluid Dynamics Journal 10*, 2 (2001), 192–209.

[31] Ismail, F. Toward a reliable prediction of shocks in hypersonic flow: resolving carbuncles with entropy and vorticity control. *Ph.D. Thesis* (2006).

[32] Ismail, F., and Roe, P. Affordable, entropy-consistent euler flux functions ii: Entropy production at shocks. *Journal of Computational Physics 228* (2009), 5410–5436.

[33] Jennings, G. Discrete shocks. *Communications on Pure and Applied Mathematics 27* (1974), 25–37.

[34] Jin, S., and Liu, J.-G. Oscillations induced by numerical viscosities. *Mat. Contemp 10* (1995), 169–180.

[35] Jin, S., and Liu, J.-G. The effects of numerical viscosities: I. slowly moving shocks. *Journal of Computational Physics 126*, 2 (1996), 373–389.

[36] Johnsen, E., and Lele, S. K. Numerical errors generated in simulations of slowly moving shocks. *Center for Turbulence Research, Annual Research Briefs* (2008), 1–12.

[37] Johnsen, E., Lele, S. K., and Larsson, J. Analysis and correction of errors generated by slowly moving shocks. *Proceedings of the 49th AIAA Aerospace Sciences Meeting* (2011).

[38] Karni, S., and Canic, S. Computations of slowly moving shocks. *Journal of Computational Physics 136*, 1 (1997), 132–139.

[39] Kemm, F. A carbuncle free roe-type solver for the euler equations. *Hyperbolic Problems: Theory, Numerics, Applications* (2008), 601–608.

[40] Kim, S., Kim, C., Rho, O., and Hong, S. K. Cures for the shock instability: development of a shock-stable roe scheme. *Journal of Computational Physics 185*, 2 (2003), 342–374.

[41] Kim, S., Lee, B., Lee, H. J., Jeung, I.-S., and Choi, J.-Y. Realization of contact resolving approximate riemann solvers for strong shock and expansion flows. *International Journal for Numerical Methods in Fluids 62* (2009), 1107–1133.

[42] Kitamura, K., Roe, P. L., and Ismail, F. Evaluation of euler fluxes for hypersonic flow computations. *AIAA Journal 47*, 1 (2008), 44–53.

[43] Kitamura, K., Shima, E., and Roe, P. Three-dimensional carbuncles and euler fluxes. *Proceddings of the 48th AIAA Aerospace Sciences Meeting* (2010).

[44] Landau, L., and Lifshitz, E. Fluid mechanics. *Pergammon* (1959).

[45] Lax, P. Weak solutions of nonlinear hyperbolic equations and their numerical computation. *Communications on Pure and Applied Mathematics 7* (1954), 159–193.

[46] Lax, P. Hyperbolic systems of conservation laws ii. *Communications on Pure and Applied Mathematics 10* (1957), 537–566.

[47] Lax, P., and Wendroff, B. Systems of conservation laws. *Communications on Pure and Applied Mathematics 13* (1960), 217–237.

[48] LeVeque, R. Wave propagation algorithms for multidimensional hyperbolic systems. *Journal of Computational Physics 131*, 2 (1997), 327–353.

[49] Leveque, R. J. Numerical methods for conservation laws. *Birkhauser Verlag AG* (1994).

[50] Liou, M., and Steffen, C. A new flux splitting scheme. *Journal of Computational Physics 107* (1993), 23–39.

[51] Liou, M.-S. Mass flux schemes and connection to shock instability. *Journal of Computational Physics 160* (2000), 623–648.

[52] Liou, M.-S. Open problems in numerical fluxes: Proposed resolutions. *Proceedings of the 20th AIAA Computational Fluid Dynamics Conference* (2011).

[53] Liu, J.-G., and Xin, Z. Nonlinear stability of discrete shocks for systems of conservation laws. *Archive for rational mechanics and analysis 125* (1993), 217–256.

[54] Liu, T.-P., and Yu, S.-H. Continuum shock profiles for discrete conservation laws i: Construction. *Communications on Pure and Applied Mathematics 52* (1999), 0085–0127.

[55] Liu, T.-P., and Yu, S.-H. Continuum shock profiles for discrete conservation laws, ii: Stability. *Communications on Pure and Applied Mathematics, 52* (1999), 1047–1073.

[56] Lowrie, R. B. Compact higher-order numerical methods for hyperbolic conservation laws. *Ph.D. Thesis* (1996).

[57] MacCormack, R. The carbuncle cfd problem. *Proceedings of the 49th AIAA Aerospace Sciences Meeting* (2011).

[58] Majda, A., and Ralston, J. Discrete shock profiles for systems of conservation laws. *Communications on Pure and Applied Mathematics 32* (1979), 445–483.

[59] Menikoff, R. Errors when shock waves interact due to numerical shock width. *SIAM Journal on Scientific Computing 15*, 5 (1994), 1227–1242.

[60] Menikoff, R. Numerical anomalies mimicking physical effects. *AIP Conference Proceedings* (1996).

[61] Moretti, G. A pragmatical analysis of discretization procedures for initial and boundary value problems in gas dynamics and their influence on accuracy or look ma, no wiggles. *Unpublished PIBAL Report* (1974).

[62] Munz, C. On godunov-type schemes for lagrangian gas dynamics. *SIAM Journal on Numerical Analysis 31*, 1 (1994), 17–42.

[63] Myong, R. S., and Roe, P. L. Shock waves and rarefaction waves in magnetohydrodynamics. part 2. the mhd system. *Journal of Plasma Physics 58*, 3 (1997), 521–552.

[64] Nishikawa, H., and Kitamura, K. Very simple, carbuncle-free, boundary-layer-resolving, rotated-hybrid riemann solvers. *Journal of Computational Physics 227* (2008), 2560–2581.

[65] Noh, W. F. Errors for calculations of strong shocks using an artificial viscosity and an artificial heat flux. *Journal of Computational Physics 72*, 1 (1987), 78–120.

[66] Paciorri, R., and Bonfiglioli, A. A shock-fitting technique for 2d unstructured grids. *Computers & Fluids 38* (2009), 715–726.

[67] Paciorri, R., and Bonfiglioli, A. Shock interaction computations on unstructured, two-dimensional grids using a shock-fitting technique. *Journal of Computational Physics 230* (2011), 3155–3177.

[68] Pandolfi, M., and D'Ambrosio, D. Numerical instabilities in upwind methods: analysis and cures for the "carbuncle" phenomenon. *Journal of Computational Physics 166*, 2 (2001), 271–301.

[69] Peery, K., and Imlay, S. Blunt-body flow simulations. *AIAA paper* (1988), 88–2924.

[70] Ramalho, M. V. C., Azevedo, J. H. A., and Azevedo, J. L. F. Further investigation into the origin of the carbuncle phenomenon in aerodynamic simulations. *Proceedings of the 49th AIAA Aerospace Sciences Meeting* (2011).

[71] Ren, Y.-X. A robust shock-capturing scheme based on rotated riemann solvers. *Computers and Fluids 32* (2003), 1379–1403.

[72] Rider, W. Revisiting wall heating. *Journal of Computational Physics 162* (2000), 395–410.

[73] Roberts, T. W. The behavior of flux difference splitting schemes near slowly moving shock waves. *Journal of Computational Physics 90*, 1 (1990), 141–160.

[74] Robinet, J., Gressier, J., Casalis, G., and Moschetta, J. Shock wave instability and the carbuncle phenomenon: same intrinsic origin? *Journal of Fluid Mechanics 417* (2000), 237–263.

[75] Rodzhestvenskii, B. I., and Yanenko, N. N. Systems of quasilinear equations and their applications to gas dynamics. *AMS Translation* (1983).

[76] Roe, P. Computational fluid dynamics - retrospective and prospective. *International Journal of Computational Fluid Dynamics 19*, 8 (2006), 581–594.

[77] Roe, P., Nishikawa, H., Ismail, F., and Scalabrin, L. On carbuncles and other excrescences. *Proceedings of the 17th AIAA Computational Flow Dynamics Conference* (2005), 1–10.

[78] Roe, P. L. Approximate riemann solvers, parameter vectors, and difference schemes. *Journal of Computational Physics 43* (1981), 357–372.

[79] Roe, P. L. Fluctuations and signals - a framework for numerical evolution problems. *Numerical Methods for Fluid Dynamics* (1982), 219–257.

[80] Roe, P. L., and Zaide, D. W. Entropy traces in lagrangian and eulerian calculations. *Proceedings of the 7th International Conference on Computational Fluid Dynamics* (2010).

[81] Rusanov, V. V. Calculation of interaction of non-steady shock waves with obstacles. *J. Comput. Math. Phys. USSR 1* (1961), 267–279.

[82] Salas, M. D. Shock fitting method for complicated two-dimensional supersonic flows. *AIAA Journal 14*, 5 (1976), 583–588.

[83] Salas, M. D. A shock-fitting primer. *CRC Press* (2010).

[84] Serre, D. Remarks about the discrete profiles of shock waves. *Mat. Contemp 11* (1996), 153–170.

[85] Shima, E., and Kitamura, K. On ausm-family scheme for all speeds with shock detection for carbuncle-fix. *Proceedings of the 19th AIAA Computational Fluid Dynamics Conference* (2009).

[86] Shu, C.-W., and Osher, S. Efficient implementation of essentially non-oscillatory shock-capturing schemes, ii. *Journal of Computational Physics 83* (1989), 32–78.

[87] Sod, G. A. A survey of several finite difference methods for systems of nonlinear hyperbolic conservation laws. *Journal of Computational Physics 27* (1978), 1–31.

[88] Steger, J. L., and Warming, R. Flux vector splitting of the inviscid gasdynamic equations with application to finite-difference methods. *Journal of Computational Physics 40* (1981), 263–293.

[89] Stiriba, Y., and Donat, R. A numerical study of postshock oscillations in slowly moving shock waves. *Computers & Mathematics with Applications 46*, 5-6 (2003), 719–739.

[90] Temple, B. Systems of conservation laws with invariant submanifolds. *Transactions of the Americal Mathematical Society 280*, 2 (1983), 781–795.

[91] Toro, E. F. Riemann solvers and numerical methods for fluid dynamics: A practical introduction. *Springer-Verlag* (1999), 1–605.

[92] Toro, E. F. Anomalies of conservative methods: analysis, numerical evidence and possible cures. *Computational Fluid Dynamics Journal 11*, 2 (2002), 128–143.

[93] Trepanier, J., Paraschivoiu, M., Reggio, M., and Camarero, R. A conservative shock fitting method on unstructured grids. *Journal of Computational Physics 126* (1996), 421–433.

[94] van Leer, B. Towards the ultimate conservative difference scheme. iv. a new approach to numerical convection. *Journal of Computational Physics 23* (1977), 276–299.

[95] von Neumann, J., and Richtmyer, R. D. A method for the numerical calculation of hydrodynamic shocks. *Journal of Applied physics 21* (1950), 232–237.

[96] Woodward, P. Ppm: Piecewise-parabolic methods for astrophysical fluid dynamics. *Astrophysical Radiation Hydrodynamics 1* (1986), 245–326.

[97] Woodward, P., and Colella, P. The numerical simulation of two-dimensional fluid flow with strong shocks. *Journal of Computational Physics 54* (1984), 115–173.

[98] Xu, K. Does perfect riemann solver exist? *Proceedings of the 14th AIAA Computational Fluid Dynamics Conference* (1999).

[99] Xu, K., and Hu, J. Projection dynamics in godunov-type schemes. *Journal of Computational Physics 142*, 2 (1998), 412–427.

[100] Xu, K., and Prendergast, K. H. Numerical navier-stokes solutions from gas kinetic theory. *Journal of Computational Physics 114*, 1 (1994), 9–17.

[101] Yamaleev, N. K., and Carpenter, M. H. On accuracy of adaptive grid methods for captured shocks. *Journal of Computational Physics 181* (2002), 280–316.

[102] Zaide, D. W., and Roe, P. L. Shock capturing anomalies and the jump conditions in one dimension. *Proceedings of 20th AIAA Computational Fluid Dynamics Conference, 2011-3686* (2011).

[103] Zel'dovich, Y. B., and Raizer, Y. P. Physics of shock waves and high-temperature hydrodynamic phenomena. *Academic, New York* (1966).